Parametric Modeling of the Brain Vascular System and its Application in Dynamic Contrast-Enhanced Imaging Studies

by

Siamak P. Nejad-Davarani

A dissertation submitted in partial fulfillment
of the requirements for the degree of
Doctor of Philosophy
(Biomedical Engineering)
in the University of Michigan
2014

Doctoral Committee:

Professor Douglas C. Noll, Chair
Associate Professor Hassan Bagher-Ebadian, Oakland University
Associate Professor Nikolaos Chronis
Professor James R. Ewing, Oakland University
Professor J. Brian Fowlkes
Research Associate Professor Luis Hernandez-Garcia
Professor Quan Jiang, Wayne State University

To my parents:

Dr. Mohammad-Ali Pourabdollah-Nezhad

Mohtaram Nashvadian-Bakhsh

ACKNOWLEDGEMENTS

During the years I have been working on my Ph.D., I have had the support and guidance of many individuals who made it possible for me to go through this journey.

First, I would like to thank my graduate advisor Dr. Douglas Noll. From the time I entered the program, his guidance, encouragement and patience kept my studies and research on the right track and helped me move any obstacles that may have come in the pathway of my research. I thank Dr. Hassan Bagher-Ebadian for introducing me to the field of Dynamic Contrast Enhanced Imaging and for being a great mentor, advisor and inspiration for me during the time I have been researching in this field. I thank my supervisor at Henry Ford Hospital, Dr. Quan Jiang for being a great mentor and for guiding me through my research and for supporting me during the time I was in the Ph.D. program. I thank Dr. James R. Ewing for his valuable feedback and guidance on my research and Dr. Michael Chopp for his support and for providing me with an environment for conducting my research. I would also like to thank members of my doctoral committee, Dr. Luis Hernandez-Garcia, Dr. Brian Fowlkes and Dr. Nikos Chronis and also Dr. Joseph Bull for their valuable input, suggestions and feedback on my dissertation.

I would like to thank Dr. Behzad Ebrahimi, Dr. Vahed Qazvinian, Dr. Soroush Saghafian and Mrs. Aazam Ranjbar (Bagher-Ebadian) and the Bagher-Ebadian family which have been great friends and supporters along the way. I give a special thanks to Ms. Aurpita Akbar whose incredible support I had during the time I was working on this dissertation. Also I thank all my colleagues and friends at the Neurology NMR lab at Henry Ford Hospital and at the fMRI lab and the BME department at the University of Michigan especially Dr. Scott Peltier, Dr. Jon-Fredrik Nielsen, Ms. Vicki Sloane, Ms. Maria Steele, Mr. Simon Eggeraat, Dr. Robert Knight and Ms. Lisa Scarpace.

Last and not least, I save a special thank you for my family especially my father Dr. Mohammad Ali Pourabdollah-Nezhad and my mother Mohtaram Nashvadiam-bakhsh who have been my foremost supporters and have been wonderful teachers for me, all through my years of studying, and in all aspects of my life. And I thank my brother Dr. Maziar P. Nezhad for being my mentor and guide as long as I can remember. I cannot thank enough my sister Ms. Azadeh Pourabdollah-Nezhad my brother in law Mr. Alireza Abedi, my aunt Ms. Fatemeh Nashvadian-bakhsh and Dr. Hamid-Reza Ebrahimi-Vishky for their support, all these past years.

Siamak P. Nejad -Davarani

CONTENTS

LIST OF FIGURES

LIST OF TABLES

ABSTRACT

Dynamic Contrast-Enhanced Imaging (DCE) is one of the main tools for in vivo measurement of vascular properties of pathologies such as brain tumors. In DCE imaging, one of the key components for estimation of vascular perfusion and permeability parameters using Pharmacokinetic models is the Arterial Input Function (AIF). To measure these parameters more accurately, there have been many approaches for estimating the AIF profile at the capillary level; however, a practical and realistic estimate is still missing.

As a solution to this problem, we have developed a model of the brain vascular system, based on laws of fluid dynamics and vascular morphology, to address dispersion and delay of the contrast agent (CA) concentration profile at different levels of the brain vascular tree. Using this model, we introduced a transfer function that can describe changes of the AIF profile along a vascular pathway, from a major artery to the capillary bed. Our simulations and also testing this model on DCE Computed Tomography (DCE-CT) and Magnetic Resonance (DCE-MR) Imaging data of the human brain, all showed that our model can give a realistic estimation of the CA concentration profile, at all levels of the vascular tree in the brain.

In the next step, to apply this model to pathologies such as brain tumors, in which leakage of the contrast agent to the extravascular-extracellular space (EES) can happen, we extended our model to address vascular leakage as well. Using this extended vascular (EV) model, we are able to decompose the tissue response signal in DCE images to its intravascular and EES components. This feature has provided us with an excellent tool that can lead to relatively unbiased measurements of perfusion and permeability parameters, especially in areas with vascular leakage. We tested this on DCE-CT and DCE-MR images and compared the performance of our model to conventional methods. Also, using a simulation study, we measured the levels of overestimation and underestimation of the permeability parameters using conventional processing methods and demonstrated the superior performance of the EV model for more accurate estimation of these parameters.

Overall, the results show that the EV model proposed in this study can provide a platform for better understanding of the role of the AIF in DCE studies as well as identification and estimation of AIF for more accurate measurement of perfusion and permeability parameters. This model can have a significant impact on the application DCE Imaging in clinical studies.

CHAPTER I

INTRODUCTION

In this chapter, the importance of the Arterial Input Function (AIF) and its significance for measuring the permeability and perfusion parameters in Dynamic Contrast Enhanced (DCE) imaging is reviewed. The problems associated with the conventional use of AIF in these studies will be introduced which is the motivation behind this dissertation.

Estimating the Arterial Input Function (AIF) of a Contrast Agent (CA), the time-concentration curve in plasma, especially at the tissue level, has long presented a problem in Dynamic Contrast Enhanced Magnetic Resonance (DCE-MR) and Dynamic Susceptibility Contrast Magnetic Resonance (DSC-MR) imaging Arterial Spin Labeling (ASL) and Dynamic Contrast Enhanced Computed Tomography (DCE-CT) studies. All these methods are based on changing the contrast of the images in the vascular areas by means of a tracer. This tracer can be endogenous (ASL) or exogenous (DSC-MR, DCE-MR and DCE-CT) [1].In the MRI field, DSC is the method of choice for perfusion studies in which Mean Transit Time (MTT) , Cerebral Blood Flow (CBF) and Cerebral Blood Volume (CBV) are estimated [2] and is based on changes of the T_2^* signal in the dynamic images[1]. In DCE-MRI studies, dynamic series of T1-weighted images are acquired and is mainly used for estimation of vascular permeability parameters such as vascular transfer rate constant (K^{trans}), vascular plasma volume (v_p), and extracellular-extravascular space (EES) volume (v_e) [3, 4].

One of the main components in the methods for estimating the parameters mentioned above is the AIF [5] Inaccurate estimation of the AIF for use in permeability and perfusion analyses could substantially add bias to the estimated hemodynamic and permeability maps. This is one of the main reasons for finding the Arterial Input Function (AIF) at the tissue level (which we will refer

to as “Tissue Input Function” or TIF). One approach towards this goal is modeling the vascular system in the brain and using that to find the dynamics of blood flow at the capillary (tissue) level which is the main focus of this dissertation

Some of the earliest studies to understand and quantitate the morphology of the vascular system and dynamics of blood flow was done by Cecil Murray [6, 7] in the early 20th century where the relationship between the rate of blood flow and the volume of the vessel and also his well-known arterial branching rule [7, 8] were interpreted based on the principle of minimum work. Another direction for measuring the blood flow is the “Indicator-Dilution Method” which is basically what DCE is based on. The first reported work in this field was done between 1824 and 1826 by Herring where he was trying to measure “velocity” in the blood circulation system by injecting ferrocyanide in the jugular vein of 14 horses and sampling it at other parts of their vascular system [9] In the late 19th century and early 20th century other scientists carried out experiments in this field. However the work done by Kenneth Zierler during the 1950’s and 1960’s set up the building blocks and equations of Indicator Dilution Theory (IDT) that we are using to this day [10-14].

In the past couple of decades, many researchers have attempted to model vasculature for applications in DSC and DCE studies. Depending on the applications, there have been different approaches to this problem, each having their advantages and shortcomings. In one study Calamante et al. proposed using Independent Component Analysis (ICA) in perfusion studies as a tool to define a local AIF for obtaining more accurate quantification of CBF in DSC-MRI studies [15]. Using the local AIF resulted in obtaining higher CBF and shorter MTT in areas with distorted AIFs which suggests minimized delay/dispersion. The method for finding the local AIF was based on a semi-manual approach and user input was required for choosing the components and also there was no method for validating the local AIF; another shortcoming of this method was the assumption that the AIF is similar between neighboring voxels. Mouridsen et al. defined a physiological estimation of microvasculature which was used for estimation of cerebral perfusion with Bayesian methods [16]. The model that they designed for microvasculature is basically a set of parallel delay lines each representing an arteriole and a capillary and each having a different transit time. The assumption for the AIF in this work was having a gamma-variate Probability Density Function (PDF) which is a simplified form of the actual AIF in

vasculature; this function or the exponential decay function for the local AIF are assumptions that have been used in other studies as well [17, 18].

Cebral et al. used noninvasive methods to develop detailed assessment of blood flow patterns from direct in vivo measurements of vessel anatomy and flow rates using finite element methods [19]. They used MR angiograms for imaging the Carotid artery in patients with stenosis, and blood flow was modeled in this artery for each patient. The goal of this work was characterization of blood flow patterns in healthy and diseased carotid arteries. The main attraction of this work is the detailed modeling of blood flow and turbulence at the bifurcation point in a major artery; however, the whole blood circulation in the brain and in smaller arteries and tissue was not modeled.

In a recent work, Li et al. created a method for tracking the AIF in DCE-MRI images of the breast [20]. However, this method was only focused on finding the voxels in the images that showed characteristics of being representative of the AIF and the goal of Li's work was not for finding a TIF.

Another approach was modeling the blood circulatory system of the whole body and finding the flow at different locations in the vascular system. In this category, Sherwin et al. built a one dimensional network based on space-time variables and linear and non-linear modeling [21]. They first derived the governing equations by considering the conservation of mass and momentum for a single one-dimensional vessel and they applied these equations to a network and adding the effects of bifurcation and dispersion. They tested this model on a network containing 55 arteries. Another modeling approach is Three-Dimensional One-Dimensional coupled models. The concept of a coupled model is based on having a Three-Dimensional arterial district embedded in a One-Dimensional representation of the arterial system [22] The use of Three-Dimensional One-Dimensional coupled models allows performing quantitative and qualitative studies about local and global hemodynamic quantities but none of the models above have addressed the model of the flow at the capillary (tissue) level and are useful mainly for modeling flow in arteries in healthy and abnormal conditions such as aneurisms. In another study, Bagher-Ebadian et al. suggested a model, based on the blood-circulatory system, for the construction of an algorithm for estimating the CA time-concentration curve in arterial plasma

after an intravenous bolus injection [23, 24]. A set of time courses of radiolabeled Gd-DTPA CA concentrations in arterial plasma (time–activity curve) after an intravenous bolus injection were measured by counting β emissions in a well counter for 13 Wistar rats. The measured AIF profiles were averaged and calibrated to blood relaxivity to construct a reference curve (ΔR1) for constructing a standard radiological AIF (SRAIF). Next, the SRAIF curve was used to estimate the blood-circulatory model parameters to construct a standard model based AIF in a high temporal resolution which can be adapted to any MR DSC and DCE studies [25]. This model based AIF (SRAIF) can be used in the animal model. The models suggested above mainly focus on estimating the AIF signal in major arteries. These models work reasonably when only a global AIF is used in the perfusion and permeability analyses.

As we mentioned, one application of AIF estimation is in ASL. One major difference between ASL studies and DCE-MR, DSC-MR and DCE-CT studies (which are considered CA based studies) is the profile of the bolus at the location of major artery entering the brain. In ASL, a square shaped bolus (which is considered as the ideal AIF in ASL studies [26]) is formed inside the major artery by radiofrequency excitation of the water protons in the arterial blood, which is then imaged after a delay, to allow the bolus of labeled blood reach the tissue of interest. Any modeling for finding the dispersion in the flow pathway in ASL can use the box-car bolus as the input. On the other hand, in the CA based studies, the CA bolus is injected intravenously and after arriving at the major artery in the brain, it totally gets deformed and dispersed. This point makes the models used in ASL studies (that assume the square shape for the bolus), not directly useable for the CA based studies. There has been considerable number of studies for modeling changes in the AIF for ASL applications. Some have used Gaussian kernels [27] or variations of it [28] for modeling dispersion of the AIF which provide plausible smoothening of the AIF box-car shape along the arterial pathway. Hernandez et al. previously presented a one dimensional model for ASL applications that takes into account the effects of transit times by modeling displacement and decay of the inversion tag between the tagging and imaging locations [29]. In this study, the numerical ASL model was based on a series of arterial compartments. Passing of the inversion tag through each compartment was characterized by the transport equation, a decay term and the exchange of the tag with the tissue. In the transport equation, the mean arterial velocity function was incorporated which reflected the changes of the transit time along the path. Also, to take into account the dispersion effects of the laminar flow, the AIF was smoothened

using a Gaussian kernel. In another study, Kazan et al. modeled the effects of dispersion in Arterial Spin Labeling (ASL) [30]. In their model, the mass transport equation has been used to model the transport of the ASL signal from the tagging band to the imaging band. They have accounted for flow dispersion through the use of a more physically realistic representation of the transit of the bolus compared to the existing ASL models and they have managed to get more accurate results using the dispersion model; in neither of the studies above has the effects of multiple pathways of flow through the vasculature been considered for modeling the overall dispersion. In another study dispersion of the AIF was modeled based on laminar (parabolic) and pulsatile flow of blood in major arteries [31]. Since this model was designed to address the signal changes for applications in ASL, it had incorporated parameters and components such as the tag delivery function and decay function which are relevant to ASL studies. The result of this work is a four phase equation describing the effects of labeling the cross section of a tube (in the form of a square label profile), after moving a certain distance from it to the imaging location. The advantage of this model was considering the effects of blood flow, including laminar and pulsatile flow in the model; however, this was designed only for ASL applications and also it was considering only a single tube with no branching which is the real case in all vascular structures. Later Chapelle et al. used a variation of this model with adding a gamma-variate kernel to address dispersion in ASL [26]. Using Dynamic Angiographic measurements in major arteries, this study showed that the gamma-variate model can explain dispersion of the ASL bolus in these arteries.

One issue with the suggested models in DCE studies is clinically validating them and the estimated parameters in the human brain [32]. Although there have been attempts to address this issue by developing phantoms to simulate perfusion, most of these systems fail to establish and accurately replicate physiologically relevant capillary permeability and exchange performance. One approach to solving this problem has been using concepts of physics and transport phenomena for better understanding of contrast agent kinetics. In one approach, Peladeau-Pigeon and Coolens [32] used the results of a Computational Fluid Dynamics (CFD) simulation and DCE-CT data obtained from a flow phantom to test Tofts [33] enhanced model and Fick's principle [34] The phantom used in this study contained a single tube. As will be discussed later in this dissertation, we have used a similar approach for simulating such physical model;

however, effects of dispersion due to vascular branching and flow have also been incorporated in our model.

The methods discussed above show different models for the AIF but these models either represent the input function only at the level of the major arteries (such as the carotid artery) or if they have an estimation of the input function at a lower level, the model does not represent all the major parameters that affect the AIF at the capillary level. Here we introduce a method that not only presents an analytical approach for modeling the dispersion in major arteries at different levels of branching, but is also able to present a model of the TIF using Laws of fluid dynamics and morphological properties of the vessels.

In Chapter II first a brief overview of vascular neuroanatomy and hemodynamics will be given. Next we will introduce the parametric equation of the transfer function of a single vessel that we have calculated and based on that we will present our basic model of the vascular structure of the brain. In Chapter III, initially a method will be introduced based on fitting and model averaging, to be used for finding the branching level and vascular characteristics of the vessel that the CA profile is sampled from. Next the results of testing this method on simulated data and DCE-CT images will be presented after that the software platform for processing the DCE images using this method is introduced. Chapter IV starts with reviewing the concepts of Indicator-Dilution Theory and the Pharmacokinetic Model. After that, the methods that we have developed for estimating T1 maps and also the $\Delta R1$ signal will be discussed. Next, the models of vascular leakage will be introduced and then we will describe our method for finding permeability parameters using fitting and model selection. In Chapter V we will introduce the extended vascular model which combines the basic vascular model with the concept of vascular leakage. In this chapter, the application of this method for decomposing the tissue response signal into intravascular and extravascular components is explained and the results of testing the model on DCE-CT and DCE-MRI images are presented. The main focus of Chapter VI is on comparing the effects of using different AIFs on the estimated values of the permeability parameters. The AIFs discussed in this chapter are the Manually Selected AIF (MSAIF), Standard Radiological AIF (SRAIF), and the TIF found using our Extended Vascular Model. Also results of using $\Delta R1$ vs. DCE-T1 signal intensity for calculation of permeability parameters are compared. At the end

of this chapter, the advantage of the Extended Vascular Model for perfusion studies is discussed. Finally, in Chapter VII, we will present the conclusions of our research.

CHAPTER II

VASCULAR MODELING OF THE BRAIN

This goal of this research is finding an estimate of dispersion of the contrast agent profile in the brain tissue and different layers of the vascular structure. For this reason, knowledge of the vascular anatomy of the brain and also dynamics of blood flow in these vessels is necessary. In this chapter, after addressing these, a model will be introduced that can analytically model dispersion of the contrast agent profile in the brain vascular structure.

2.1 Vascular Anatomy of the Brain

In this research, our goal is finding dispersion of the contrast agent profile at the all vascular levels in the brain, from the main arteries entering the brain to the veins that collect the blood from the venules and capillaries and exit the brain. One critical point is the fact that more than one artery enters the brain and it is critical to study the anatomy of these vessels and for finding the relationship of the contrast agent profile at the entry point of these vessels to the brain and also how these vessels branch into the brain.

2.1.1 Anatomy of Arteries between the Heart and the Brain

Figure 2.1 shows the fontal view of the arteries connecting Aorta to the brain [35]. As seen here the right common carotid artery begins at the bifurcation of the brachiocephalic trunk and the right vertebral artery originates from the right subclavian artery which is also a branch of the brachiocephalic trunk. In contrast, the left common carotid artery branches out directly from the aortic arch and the left vertebral artery arises from the left subclavian artery. Both (left and right)

common carotid arteries bifurcate into the internal and external carotid arteries. The external branches of the carotid arteries basically feed the organs outside the brain, such as the facial and lingual structures and don't enter the brain. The Left and Right Vertebral Arteries join together to form the Basilar Artery. This Artery along with the Left and Right Internal Carotid Arteries are the main arteries that flow into the circle of Willis (Figure 2.2) to supply the brain tissue.

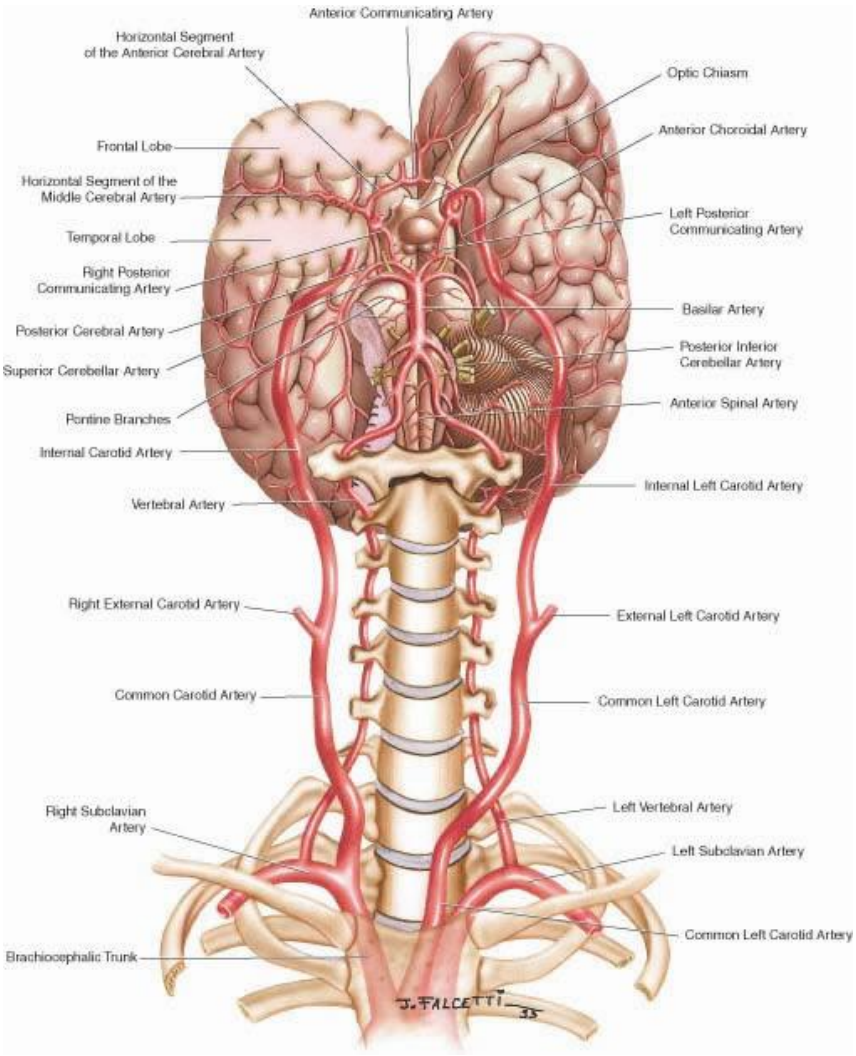

Figure 2.1. Frontal view of the main arteries entering the brain. Here, the vertebral arteries, carotid arteries and intracranial vessels are seen. The main arteries that enter the brain are the left and right Internal Carotid Arteries and the Basilar Artery. (Figure courtesy of Renan Uflacker. Atlas of Vascular Anatomy an Angiographic Approach: Second Edition. Philadelphia, Lippincott Williams & Wilkins © 2007)

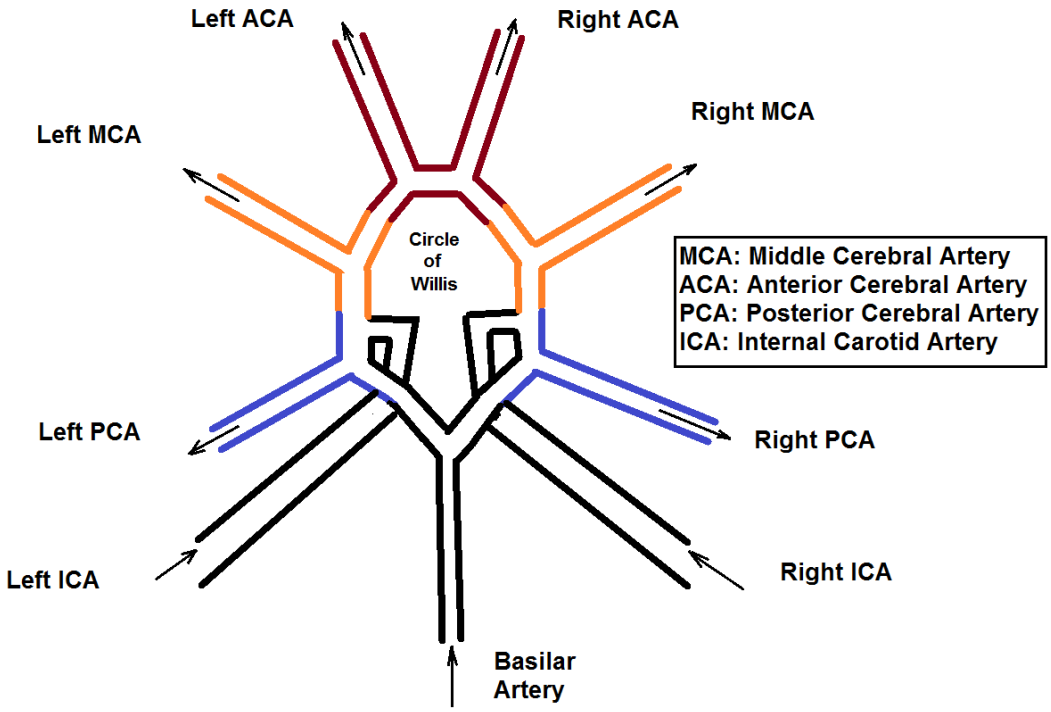

Figure 2.2. Schematic diagram of the circle of Willis and the major efferent and afferent arteries connected to it. The Left and Right Internal Carotid Arteries and the Basilar Artery are the main sources of blood flow into the circle of Willis and the blood is directed to the different cerebral regions through the Left and Right MCA, PCA and ACA. Considering the short vascular distance between the different efferent arteries and also the relatively low temporal resolution of the dynamic images, it is assumed that the profile of the CA entering each of these arteries is similar in these vessels.

2.1.2 Anatomy of Vessels Inside the Brain

As seen in Figure 2.2, after entering the circle of Willis through the Basilar and Internal Carotid Arteries, the blood flow gets divided into six main branches. These are the Left and Right Anterior Cerebral Arteries, Middle Cerebral Arteries and Posterior Cerebral Arteries [36]. Each of these arteries supplies a different region in the brain.

The goal of our study is to model the vascular trees in the brain and based on that, measure the dispersion of the contrast agent profile in the brain. Therefore, it is crucial to have a good estimate of the number of bifurcation levels of the vasculature after the circle of Willis. To this date the most extensive report for quantification of the global and local anatomical features of arterial vasculature can be seen in a study by Wright et al. [36]. In this study, using MR Angiograms from a human population of 61 subjects, the size, symmetry, branching characteristics, bifurcation angles, and path meandering of brain arteries have been measured.

According to this study, the maximum number of bifurcations in the three vascular trees are 6.15 ± 1.53 (ACA), 8.80 ± 1.40 (MCA), and 5.93 ± 1.66 (PCA). In our research, six levels was the maximum number of bifurcations that was considered.

2.2 Hemodynamics

Hemodynamics is the study of blood flow or blood circulation. It explains the physical laws that govern the flow of blood in the blood vessels. This is a vast field and addresses many different aspects of the vascular system. Here we only focus on a few concepts that we will be dealing with in our model.

Blood flow in the vessels is of pulsatile nature; however, as the blood flows from the major arteries into smaller arteries and arterioles the pulsatile effects of the blood get reduced and get closer to continuous flow. The flow of blood in the vascular system can be divided into three types:

- Turbulent flow
- Laminar flow
- Plug flow

The first two types of flow are seen in larger vessels while plug flow occurs in capillaries in which the white and red blood cells squeeze through the vessels as a solid mass. Figure 2.3 shows the pattern of the movement of fluid particles in a cylindrical tube for Turbulent and Laminar flow. In laminar flow, all the elements of the fluid move in streamlines parallel to the axis of the tube; but in turbulent flow, the elements of fluid move axial, radial and circumferential directions irregularly.

The occurrence of turbulent or laminar flow mainly depends on the Reynolds number (*Re*). *Re* is a dimensionless number that gives an estimate of the ratio of inertial forces to viscous forces. For a cylindrical tube [34]:

(2.1) $$Re = \frac{inertial\ forces/volume}{viscous\ forces/volume} = \frac{\rho v^2/L}{\mu v/L^2} = \frac{\rho L v}{\mu}$$

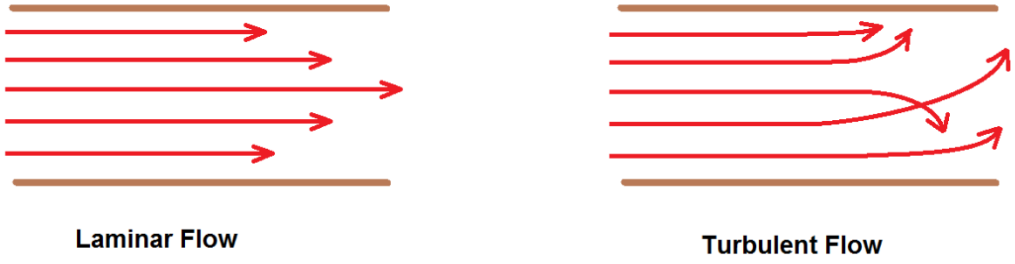

Figure 2.3. Movement of particles in Laminar and Turbulent flow in a vessel. In laminar flow, all the elements of the fluid move in streamlines parallel to the axis of the tube; but in turbulent flow, the elements of fluid move axial, radial and circumferential directions irregularly.

Here, ρ is the density and μ is the viscosity of blood. L and v are characteristics of length and velocity respectively. As seen here, the velocity of the fluid and the diameter of the vessel can increase the Reynolds number. Generally speaking, higher velocity and larger opening for the tube would lead to a higher Reynolds number. One of the main parameters that cause flow to switch between turbulent and laminar forms is the value of *Re*. For cylindrical tubes, flow is always laminar for $Re < 2100$ but if the inner walls of the cylinder are smooth and there are no vibrations, laminar flow can continue to happen up to *Re* values around 10,000. In section 2.3.1 we will talk more on the measured and estimated values for the Reynolds number of blood in major arteries and also based on the equation of the velocity of fluids in laminar flow, will model the flow of blood in vessels.

One of the parameters that we deal with when calculating the permeability parameters of vessels using the Pharmacokinetic model is the Hematocrit (Hct). Hematocrit is defined as the volume percentage of erythrocytes in blood [37] and is normally about 45% for men and 40% for women [38]. Another important concept that should be noted here is the Fahraeus-Lindquist Effect [39]. Based on this effect, when blood moves from larger to smaller vessels its viscosity decreases. This effect is mainly seen in vessels with a diameter below 0.3mm where the viscosity strongly decreases with the reduced diameter of the vessels. The result of this effect is the reduced resistance to blood flow in these vessels. Based on this effect, the relative hematocrit ratio of the blood will change as it moves from larger vessels to tissue. For more accurate solutions for the pharmacokinetic model, this should effect should be considered [40].

2.3 Modeling Blood Flow in the Vessels

In this section, the steps and building blocks of our vascular model is described. First, we describe the dispersion of the contrast agent profile in a single vessel due to the laminar flow of blood in large vessels and using that, we find a parametric expression for the transfer function of single vessel. In the next step, we model the morphological structure of vessels and finally, by combining these results, we model the overall transfer function of vessels in the brain.

2.3.1 Transfer Function of a Single Vessel

As mentioned in section 2.2, the flow of blood in vessels in the body can fall in any of the three categories of Turbulent flow, Laminar flow or Plug flow. One of the factors that determine the type of flow in vessels is the Reynolds number (*Re*). The value of Reynolds number in different vessels changes based on the diameter of the vessel and the velocity of blood. The vessel that has the highest value of Reynolds number is the Ascending Aorta which has a peak value of 4500 (and a mean of 750). Typically, turbulent flow starts at Reynolds numbers higher than 4000 [34]. The focus in this study is on vessels in the brain. The largest vessel entering the brain is the Internal Carotid Artery (ICA). The average *Re* for the ICA has been calculated to be 266 and 911 for the mean and peak flow rates respectively [41]. Also Laser Doppler measurements of 3D flow models of the ICA have given a value of 700 for the Reynolds number in these vessels [42]. Considering these reports, the possibility of having Turbulent flow in any of the vessels in the brain is excluded since they are less than 4000. Also, it is known that that in micro vessels, blood flows in the form of plug flow [34]. Based on this, for finding the dispersion, the focus will be on the arteries, arterioles, veins and venules in the brain where flow is laminar and dispersion due to laminar flow will be calculated.

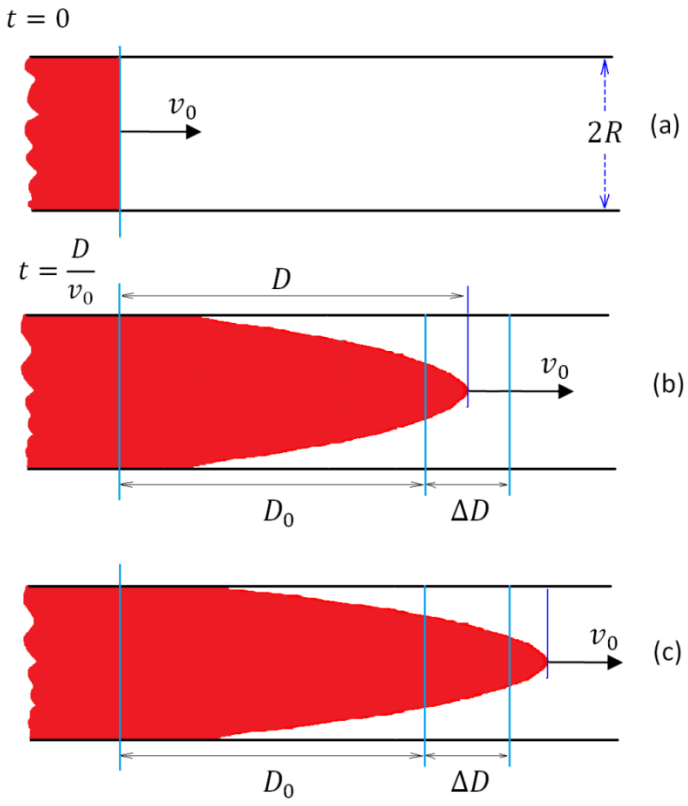

Figure 2.4. (a) Introduction of a contrast agent in the form of a step function to a vessel with laminar flow. (b) The parabolic form of the contrast agent after flowing the distance of D0 in the vessel at time t while entering the volume enclosed by planes at D0 and D0+ΔD (c) The next step where the tip of the parabola exits the enclosed volume.

Figure 2.4 shows the effect of laminar flow on the shape of the profile of the contrast agent along the vessel after it is presented to the entrance of the vessels as a bolus. In laminar flow, the velocity of the fluid in a tube is dependent on the radial distance to the center of the tube and can be characterized as [34]:

(2.2) $$v = v_0(1 - \frac{r^2}{R^2})$$

where v_0 is the velocity of blood along the central axis of the vessel (maximum velocity) with a radius of R. v is the blood velocity at the radial distance r from this axis. v_0 is calculated by:

(2.3) $$v_0 = \frac{\Delta p R^2}{4\mu L}$$

L and R are the length and radius (m) of the tube, Δp is the pressure drop across the tube (or the

pressure difference between the ends of the tube) (Pa) and μ is the blood viscosity ($Pa{\cdot}s$). In this study, considering the time resolution of DCE imaging, the effects of pulsatile flow of blood in the vessels are ignored and it is assumed that flow has reached a steady state; this indicates that the blood velocity in every vessel has a value that is dependent on the overall structure of the vascular system and it will be assumed that the effect of the whole system on flow has already taken place and has resulted in the maximum velocity being v_0 in this particular vessel and from this point on, v_0 will represent the flow in the vessels.

As shown in Figure 2.4-a, contrast agent is introduced to the entrance of the vessel in the form of a step function. The goal is to find an equation that shows the concentration of the Contrast Agent (CA) in the volume enclosed by the two planes at D_0 and $D_0 + \Delta D$, as a function of time. We will use this equation to find a transfer function for this vessel.

The equation of the surface of the parabola is written as:

(2.4) $$z = v_0(1 - \frac{r^2}{R^2})t$$

As seen in Figure 2.4-b, initially the CA enters this space between the two planes, but does not pass through the second plane. For calculating the transfer function of the vessel, we assume the condition where the tip of the parabola has crossed the second plane and ΔD is assumed to be small. Considering these conditions, at the intersection of the parabola and the D_0 plane, the following equation holds:

(2.5) $$D_0 = v_0(1 - \frac{r_1^2}{R^2})t$$

Where r_1 the radius of the circular is cross section of the parabola and the D_0 plane and t is the time taken for the CA to reach the D_0 plane at the r_1 radius.

The shortest time for the bolus to reach the D_0 plane is defined as t_0:

(2.6) $$t_0 = \frac{D_0}{v_0}$$

By rearranging Equation 2.5 and using Equation 2.6, we have:

(2.7) $$r_1^2 = R^2(1 - \frac{t_0}{t})$$

Using r_1, the volume of the parabola (CA) enclosed between the two planes is calculated as:

(2.8) $$V_{CA} = \pi r_1^2 \Delta D$$

And by dividing this volume by the total cylinder volume enclosed between the two planes, the CA concentration in this segment of the vessel can be found:

(2.9) $$CA_c(t) = \frac{V_{CA}}{V_{Cyl}} = \frac{\pi r_1^2 \Delta D}{\pi R^2 \Delta D} = (1 - \frac{t_0}{t})$$

This equation shows the CA concentration with respect to time for a step function as the input. If the time derivative of the equation is calculated, the response to the delta function or in other words, the transfer function can be calculated. By calculating the derivative with respect to time, the impulse response or transfer function of a single vessel can be found:

(2.10) $$h(t) = \frac{t_0}{t^2}$$

Considering the fact that the no contrast agent passes through the D_0 plane before time t_0, the transfer function of a single vessel is as follows:

(2.11) $$h(t) = \begin{cases} 0 & t < t_0 \\ \frac{t_0}{t^2} & t \geq t_0 \end{cases}$$

D_0 is the length of the vessel and v_0 the maximum velocity of blood in that vessel so t_0 is the shortest time that the contrast agent takes to reach the end of the vessel. Figure 2.5 shows the plot of the transfer function of a single vessel. Using this transfer function and by knowing the flow rate in a cascade of the vessels, the transfer function at each node in the network can be found by convolving the transfer functions. This will be discussed in the next section.

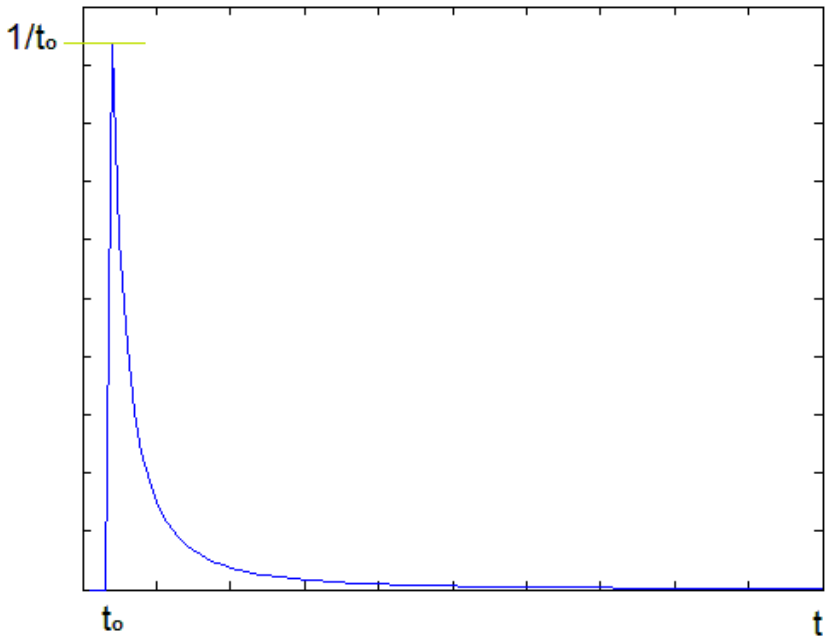

Figure 2.5. Plot of the transfer function of a single vessel. t_0 represents the time the tip of the CA parabola reaches the end of the vessel.

2.3.2 Three Dimensional Model of the Brain Vascular Structure

After calculating the transfer function of a single vessel, the next step is finding the transfer function (and distortion) of a cascade of branching vessels such that the morphological model of the brain vasculature is implemented and the flow and distortion at each level is calculated. For this purpose, a model of the vessels was designed for finding the flow and dispersion from an artery to arterioles down to capillaries and from those to the venules and veins. Figure 2.6 shows the Three-Dimension representation of this model. In this model, the artery at the first level is assigned a diameter and flow value close to those of the three main arteries branching from the circle of Willis. At the end of this vessel, bifurcation happens and two daughter vessels are created. The radii of these daughter vessels are found based of Murray's branching law of vessels [6, 8]. Based on this law, the radii of the three vessels are related through the following equation:

(2.12) $$r_P^3 = r_{d1}^3 + r_{d2}^3$$

Where r_P is the radius of the parent vessel and r_{d1} and r_{d2} are the radii of the two daughter vessels. In this model, first r_{d1} is selected randomly as a fraction of r_P and next, r_{d2} is calculated

based on Murray's law, and the values of r_P and r_{d1}. The length of the daughter vessels are also selected randomly within a certain range as a fraction of the length of the parent vessel. Using the same procedure for creating the daughter vessels, based on a recursive rule, the branches can be created to as many levels as desired. To follow the branching in the brain down to the capillaries, this is repeated up to 6 levels. The vessels at the 6th level represent the last level of arterioles. The reason for selecting 6 levels will be discussed in section 2.2.2.

After implementing the morphological model of the vascular structure, the next step is calculating the flow rate in the branches. Volumetric flow rate is defined as [34]:

(2.13) $$Q = \langle v \rangle A$$

Here, $\langle v \rangle$ is the mean velocity of fluid and A is the cross sectional area of the vessel. In laminar flow [34],

(2.14) $$\langle v \rangle = \frac{1}{2} v_0$$

In branching vessels, the volumetric flow rate of a non-compressible fluid can be calculated as follows:

(2.15) $$Q_P = Q_1 + Q_2$$

This means that the volumetric flow rate of fluid in the parent branch (Q_p) equals the volumetric flow rate in the daughter branches (Q_1 and Q_2). Accurate calculation of the ratio of the flow rate in the daughter branches requires knowing many parameters such as the angle between the branches and also knowing the flow resistance all the way to the capillary bed [34]. For finding this ratio in our model, the resistance of the all vessels was found and using the electric circuit analogy [43], the flow in all branches was calculated.

The next level in the vascular system following the arterioles is the capillary bed. In our model, for implementing the capillary bed, certain assumptions have been made: First, it is assumed that every section of the capillary bed is fed by only one arteriole and the efferent blood from each section is collected by only one venule. Next, it is assumed that flow in the capillaries is not laminar but in the form of plug flow. In this case, no dispersion due to laminar flow would be

seen in these microvessels. The capillary bed can be considered as a network of microscopic vessels that form a grid. The whole capillary network between the arteriole and venule has been modeled as a single vessel of larger diameter with non-laminar flow. This will basically cause only a delay in the flow of blood entering the veins and venules. However, when estimating the TIF in images, one consideration should be the possibility of sampling from an area where the capillaries are being fed from more than one venule and the resulting signal being the result of CA profiles; this condition will be addressed later in the following sections, when model averaging technique is discussed.

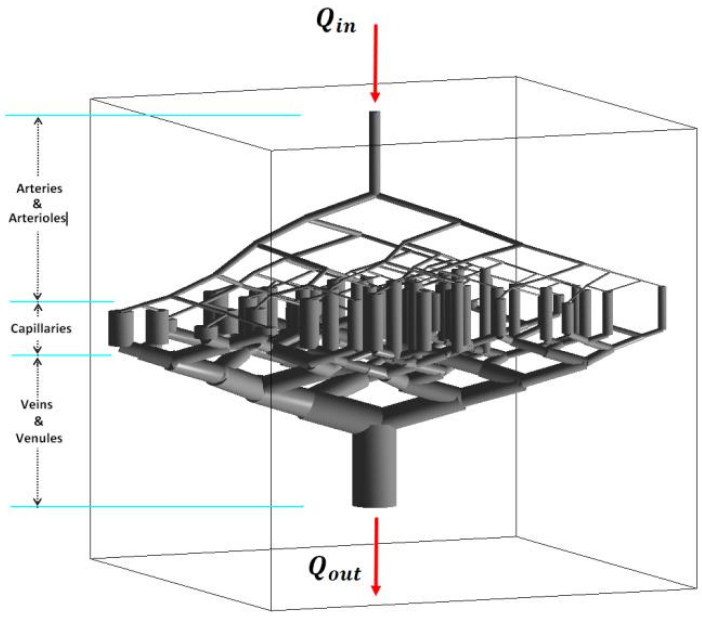

Figure 2.6. Morphological structure of the vascular model; branching of arteries and arterioles has been done down to six levels. As seen here, the veins and venules have a larger volume and diameter compared to arteries and arterioles. The volumetric flow rate of blood entering this model equals the efferent flow. Every segment of the capillary bed is modeled as a single tube vessel in which the flow is non-laminar.

The diameter of venules and veins that return the blood from the capillaries is large enough to have flow in laminar form in them. Therefore, the transfer function of these vessels is similar to the arteries. However, one point that has been considered in our model is the larger diameter and overall luminal volume of the veins and venules compared to the arteries and arterioles. The overall volume of veins and venules is about 4 times that of arteries and arterioles [34]. This is a

natural effect for dealing with the pressure drop of blood after passing through the arteries and capillaries.

2.3.3 Transfer Function of the Brain Vascular Ensemble

The next step in implementing the vasculature model is finding the transfer function of the vessels between the input artery and nodes in the structure. This is done by combining the transfer function of the single vessel and the overall structure of the vessels which we introduced in the previous two sections.

Equation 2.11 shows the transfer function of a single vessel. In the situation that there is a cascade of vessels, the overall transfer function of the vessels from the input node to any node in the system would be the convolution of the transfer functions of the individual vessels to that node. In this case the transfer function of each vessel can be written as follows:

(2.16) $$h(t)_1 = \frac{t_{01}}{t^2} \quad for \ t \geq t_{01}$$

(2.17) $$h(t)_2 = \frac{t_{02}}{(t-t_{01})^2} \quad for \quad t \geq t_{01} + t_{02}$$

(2.18) $$h(t)_3 = \frac{t_{03}}{(t-t_{01}-t_{02})^2} \quad for \quad t \geq t_{01} + t_{02} + t_{03} \ldots\ldots\ldots$$

(2.19) $$h(t)_n = \frac{t_{0n}}{(t-t_{01}-t_{02}-\cdots t_{0n-1})^2} \quad for \quad t \geq t_{01} + t_{02} + \cdots + t_{0n}$$

In these functions, t_{01} to t_{0n} are the time delays of each individual vessel along the branching route, from the opening of the main artery down to the nth branching layer. The transfer function of the vessels from the input to the nth level of sub-branches is:

(2.20) $$h(t)_{1\ to\ n} = h(t)_1 * h(t)_2 * \ldots * h(t)_n$$

It should be noted that when calculating the transfer function of the cascade of the vessels, the delay of the transfer function of each segment will be calculated independent of the common time origin and the equation will be similar to the equation of the first segment but with the t_0 of that segment. After implementing the vascular model described in section 2.1.2, by assigning a

flow to the input artery, the flow to all the vessels in can be found. This, along with the physical characteristics of the vessels in the model can all be used to find the parameters of the transfer function (which are basically the time delays of the segments). Figure 2.7 shows the transfer functions between the opening of the main artery to the end of each of the vessels in the vascular structure, down to the sixth layer of branching in one vascular line. The gain of these transfer functions are arbitrary and the area under all these curves have been normalized to a common value. As seen here, as the level increases, the transfer function gets more spread out in the time domain and also the arrival time increases. The arrival time actually represents the time delay of the vessel.

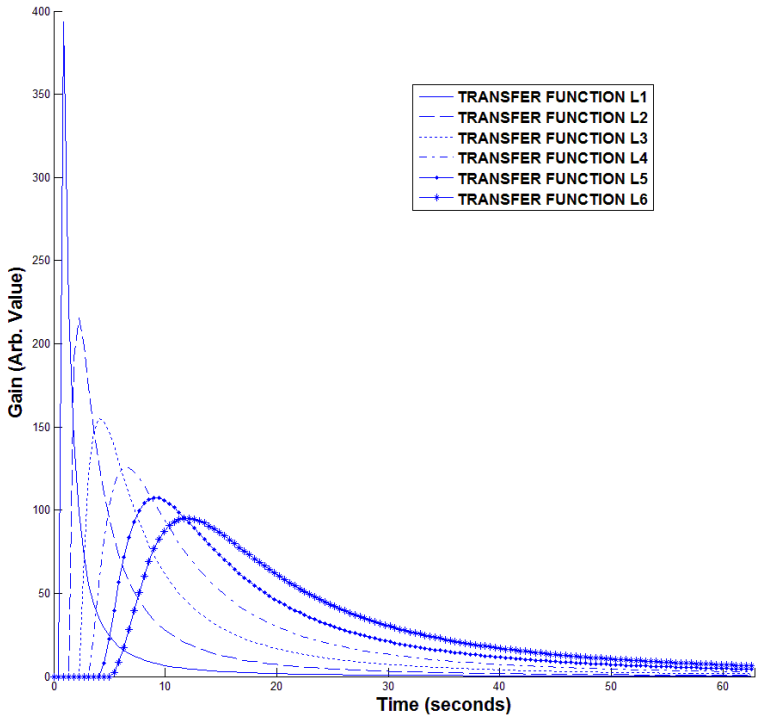

Figure 2.7. The transfer function of vessels from the opening of the main artery down to the 6th level of the vascular branching. As seen here, as the level increases, the arrival time and dispersion both increase. The total delay time at the last branching level is about five seconds.

CHAPTER III

TESTING THE VASCULAR MODEL WITH DCE IMAGING

The next step in the vascular model development was testing the model. For this purpose, a modality of dynamic imaging was needed for investigating the changes of the CA concentration profile in main arteries and tissue and to use them to find the transfer function that relates them and try to match that with the parameters of the transfer function of our model. In this chapter, first we will describe our methods for finding the vascular branching level of a CA profile. And next, we will test these methods on simulated data and data from human studies.

3.1 Steps for Finding the Vascular Branching Level from the CA Profile

Our goal here is to test the model and the transfer function that were introduced in the previous chapter. We present a platform here, to estimate a transfer function, that when presented with a global AIF and the CA profile of any voxel in a DCE image series, it would give an estimate of the level of that voxel in the vascular tree of the brain. The main blocks of this platform are the fitting and the model selection methods.

3.1.1 Fitting the Models to the Data.

Every voxel in the image volume belongs to one part of the vascular tree or the capillary bed; however, except for a few major vessels, it is not visually possible to follow the level of vessels in the branch hierarchy. The goal is to determine the likelihood of each voxel belonging to different branching levels of the vascular tree structure. The first step is estimating a transfer function which when convolved with a global AIF, can result in the CA concentration profile of

a voxel (Figure 3.1).

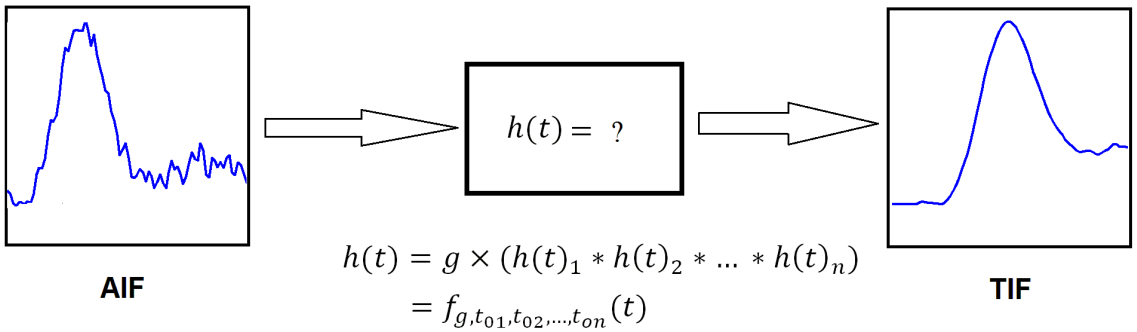

Figure 3.1. System for finding parameters of the transfer functions that transform the AIF to the TIFs that are measured for every voxel in the brain.

It should be noted that $h(t)_{1\ to\ n}$ denotes the transfer function between the main artery and only one branch at the n^{th} level; however, when the branching level increases, the diameter of the branches get smaller and the intensity of the signal from each single branch decreases. When the signal is sampled in an image, many branches may fit in an area the size of one voxel. To compensate for this fact, a gain factor g, was added to the transfer function. The new equation of the transfer function can be written as:

$$h(t)_{1\ to\ n} = g \times (h(t)_1 * h(t)_2 * \dots * h(t)_n) \tag{3.1}$$

This equation shows the general expression for $h(t)_{1\ to\ n}$, the transfer function between the first and the n^{th} level of branching. The global AIF profile is defined as $AIF(t)$ and the tissue input function in an arbitrary voxel in the brain image as $TIF(t)$. The relationship between these two can be defined as:

$$TIF(t) = AIF(t) * h(t)_{1\ to\ x} \tag{3.2}$$

where x is the branching level of the vessels at that voxel which generally speaking, is initially an unknown value and the goal is to determine the possible value (or values) of x for that voxel.

Prior knowledge about the cerebral vascular anatomy and morphology of the cerebral vascular trees can help find the limit on the number of branching levels in our model. The three main

arterial branches originating from the circle of Willis are the Anterior Cerebral Artery (ACA), Middle Cerebral Artery (MCA) and Posterior Cerebral Artery (PCA) [35] as seen in Figure 2.2. Each of these major vascular trees feeds a different part of the brain, but since they all originate from the circle of Willis, considering the relatively low time resolution of the imaging modalities, it is assumed that the CA profile in the blood entering these three branches is the same. Wright et al. have done a comprehensive measurement and morphology analysis of human brain arterial vasculature using Magnetic Resonance Angiography (MRA) among 61 health volunteers [36]. According to their measurements, the maximum number of bifurcations in the three vascular trees are 6.15 ± 1.53 (ACA), 8.80 ± 1.40 (MCA), and 5.93 ± 1.66 (PCA). Based on these values, to find the branching level *x*, at each voxel, it is assumed to have any of the values from 1 to 6. According to equation 3.1, $h(t)_{1\ to\ n}$ is a function of *n+1* parameters where t_{01} to t_{0n} indicate the delay of every branch from the main artery to the n^{th} branching level and g is a gain factor.

Using the simplex method [44] as a non-linear fitting method and the sum of squared errors as the cost function, for every possible configuration of the transfer function ($h(t)_{1\ to\ 2}$, $h(t)_{1\ to\ 3}$,… or $h(t)_{1\ to\ 6}$) as described by Equation 3.1, the best function that can transform the reference $AIF(t)$ to $TIF(t)$ is found. This results in six different sets of optimal parameters (each consisting of $[g, t_{01}, t_{02}, \dots t_{0n}]$ where *n* varies from 1 to 6). The next step is determining the best set of parameters among these six that can describe the transfer function between the main artery and that specific voxel. The order of this function can define the level of vascular branching in that voxel and the sum of the t_0 parameters can determine the CA arrival time to that voxel.

3.1.2 Model Selection and Model Averaging Using Akaike Information Criterion (AIC)

After finding the six best transfer functions (one for each of the one to six branching layer configurations) or models for every voxel, the problem of determining the contribution of each model needs to be addressed; this is necessary since each voxel might be representing a combination of tissue or vessels (from different layers of the vascular structure); or if it is the representative of only one vessel or tissue type, the branching level of the vessel at that voxel needs to be estimated. Two methods that can be used for model selection and model averaging

are Akaike Information Criterion (AIC) [45] and Bayesian Information Criterion (BIC). According to the principle of parsimony, if equal conditions exist, the model with lower number of parameters should be selected over more complex ones. Both of these methods satisfy this principle by penalizing the models by the number of parameters. One of the advantages of AIC over the BIC is the fact that AIC penalizes the number of parameters less strongly than BIC [46] and since one of the main distinctions between the different models here is the number of parameters, results would have been more biased towards the lower level models if BIC was used. Considering these facts, the AIC method was used to find the goodness of fit of these models.

In the general case, for a statistical model, the AIC value is defined by:

(3.3) $$AIC = 2k - 2\ln(L)$$

where k is the number of parameters of the model and L is the maximized value of the likelihood function of that model. *AIC* can also be calculated using the residual sums of squares:

(3.4) $$AIC = 2k + n\ln(\frac{RSS}{n})$$

As a rule of thumb, if $\frac{n}{k} < 40$, bias adjustment needs to be done and *AIC* will be calculated as[46]:

(3.5) $$AIC = 2k + 2\frac{k(k+1)}{n-k-1} + n\ln(\frac{RSS}{n})$$

n is considered to be the number of observations (or in our study, the number of timepoints), and is 99 for all models; k varies from 2 to 7 for models one to six respectively. The *AIC* values for these five models are named AIC_i where i=1 to 6. The best fit model is the one with the lowest *AIC* value which we name AIC_{min}. The goal is to find the likelihood of each of these six models being the best fit model for every voxel. To find these likelihood values, the Akaike weights are estimated. First a new variable Δ_i is defined that represents the difference between the *AIC* values in these six models with the lowest *AIC* value:

(3.6) $$\Delta_i = AIC_i - AIC_{min} \qquad for\ i = 1,2,\dots 6$$

Using Δ_i the Akaike weights are calculated as:

(3.7) $$w_i = \frac{\exp(-0.5\,\Delta_i)}{\sum_{j=1}^{6}\exp(-0.5\,\Delta_j)}$$

w_i is considered to be the probability of model i being the best model that describes the transfer function between the main artery and the voxel being studied.

3.1.3 Delay maps

As explained in section 2.1.1, every transfer function is described with a set of parameters $[g, t_{01}, t_{02}, \ldots t_{0n}]$. In this set, every t_0 represents the shortest time that blood takes to pass through the vessel segment; or in other words, it is the time that the fluid flowing with the velocity on the central axis (maximum velocity of the laminar flow) would take to pass through that particular vessel branch. In the case of dealing with only one model, by adding all these t_0 values from the best fit transfer function from that model, the total delay time from the main artery opening to the voxel being studied (or the arrival time of the contrast agent for that voxel) can be calculated; however, in this study since multiple models are used, the delay time of each voxel is estimated by calculating a weighted sum of the delay times of all models, with the weights being the Akaike weight or the likelihood of each model being the best fit model for that voxel:

(3.8) $$t_{Total} = \sum_{i=1}^{6} w_i \times \sum_{j=1}^{i+1} t_{0j}^{i}$$

Where t_{0j}^{i} is the t_0 of model i at the j^{th} level of branching. The benefit of using this model averaging method [47] for calculating the delay time is that voxels representing tissues that are being supplied by more than one branching level of the vascular system will have all those vessels accounted for and the delay time will be a weighted average of all the possible delay times from different vascular pathways.

3.2 Simulation results

Prior to applying our method to human data for estimating the vascular transfer function in these images (as explained in section 3.1.1), a simulation of the blood flow in our vascular model was performed to explore the feasibility of using this method for estimating the vascular transfer function parameters.

3.2.1 Simulating the Size and Flow Rate of the Model Based on Real Life Measurements

The first step in our analysis was designing the model with sizes comparable to real life values. The diameter of the common carotid artery in healthy adults has been estimated to be [48] 6.0 ± 0.8 mm and the mean diameter of the ICA has been measured to be 4.66± 0.78 mm and 5.11±0.87 mm in women and men respectively [49]. The mean velocity of blood passing through the Internal Carotid Artery (ICA) and Middle Cerebral Artery (MCA) has been measured to be 32.7 ± 3.0 cm/s and 58.1 ± 8.6 cm/s respectively in normotensive adults [48]. These values were used as the starting points of our model implementation. Based on the findings of Wright et al. the mean and standard deviation of the branch lengths in the brain is 25.02 ± 2.71 mm (19.35 mm-30.14 mm). To find the radii of the sub-branches of each branch, we randomly selected the radius of one of the sub-branches a value between 0.77×R and 0.83×R (where R is the radius of the mother branch) and the radius of the next one was calculated based on Murray's law (Equation 2.12). The length of the main branch of our model was set to 4 cm based on these reported values. As the length of every sub-branch, we assigned a random value from 50% to 70% of the length of its mother branch. Using these initial values and branching rules, our model was implemented with six levels of branching as in Figure 2.6 down to the capillary level and the veins and venules were implemented as the mirror image of the arteries and arterioles, albeit with a larger diameter to compensate for the pressure drop along the vessels. The flow in every vessel in this model was calculated by finding the resistance of every branch based on Poiseuille's law [34] and by converting the model to an analogous electric circuit and finding the electric current in all branches based on Ohm's law [43].

It should be noted that when finding the flow values in the branches, we assume a steady blood flow in all branches which does not change with time, neither locally nor globally. After finding the blood flow of all branches in the model, the time delay (t_0) of each branch was calculated based on Equation 2.6. Next, a node was randomly selected on the sixth level and the time delay of all the branches connecting the main artery to that node was found; using Equation 2.20, the vascular transfer function between the opening of the main artery and every node was estimated. Using the profile of the contrast agent in the carotid artery of a human subject in a CT-DCE image (Which will be described in detail in section 3.4) and the six transfer functions between the main artery and every node in the pathway described above, TIF at every node was

calculated by convolving this AIF with each transfer function. Figure 3.2 shows the AIF and the TIFs at the six levels. For better visual comparison of these curves, the peaks are all scaled to the same level as the AIF. As seen here, by moving to higher levels of the vascular tree, the arrival time of the CA profile increases and it gets more dispersed. By creating these TIFs, our goal was to:

(1) Explore the feasibility of our method for determining the level of the a TIF based on the transfer function that transforms the AIF to it and

(2) Test our method for separating the TIFs from two different levels when added together to form a composite signal.

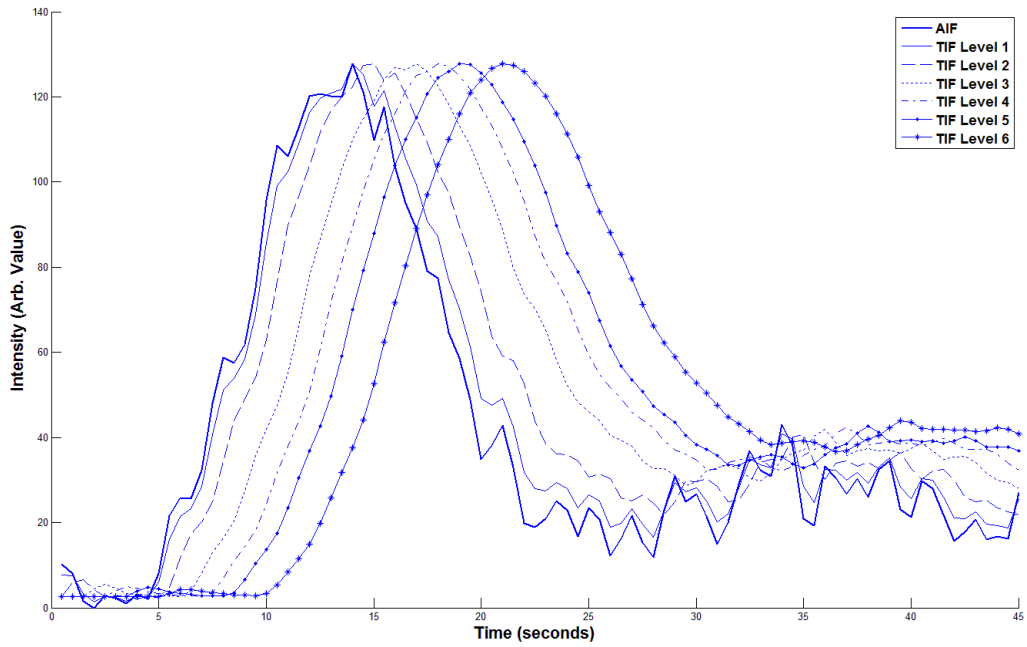

Figure 3.2. Plots of the main AIF (bold curve) of a human subject along with the TIFs at six levels of our vascular model. These are estimated by convolving the main AIF with the transfer function at each level. The AIF was sampled from the first 45 seconds of the DCE-CT image series in the voxels showing the Internal Carotid Artery of a human subject after the bolus injection of the CA. For easier comparison of the profile of these curves, the peaks are scaled to the peak of the AIF. As seen here, by moving to the higher levels of the vascular structure, the arrival time delay gets longer and the curves get more dispersed.

3.2.2 Estimation of the Branching Level of the Simulated TIF

The goal of the first part of our simulation was to explore the ability of our method for finding the correct transfer function of different nodes in the vascular structure, based on the AIF and the simulated TIF's based on the method explained in 3.1. Using the fitting procedure in 3.1.1 and the model selection method in 3.1.2 the different models were fit to each of the six TIF's and using the residue and the Akaike method, the likelihood of these TIF's belonging to each of the different models was estimated. This simulation was repeated by adding different levels of noise to the TIF's. Figure 3.3 shows the results of this simulation. As seen here, the added noise level is varied from 0% to 100% and at each of these levels, the likelihood of selecting the correct level of the vascular structure has been estimated. Up to 18% of noise level, the likelihood of picking the correct level of the TIF is almost 1 for all cases. As the noise level increases, the accuracy of the system decreases and the likelihood of picking the correct model is reduced; however, in the 100% noise level, the probability of picking the correct level index does not go below 0.45.

3.2.3 Decomposing the Simulated Composite TIF

In real applications, when the CA concentration profile is being sampled from a typical voxel in a DCE image series, considering the size of the vessels and the complexity of the vascular network in the brain, it is very likely that each voxel would be representing a composite of vessel segments, originating from more than one level of the vascular tree. As will be explained in section 3.4, when applying our method to the DCE images, this fact has been considered and the likelihood of presence of different levels of the branches of the vascular tree in each voxel is estimated. To explore the feasibility of this method for finding the likelihood of presence of signals from each level of the vascular structure, the superposition of the CA profile from two levels of the model was simulated and in the next step decomposed by the fitting algorithm and by applying the AIC method as explained in sections 3.1.1 and 3.1.2.

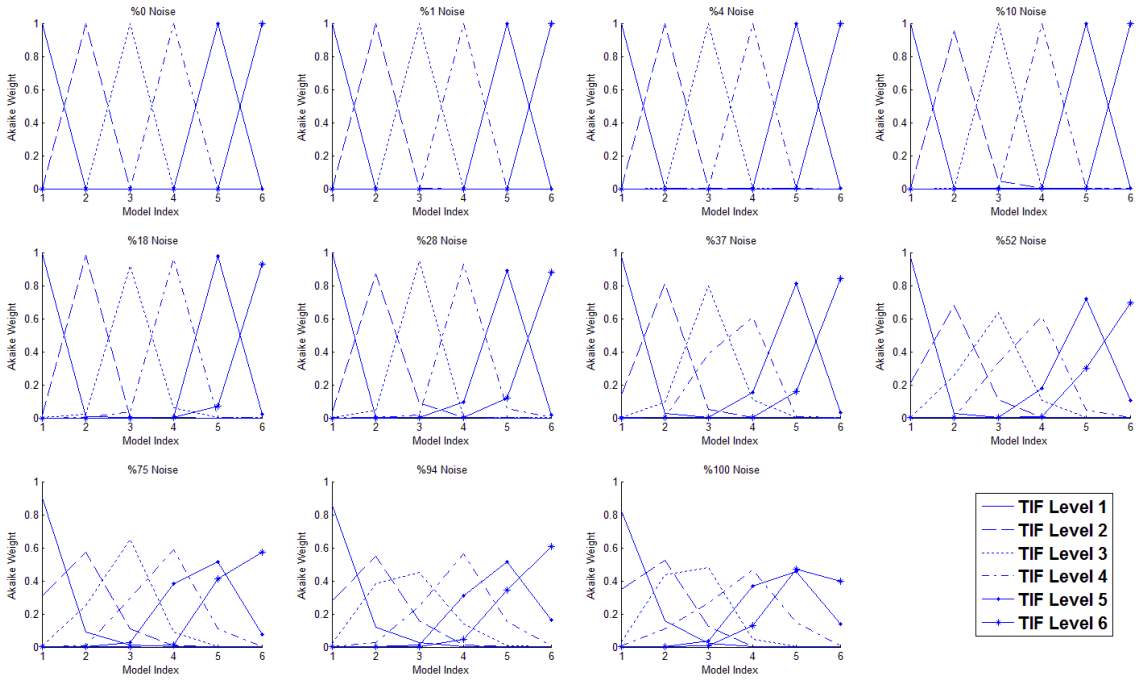

Figure 3.3. Akaike weights of each of the simulated signals after model averaging. The plots show the likelihood of each of the simulated TIF's being selected as the level of branching that they were simulated for. As seen here, even at the 18% noise level, the likelihood of picking the correct branching level of the TIF is almost 1 for all cases. As the noise level increases, the accuracy of the system decreases and the likelihood of picking the correct model gets less; however, in the 100% noise level, the likelihood of picking the correct level index does not go below 0.45.

Figure 3.4 shows a schematic diagram of our vascular model simulation. Here, the AIF is similar to the AIF used in the previous section and the TIFs from the second and sixth levels are found by convolving this AIF with the vascular transfer function at these two levels. The square represents a hypothetical voxel in which vessels from both the second and sixth levels pass through. The temporal signal sampled in this voxel is the weighted sum of the signals from the two vessel segments and depending on the effective volume of each of them in this voxel, the level of contribution of each signal will be adjusted. In our simulation, it is assumed that the weighted sum of only two signals from any two levels are present in the hypothetical voxel and the level of contribution of each of these two can vary from 0% to 100%, meaning that the signal is fully representing one level or the other or a combination of them. In addition, we added different levels of noise to the composite signal (0% to 100%) and explored the feasibility of our method to decompose these signals in presence of noise.

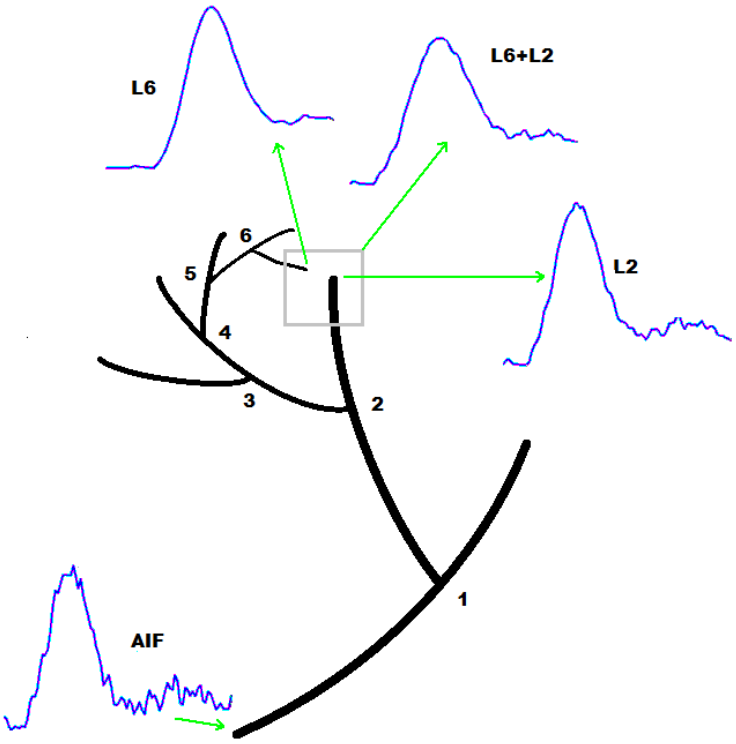

Figure 3.4. Schematic figure showing a typical AIF from the carotid artery of a human subject in DCE-CT images and the simulated TIFs at the second (L2) and sixth level (L6) of our vascular model. In this figure the effect of one voxel representing vessels from two different levels has been simulated. In this case the signal sampled from this voxel would be the superposition of the two signals (L6+L2). Using this configuration, we have studied the feasibility of our method to distinguish and separate the signals that form the composite signal.

Figure 3.5 shows the curves representing the Akaike weights of the composite signals after decomposition by the method explained above. Each curve represents the average of results from 300 repetitions at each noise level. The composite signal is basically the weighted sum of the two signals as described above each curve (the x-axis represents the percentage of contribution of the second signal in the composite signal based on their energy level). As seen here, in noise levels lower than 50%, all these curves meet at the 50% contribution point which matches our expectation: when the composite signal is the sum of two signals with equal levels of power, our method is able to decompose them into two signals with equal weights for each signal. One observation in these curves is that in the cases that there is no noise added to the signals or the noise level is small, the Akaike weights tend to get saturated to 1 or 0 for the individual signals, when the contribution is not close to 50%. This is due to the large difference in the residue values of the fitting procedure for the two signals in the absence of noise; when the

level of contribution of one signal to the composite signal changes from 0% to 100%, the residue increases in the order of 10, which is roughly what the difference between the residue of the fitting procedure for the two signals is when the contribution level of one is 0% and the other is 100%. This causes the AIC value to have a difference of approximately 250 between these two signals which leads to the Akaike weights calculated by Equation 20 have the values of 0 and 1 for these signals. As a rough rule of thumb, if the difference between the AIC_i or the AIC of model *i* and AIC_{min} is between 0 and 2 , the level of empirical support for model *i* is substantial and if it is between 4 and 7 it is considerably less and if it is larger than it is 10 essentially none [46].As the contribution of the second signal increases, the residue values for the two models get closer and fall in the same order; therefore the Akaike weights will have values between 0 and 1, as seen in the points of the curve close to the 50% point. When noise is added to the composite signal, even for the case of pure signals in the original composite signal, the residues will have large values and they will vary much less than what is seen in the no-noise situation and therefore the Akaike weights will not get saturated in these cases. It should also be noted that when the difference between the levels of the two signals increases, this saturation effect will become more evident, even in the presence of noise. The worst case is when one signal is from the 1^{st} layer and the second is from the 6^{th} layer, as seen in Figure 3.5. This is due to the large difference between the two residue values of these two signals after the fitting procedure. If a measure for the level of contribution of the signals is sought, using variations of the fitting residual values can be a better measure for that, instead of the Akaike weights.

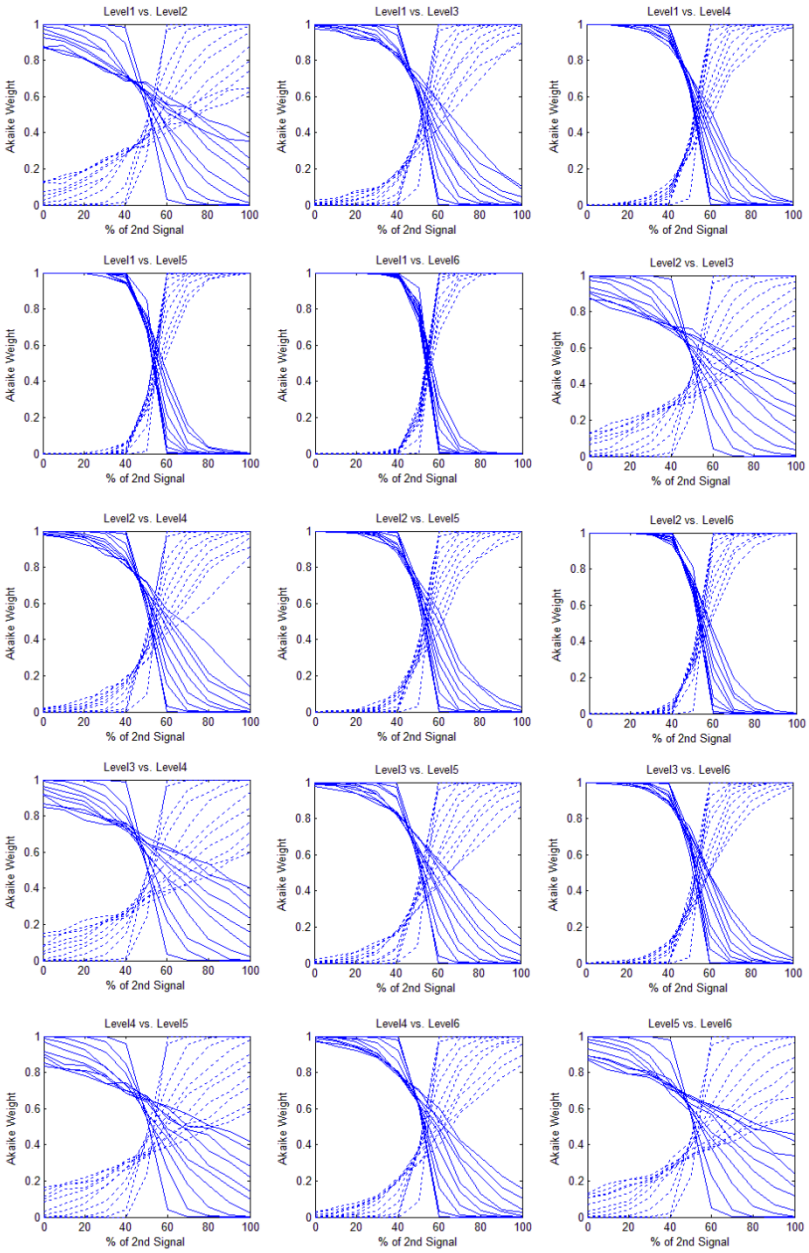

Figure 3.5. Akaike weights of the simulated composite signals after decomposition. Each curve represents the average of results of 300 repetitions at each noise level. The composite signal is basically the weighted sum of the two simulated signals (the x-axis represents the percentage of contribution of the second signal in the composite signal) from different layers of the vascular structure. In each of the boxes above, each plot represents one noise level: In the upper half of the box, from left to right, each dotted line indicates 0% to 100% noise level (0%, 1%, 4%, 10%, 18%, 28%, 37%, 52%, 75%, 94%, and 100%) added to the composite signal and the solid lines correspond to %100 to %0 noise levels respectively. In the absence of noise, the switching point for all of these cases occurs at the 50% level which is what is expected. However, in the case that the model levels are consecutive, when the noise level is increased, this switching point moves towards higher values, in favor of the model with fewer parameters. The worst case is seen in level 5 vs level 6 when the noise level is 100%. However, even in this case even up to 52% noise level, the cutoff threshold is still around 50%.

3.3 Modalities Considered for Testing the Model

For testing the model, several dynamic imaging modalities were considered that could have satisfied the requirements of our model; however for practical reasons not all of these were suitable for this part of our study. These modalities were as follows:

- DCE-T1 Images

- Dual Gradient Echo Images

- Fluorescein Angiography of the Fundus

- Dynamic CT images of the Brain

Below each of these modalities is described in more detail:

3.3.1 DCE-T1 Images

In DCE-T1 imaging, Spoiled Gradient-Recalled Echo (SPGRE) T1 weighted images are acquired repeatedly for a period lasting for a few minutes. The first few images are considered as the baseline and are recorded prior to injection of the CA. After intravenous injection of the CA, image acquisition will continue for a few minutes afterwards [50]. The contrast agents used in DCE-T1 imaging work by decreasing the spin-lattice relaxation time (or T1) in tissues that it is localized [51]. One of the most commonly used MR contrast agents is Gadolinium_Diethylene-Triamine-Pentaacetic-Acid (Gd-DTPA) that produces a marked reduction in proton relaxation rates. Gd-DTPA does not cross intact Blood-Brain-Barrier (BBB) and rapidly gets eliminated by glomerular filtration in the Kidneys [52]. It is assumed that the dose (or concentration) of Gd-DTPA is linearly related with the changes of the Spin Lattice Relaxation rate (Relaxitivity or 1/T1) which is expressed with the 1/seconds unit [51, 53]. However, nonlinearities in changes of relaxitivity (or in other words $\Delta R1$) due to limited access of water in tissue compartments distal to the CA can substantially bias estimates of tissue CA concentration. In addition to the non-linearity problem, in MR fast sequences, the T2* contrast competes with T1 contrast and can bias the estimate of T1 and consequently $\Delta R1$ [54]. Since our goal was to test our model in different parts of the brain and different levels of the vascular structure, these nonlinearities and

also the T2* effect would have caused unreliable results and therefore we decided not to use this modality for this part of our research.

Inversion recovery imaging techniques such as the Look-Locker (LL) pulse sequence can offer unbiased estimation of longitudinal relaxation time (T1) and the LL pulse sequence shows no evidence of bias in its estimates of tissue CA concentration [55]. However, LL imaging is a slow imaging technique due to the time required for full recovery of the longitudinal magnetization between sequential inversion pulses.

3.3.2 Dynamic Dual Gradient Echo Images

Spoiled Dual Gradient Echo (DGE) pulse sequence is a fast imaging technique with short echo time and relatively short time interval between image acquisitions (2 to 4 sec). The main advantage of DGE imaging is that it allows computation of T1 and T2* as pure components: this is essential for estimation of CA concentration ($\Delta R1$ and $\Delta R2^*$) for both permeability and perfusion studies. However, in practice the complex relationship between signal intensity, T1, T2*, and other model parameters such as M0 and flip angle, makes the dynamic estimation of $\Delta R1$ in the presence of noise levels typical of MRI, quite challenging [56]. We have developed novel methods for estimation of $\Delta R1$ and $\Delta R2^*$ signals in these images which will be described in detail in chapter IV. Despite the advantages of this image modality, the human images that we had acquired were too noisy and we decided not to use them for this section of our experiments.

3.3.3 Fluorescein Angiography of the Fundus

Fundus Fluorescein angiography (FFA) is an optical imaging method that is used for studying anatomic structures of the ocular fundus. The fundus is the interior surface of the eye and includes the retina, optic disk, macula and fovea and is the only part of the mammalian body where microcirculation can be directly observed [57]. Fluorescein Angiography records the dynamic interaction of fluorescein with both normal and abnormal anatomic structures of the ocular fundus. This procedure is performed by injecting fluorescein sodium dye as a bolus into a peripheral vein and recording the retina images using a fundus camera. The angiogram is created by imaging the fluorescence of the dye (520–530 nm, green–yellow light) after the retina is illuminated with a blue light at a wavelength of 465–490 [58].

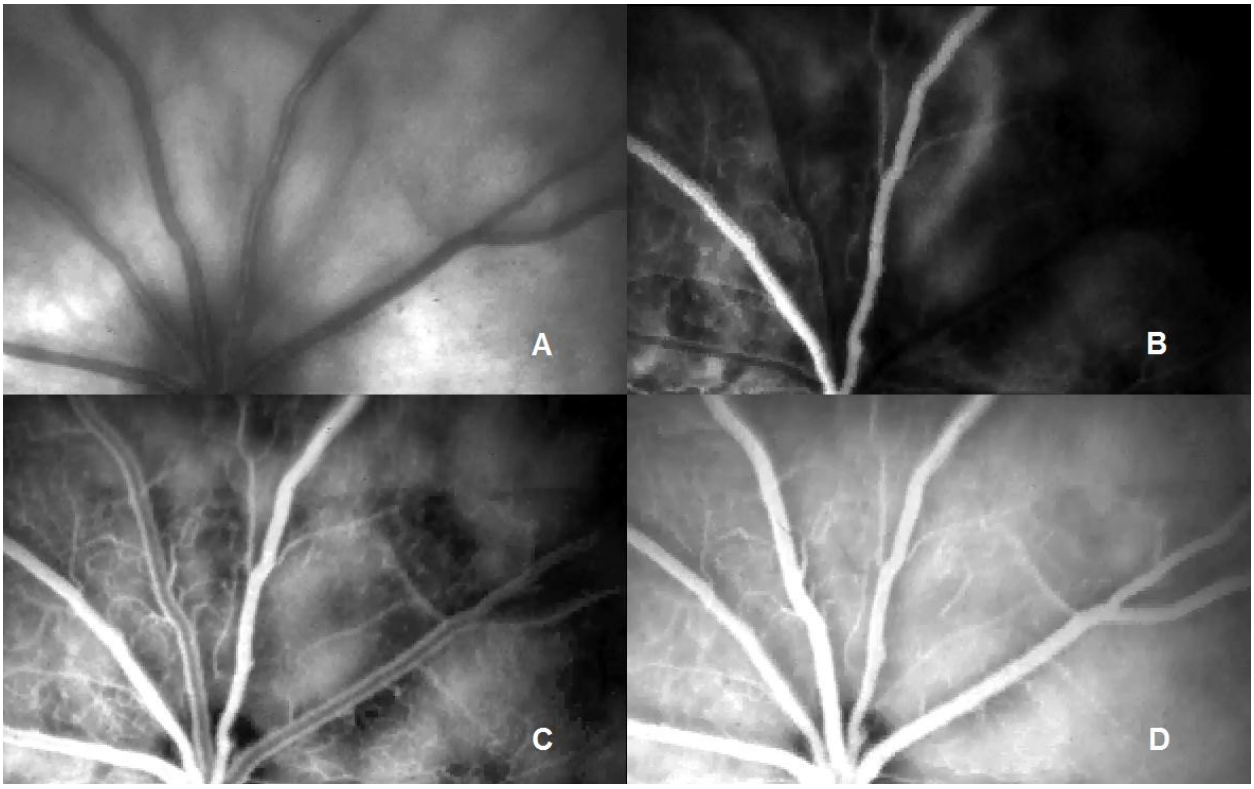

Figure 3.6. The four main stages of a fundus angiogram in the vessels of the Retina of a rat, seconds after injecting the fluorescein (A) shows the "Choroidal flush" stage where the fluorescein leaks into the extravascular space of the chorio-capillaries (B) The "Arterial phase" happens two seconds after the choroid is filled. As seen here the arteries start filling in this stage(C) In the "Arterio-venous phase", after the blood containing the CA passes through the capillaries, it gets collected by the veins; as seen here the effect of laminar flow can be seen as the layers of fluid closest to the vein walls get filled faster (D) Finally in the "Venous phase", filling of the veins gets completed.

Figure 3.6 shows FFA images from the retina of a rat that were acquired as part of a research study at Henry Ford Hospital to investigate the effects of Diabetes on microvasculature. The main goal in this experiment was measuring the circulation time of the CA from the arteries to the veins in normal and diabetic animals and based on that study the changes in the microvessels due to the disease. In this figure the four major stages of FFA can be seen. These are the Choroidal flush, Arterial Phase, Arterio-venous phase and the Venous phase. The profile of the contrast agent is measurable by sampling the pixel at different locations of the image. One advantage of this method is the high temporal resolution of the images (32.25 ms)

Even though this could have been an ideal modality for testing our model, we were not able to use these images due to problems including saturation of the CA signal after the filling of the major vessels and also excessive shifting of the images due to movement of the eye and not being able to co-register the images in a reasonable manner. Also, the number branching levels

and vascular physiology in the retina are not necessarily similar to those of the brain but we for testing our model, we could have adjusted the parameters to match the ocular vessels.

3.3.4 Dynamic CT Images of the Brain

Compared to DCE-MRI, DCE-CT images have lower Signal to Noise Ratio (SNR) and Contrast to Noise Ratio (CNR) [59] however, several other characteristics of this modality made it an attractive choice for our study: The signal intensity of the CT images is linearly dependent on the CA concentration [60] and also, the temporal resolution of this modality is much higher (~10 times more) than DCE-MR images (0.5 sec vs. 5 sec). In addition, CT images have a better spatial resolution [61]. All these characteristics made DCE-CT imaging an attractive candidate for our study.

3.4 Testing the Model with Dynamic Contrast Enhanced Computed Tomography (DCE-CT) Imaging

After studying different dynamic imaging modalities mentioned above, DCE-CT images were selected as the modality for testing our model. Below, the steps of processing these images for testing our model will be described.

3.4.1 CT Image Acquisition

DCE-CT images were acquired on a GE LightSpeed VCT scanner with image matrix size of 512×512 (24×24 cm FOV) and eight slices (5mm slice thickness) with 99 imagepacks (89 image sets sampled every 0.5 seconds for the first 44 seconds, one image acquired at the 50 second time point, followed by 9 image sets acquired every 16 seconds for a total scan time of 194 seconds). 50ml of iodinated CA with a concentration of 0.5ml/Kg was injected as a bolus using a power injector at a rate of 4cc/sec starting five seconds after start of image acquisition; cine scan was done for 50sec.

3.4.2 CT Image Preprocessing

The dynamic images were baseline corrected to make their intensity linearly dependent on the CA concentration. Also, to increase the SNR, especially in the tissue regions, the neighboring

voxels were averaged and the images were downsized to 128×128. After these pre-processing steps, the CT images were ready to be used for testing the model.

3.4.3 Results of Applying the Model to DCE-CT Images

For every subject, a small region on the circle of Willis was sampled and the temporal signals from the voxels in this region were averaged to represent the global AIF. This AIF was used as the reference for all the brain voxels for that subject.

The temporal DCE-CT data of every voxel was sampled and based on the method described in section 3.3.1, the six different transfer functions were convolved with the global AIF to find the best fit to the signal for each configuration. Using the fitting residues for every voxel, the Akaike weights were calculated. By assigning the Akaike weights of every voxel to the corresponding voxels in six image volumes, the probability maps of these six models are estimated. Figure 3.7 shows these six probability maps for two slices of a DCE-CT image volume. These show the probability of every voxel belonging to the each of the six models. As seen in this figure, in the probability map of the first model, the voxels that represent the major artery that the AIF has been sampled from have the highest Akaike weight which has a value very close to 1. As the model index increases, the voxels with the highest value shift from the major arteries to the veins. In the map corresponding to model 6, the voxels showing the major veins such as the sagittal sinus and the tumor have the highest likelihood of belonging to this model. These probability maps are used to create the blood flow delay maps of the brain.

One point that should be mentioned about the Akaike-weight maps in Figure 3.7 is the values in the normal tissue areas. Here, originally, the highest Akaike weight value of these voxels occurred mostly at model one (with a value of around 0.5) and the next two levels of maps had Akaike weights that were less than this value but were still considerable. Considering the hierarchy of the vascular structure, we didn't expect these voxels to have high Akaike weights for models with lower index. The reason was that after fitting the different levels of the models to the signals from these areas, models five and six had the best fit (had a lower residue after fitting) but not considerably better than the other models . One reason that the residue values of fitting are not dramatically different between different models in these areas is the low Contrast-to Noise ratio in normal tissue due to the small intravascular plasma volume fraction in normal

tissue which is less than 1%. Also the non-leaky property of intact vasculature in the brain contributes to this low contrast to noise ratio in these areas. Therefore these areas have a low CNR and the signal due to the CA is very noisy. After calculating the AIC values based on equation 3.5, since the number of parameters (k) for the first model was much lower than model six (2 parameters vs. 7 parameters), the estimated AIC values for voxels in this region got biased in favor of the lower models which is one of the characteristics of the AIC method. If the AIC gets calculated without the applying the penalizing terms (the number of parameters in the model for each level), the Akaike weight order for different models will follow the order of the fitting residue values for each level. One solution to this problem was to average the temporal signals of the neighboring voxels with low intensity prior to estimating their transfer function. This will reduce the noise and can result in a lower residue for the best fit model. We applied this solution to these images and got the results as seen in Figure 3.7. In this figure, the contribution of the higher level models to normal tissue can be seen after spatial averaging of the neighboring voxels.

Figures 3.8-a and 3.8-b show the delay (arrival time) maps of the same slices of the DCE-CT image set as in Figure 3.7. These delay maps are created after model averaging. What these delay maps show are basically the arrival time of the CA at different points of the image, with respect to the arrival time in the Circle of Willis, where the AIF has been sampled from. In the CT images, the major vessels (arteries and veins) can be seen with a higher contrast but in the delay map the arteries have a lower intensity since the delay time is shorter in them; however, the veins such as the inferior and superior sagittal sinuses show the highest delay time in these images and have values above 4 seconds which is a good approximation of the mean transit time of the blood flow in the brain [62]. Point **R** in this figure shows the reference point where the global AIF was sampled (similar to the AIF profile as in Figure 3.1). This AIF was used to estimate the transfer function between **R** and all the voxels in the image. As seen here, the estimated delay time is different at different parts of the brain: The arteries such as the main arteries marked as **A** have a short and the veins (such the Superior Sagittal Sinus marked as **B**) have a longer delay time.

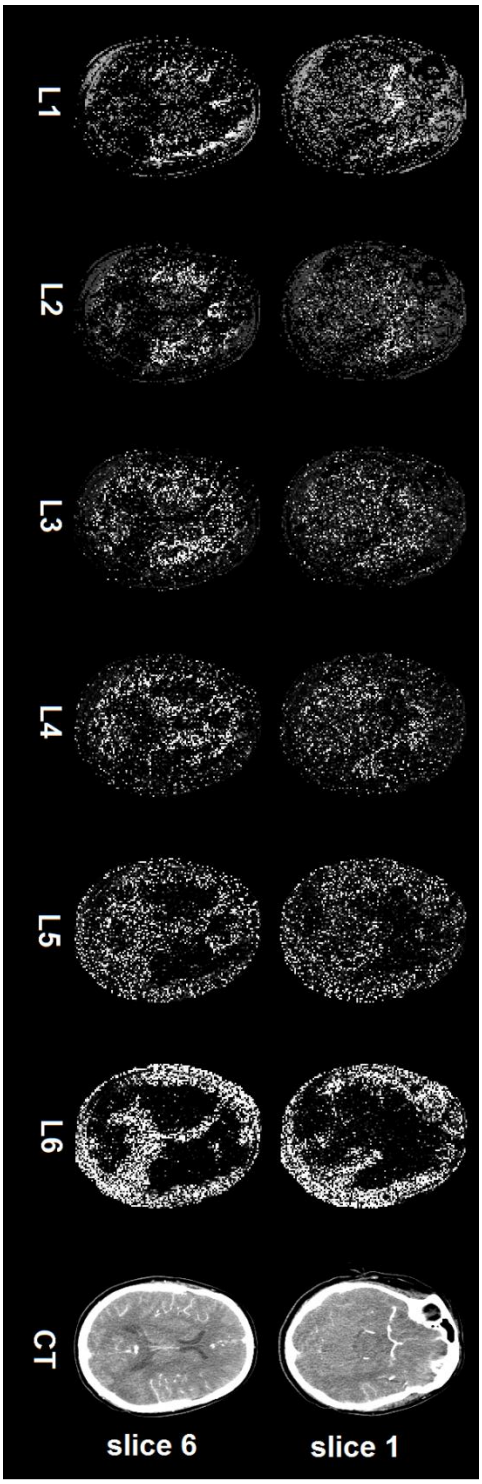

Figure 3.7 . Akaike weight (likelihood) maps of two slices of the CT image based on the six levels of the vascular tree model. The intensity of each voxel in the images L2 through L6 images show the likelihood of that voxel belonging to that level in the vascular tree. Based on the Akaike method, the sum of the intensities of every voxel across the six images is one. The images on the right column are the CT images of the same slice, a few seconds after injection of the contrast agent. As seen in these CT images, all the major vessels have been enhanced in intensity but there is no distinction between the arteries and veins since they are all enhanced.

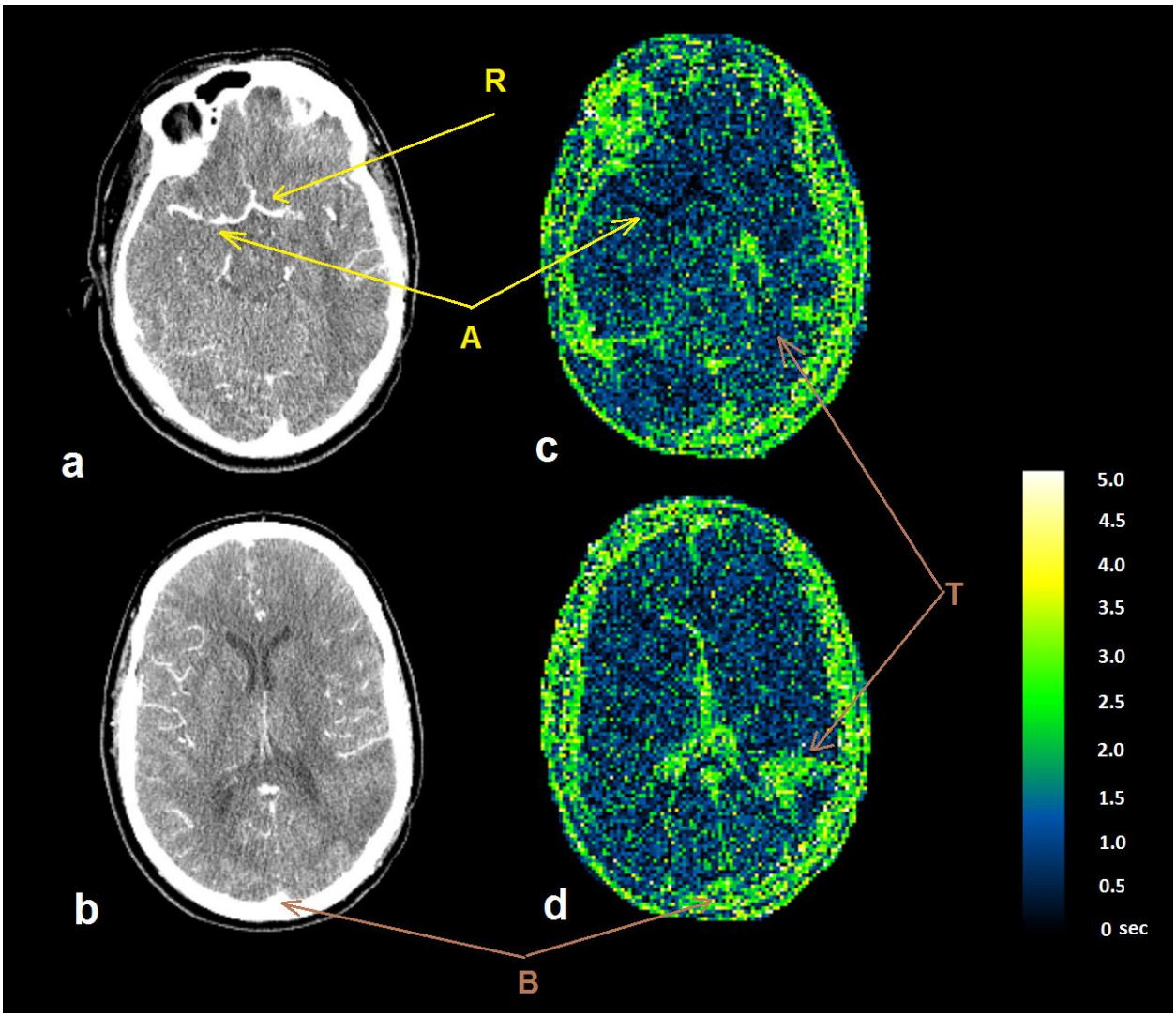

Figure 3.8. (a),(b) Two sections of post injection CT images and (c),(d) the delay (arrival time) maps (in seconds) created using the parameters found by our method. 'R' is the reference point for measuring the glocal AIF. 'A' is the location of one of the main arteries (short delay) and 'B' shows the Superior Sagittal Sinus (long delay). 'T' shows the location of the tumor.

One important note about this figure is the part of the image where a tumor can be seen (**T**). Based on the estimation using our method, the delay (arrival) time of the tumor in this image is long and comparable to the major veins such as the sagittal sinus. The artery or arteries that feed this tumor are not known to us at this point and we cannot make a statement about the level of their branching level (which could be from a higher level); however, the main reason for the system identifying this structure as having vessels from a high branching level is the abnormal CA profile sampled from this area in the CT images. Due to leakage of the CA from tumor vessels into the extravascular space, the CA profile does not follow the trend of the AIF sampled

from the major artery. Since the time required for the CA particles in the extravascular space to get cleared is usually longer than the imaging duration, the intensity of the voxels in these areas will stay high to the end of the scan. Therefore, the CA profile of these voxels mimics profile of a highly dispersed AIF. Although our method will still not be able to find a good fit to these profiles using the dispersed AIF found by model in its current form, it finds the best fit by assuming the TIF is from the 6^{th} level. In the following chapters, we will introduce an extended version of our vascular model where leakage of the contrast agent is also included in the model; there we will look more closely at the profile of the contrast agent and how to separate the intravascular and extravascular components of the tissue response signal in these areas.

3.4.4 Software Platform for Processing the CT Images

A software platform was designed and developed in MATLAB to perform the steps above and create the delay maps from the DCE CT images. Figure 3.9 shows the main interface of this software. Four dimensional DCE-CT images are read into the software in DICOM format and the user can go through different time points or slices of the image volumes using the scroll bars and can also adjust brightness or contrast of the images to find the best location for sampling the AIF from a major artery in the left window and have it plotted in the window on the right. Baseline correction is done after the CA profile is plotted and two baseline timepoints are selected using the scroll bars beneath the right side window. Reduction of the image size can be done before or after baseline correction. After baseline correction, the CT image intensity is assumed to be linearly dependent on the CA concentration. Figure 3.9 shows the CA profile of a small region on the circle of Willis after baseline correction is done.

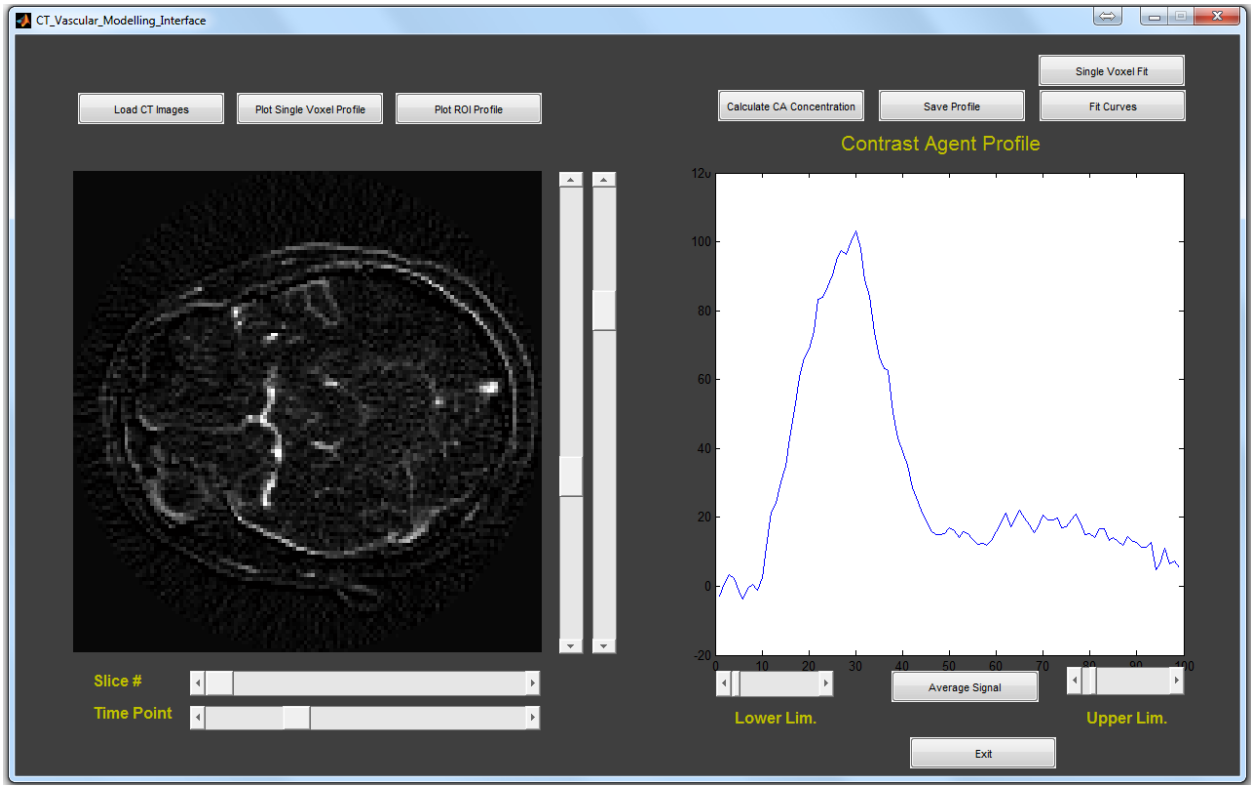

Figure 3.9. The main interface of the software platform for pre-processing and processing the CT images for estimating the level of the vascular tree in each of the voxels in the image. The image in the window on the left shows one slice of the baseline corrected CT image and the plot in the window on the right shows the CA profile sampled from a small region on the circle of Willis. As seen here, since this image is baseline corrected, the intensity of the image prior to injection of the CA is at the zero level which matches with our expectations.

CHAPTER IV

CALCULATION OF THE VASCULAR PERMEABILITY AND PERFUSION PARAMETERS

In this chapter, we will describe the theory, methods and a software tool that we have developed for estimation of the permeability parameters using Dynamic Contrast-Enhanced MR images and in the next chapter, will use these concepts for describing an extension of our vascular model which can describe the flow and vascular branching in vessels with leakage.

4.1 The Indicator-Dilution Method

The concept of Dynamic MRI started in the mid 1980's after injection of a contrast agent was proposed for measuring perfusion in tissues and permeability in vessels [40]. These measurements are based on the concepts of the Indicator-Dilution method introduced in the 1950's [12]. To use this method for Dynamic MRI, the concepts had to be translated to the MRI modality. In this section, after introducing the Pharmacokinetic model, we will explain the Observation equation for DCE MRI.

4.1.1 The Pharmacokinetic Model

Modeling leakage in the vascular system in integral form was first generated by Patlak [63, 64] and reiterated by Tofts et al. [65]. The first Model developed by Tofts was simply named Tofts Model or TM and was developed by generalizing existing models of tissue that assumed negligible amount of intravascular CA in them and was written as:

(4.1) $$C_t(t) = K^{trans} e^{-tK_b} * C_p(t)$$

where $C_p(t)$ and $C_t(t)$ are the plasma and tissue concentrations of the indicator, K^{trans} is the unidirectional transfer rate constant of the indicator from plasma across the vascular endothelium and blood-brain barrier into the interstitial fluid and k_b is the transfer rate constant from the interstitial compartment to the vascular compartment. Since the assumption of negligible concentrations of intravascular CA was invalid, later TM was generalized to the Extended Tofts Model (ETM) as we use it today [33]. Based on the Extended Tofts Model, after intravascular administration of CA, its concentration in tissue is given by:

(4.2) $$C_t(t) = K^{trans} \int_0^t e^{-k_b(t-\tau)} C_p(\tau) d\tau + v_P C_p(t)$$

Here, v_p is the fractional volume of the vascular distribution space, usually thought to be the plasma distribution space.

If the transvascular transfer of the CA is passive (non-active transfer), the two rate constants are related via the interstitial volume fraction:

(4.3) $$v_e = \frac{K^{trans}}{k_b}$$

It should be noted that in the computation of the permeability parameters, v_e is a *derived* factor; k_b is the parameter that can be directly estimated from the concentration-time curve. In section 4.4, the details of our method for finding the permeability parameters using this model will be discussed.

4.1.2 The Observation Equation

It has been shown that the changes in Gadolinium (Gd) concentration and the longitudinal relaxation rate (= $1/T_1$) are related through the following equation [51, 53]:

(4.4) $$R_1(t) = R_{10} + r_1 C_t(t)$$

where R_1 is the longitudinal relaxation rate (= $1/T_1$), R_{10} is the rate before injection of Gd and r_1 is proton relaxivity i.e. the increase in relaxation rate per unit concentration of Gd (its in-vitro

value is 4.5 s-1mM-1). As seen here, the change in Relaxivity is linear with CA concentration. If the relaxation rate is subtracted from the pre-injection relaxation rate, the difference would be a parameter which is linearly dependent on $C_t(t)$, the contrast agent concentration. We will name this ΔR_1. Based on this definition, the following equation relates the MR parameters to the pharmacokinetic model:

$$(1 - Hct)\Delta R_{1t}(t) = K^{trans} \int_0^t e^{-k_b(t-\tau)} \Delta R_{1a}(\tau) d\tau + v_p \Delta R_{1a}(t) \tag{4.5}$$

This is named the Observation Equation. Here, *Hct* is the Hematocrit ratio, R_{1a} has been defined as the longitudinal relaxation rate in the artery, and R_{1t} as the longitudinal relaxation rate in the tissue, and Δ denotes the subtraction of the pre-contrast and post-contrast values of the longitudinal relaxation rate.

4.2 Calculation of the Longitudinal Relaxation Rate Change (ΔR1)

Based on the Observation Equation, to find the permeability parameters of brain vasculature using the Pharmacokinetic Model and MR images, it is necessary to calculate ΔR_1 first. We have used two MR sequences for permeability studies: Spoiled Gradient-Recalled Echo (SPGRE) DCE-T1 and Dual Spoiled Gradient Echo (DGE). In the next two sections, we will describe each sequence and explain the procedures that we have developed for calculating ΔR_1 for these two sequences.

4.2.1 Calculation of ΔR1 in DCE T1 Images

In an SPGRE DCE-T1 sequence, the signal intensity of any voxel can be written as follows [66, 67]:

$$S_n(t) = \frac{M_0 \sin(\theta) e^{-TE\, R_2^*(t)} (1 - e^{-TR\, R_1(t)})}{1 - \cos(\theta) e^{-TR\, R_1(t)}} \tag{4.6}$$

Here, *n* is the index of the image in the DCE-T1 procedure, *t* is time, M_0 the magnetization of protons in the voxel, θ the local tip-angle, *TR* the repetition time between the pulses, *TE* the echo time and $R_2^*(t)$ the transverse relaxation rate. Using this equation, we proceed to find ΔR_1; the following calculations are done in a voxel-by-voxel basis.

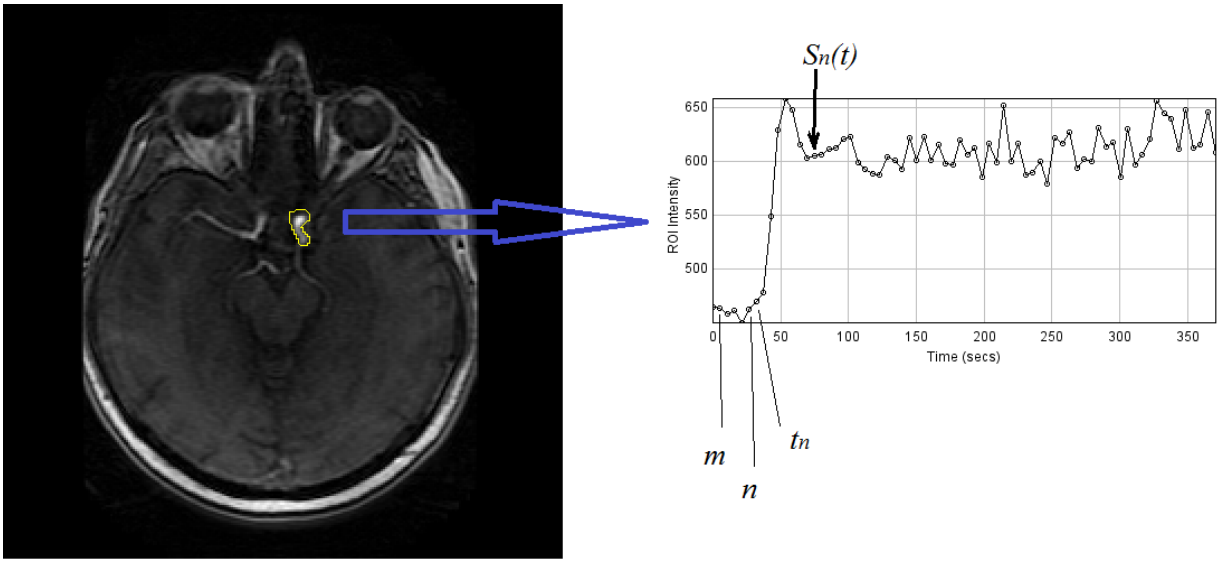

Figure 4.1. The profile of the CA sampled from the Left ICA in an SPGRE DCE T1 image series. The figure shows the timepoints *m* and *n* where the preinjection signal is averaged from, for finding μ_{pre} for this signal. t_n is the last time point before arrival of the CA to this point in the vascular structure. This image series consists of 70 timepoints with a resolution of 5.376 seconds.

The typical time course of a DCE-T1 signal sampled from the ICA can be seen in figure 4.1. As seen here, the pre-injection and post injection phase of the signal can be clearly identified by the sharp rise at the arrival time of the CA. We name the last time point before arrival of the contrast agent t_n. To define the mean of the signal before arrival of the contrast agent (μ_{pre}), two points are defined as *m* and *n* where $m<n<t_n$:

(4.7) $$\mu_{pre} = \frac{\sum_{t=m}^{n} S_t}{n-m+1}$$

Now we define a new parameter, α_t, as the ratio of the baseline to post-injection signal intensity at any time *t*, where $t>t_n$:

(4.8) $$\alpha_t = \frac{\mu_{pre}}{S_t}$$

We can rewrite equation 4.6 with the pre-injection T1 and T2* values as follows:

(4.9) $$S_0 = \frac{M_0 \sin(\theta) e^{-TE\, R_2^*(t \leq t_n)} (1 - e^{-TR\, R_1(t \leq t_n)})}{1 - \cos(\theta) e^{-TR\, R_1(t \leq t_n)}}$$

Assuming that the errors in MRI tissue are approximately normally distributed μ_{pre} will be an unbiased estimator of S_0:

(4.10) $$S_0 \approx \mu_{pre}$$

Also, assuming that TE << T2*, α_t in Equation 4.8 can be written as:

(4.11) $$\alpha_t = \frac{(1-e^{-TR\,R_1(t\leq t_n)})(1-\cos(\theta)e^{-TR\,R_1(t>t_n)})}{(1-e^{-TR\,R_1(t>t_n)})(1-\cos(\theta)e^{-TR\,R_1(t\leq t_n)})}$$

We define the following parameters:

(4.12) $$E^0 = e^{-TR\,R_1(t\leq t_n)}$$

(4.13) $$E^t = e^{-TR\,R_1(t>t_n)}$$

(4.14) $$E_t^{\Delta} = \frac{E^t}{E^0} = e^{-TR[R_1(t>t_n)-R_1(t\leq t_n)]}$$

Based on these new parameters, Equation 4.11 can be re-written as:

(4.15) $$\alpha_t = \frac{(1-E^0)(1-\cos(\theta)E_t^{\Delta}E^0)}{(1-E_t^{\Delta}E^0)(1-\cos(\theta)E^0)}$$

Solving for E_t^{Δ}:

(4.16) $$E_t^{\Delta} = \frac{(1-E^0)-\alpha_t(1-\cos(\theta)E^0)}{(E^0)^2\cos(\theta)(\alpha_t-1)+E^0\cos(\theta)-\alpha_t E^0}$$

Therefore, the analytical equation for the change in $R_1(t>n)$ can be written as:

(4.17) $$\Delta R_1(t>n) = -\frac{1}{TR}\ln(E_t^{\Delta})$$

There have been other analytical estimates of R1 versus time after the injection of a CA such as the approach suggested by Li et al. [68] . However, the method suggested in that paper requires a priori knowledge of the relaxivity of CA in a particular tissue and also a measure of proton density (M_0) must also be presented. It has been demonstrated [69] , that the apparent tissue relaxivity of a CA is dependent on the rate of transvascular water exchange, among other factors.

This exchange rate probably does change in pathology. The advantage of our analysis is that it does not require an assumption about the tissue relaxivity, or a calculation of M_0, and may avoid systematic errors associated with an assumption as to the relaxivity of the CA in a particular tissue. The sensitivity of Equation 4.16 to a priori knowledge of the tip-angle (θ) should be also noted.

4.2.2 Calculation of ΔR1 in Dual Gradient Echo Images

As we mentioned in section 3.3.2, DGE imaging allows computation of T1 and T2* as pure components: this is essential for estimation of CA concentration (ΔR1 and ΔR2*). The ability to estimate pure components is an advantage to the SPGRE DCE-T1 images where nonlinearities in the MR measurement of ΔR1 due to limited access of water in tissue compartments distal to the CA and also the T2* contrast competing with T1 contrast can substantially bias estimates of tissue CA concentration. Another advantage of the DGE sequence is the relatively short time interval between image acquisitions (2 to 4 sec). Below we will describe the method we have developed for calculating the ΔR1 signal from the DGE signals.

The following equations describe the measured T1-Weighted intensities of the first and second echo signals and their relationship with the longitudinal and transverse relaxation times (T1, $T2^*$), repetition time (TR), echo time (TE), the flip angle (θ), and the equilibrium longitudinal magnetization (M0). *F* denotes the signal from the First echo and S the signal from the Second echo:

(4.18) $$F = \frac{M_0 \sin\theta\left(1-e^{\frac{-TR}{T1}}\right)e^{\frac{-TE1}{T_2^*}}}{1-\cos\theta e^{\frac{-TR}{T1}}}$$

(4.19) $$S = \frac{M_0 \sin\theta\left(1-e^{\frac{-TR}{T1}}\right)e^{\frac{-\mu TE2}{T_2^*}}}{1-\cos\theta e^{\frac{-TR}{T1}}}$$

(4.20) $$\mu = \frac{TE2}{TE1}$$

For each voxel there are two main phases for the signal: the pre-injection phase and the post injection phase. In order to set a baseline for the signal intensity prior to injection of the contrast

agent for each voxel, we average the signals S_t and F_t for that voxel over few time points prior to injection:

(4.21) $$F^{pre} = \frac{1}{(n-m+1)} \sum_{t=m}^{n} F_t$$

(4.22) $$S^{pre} = \frac{1}{(n-m+1)} \sum_{t=m}^{n} S_t$$

In this equation, *t* denotes the experiment time point and F^{pre} and S^{pre} are the mean of the signal intensities associated with first and second echoes between time points *m* and *n* where *m* and *n* are smaller than the injection time. Also we define E^{pre} and E^{post} as:

(4.23) $$E^{pre} = e^{\frac{-TR}{T1(pre)}}, E^{post} = e^{\frac{-TR}{T1(post)}}$$

Which are the values estimated using the images obtained from the T1 mapping sequences that are run before and after the DGE sequence. Using the definitions above, we have derived the following equations for preprocessing the DGE signals for Dynamic Contrast Enhanced Imaging:

(4.24) $$\theta_{Est} = \cos^{-1}\left\{ \frac{1 - \left[\frac{\left(\sum_{t=m}^{n} S_t^{pre}\right)^{\frac{1}{\mu-1}}}{\left(\sum_{t=m}^{n} F_t^{pre}\right)^{\frac{\mu}{\mu-1}}}\right]\left[\frac{\left(\sum_{t=m}^{n} F_t^{sat}\right)^{\frac{\mu}{\mu-1}}}{\left(\sum_{t=m}^{n} S_t^{sat}\right)^{\frac{1}{\mu-1}}}\right]}{E^{post} - E^{pre}\left[\frac{\left(\sum_{t=m}^{n} S_t^{pre}\right)^{\frac{1}{\mu-1}}}{\left(\sum_{t=m}^{n} F_t^{pre}\right)^{\frac{\mu}{\mu-1}}}\right]\left[\frac{\left(\sum_{t=m}^{n} F_t^{sat}\right)^{\frac{\mu}{\mu-1}}}{\left(\sum_{t=m}^{n} S_t^{sat}\right)^{\frac{1}{\mu-1}}}\right]} \right\}$$

(4.25)

$$\Delta R_1(t) = \frac{-1}{TR} \ln\left\{ \frac{1}{\cos\theta_{Est} E^{pre}} + (n-m+1)\left[1 - \frac{1}{\cos\theta_{Est} E^{pre}}\right]\left\{\frac{\left[\sum_{t=m}^{n} S_t^{pre}\right]^{\frac{1}{\mu-1}}}{\left[\sum_{t=m}^{n} F_t^{pre}\right]^{\frac{\mu}{\mu-1}}}\right\}\left\{\frac{\left[F_t\right]^{\frac{\mu}{\mu-1}}}{\left[S_t\right]^{\frac{1}{\mu-1}}}\right\}\right\}$$

As seen in these equations, we can get both an estimate for the pure component $\Delta R_1(t)$ and also the actual tip angle for the signal in each voxel. One interesting observation about this equation is that $\Delta R_1(t)$ is independent on the value of E^{post}.

Using this equation, and using the pre and post T1 values, $\Delta R_1(t)$ can be directly estimated. In our study, we used these equations, to train an adaptive neural network for estimating ΔR_1 maps in images of six Fisher rats with brain tumors [56]. The ANN was trained and tested with the DGE and LL information using a K-Fold Cross-Validation (KFCV) method with 60 folds and 10500 samples. The Area Under the Receiver Operator Characteristic Curve (AUROC) for 60 folds was used for training, testing and optimization of the ANN. After training and optimization, the optimal ANN (4:7:5:1) produced maps of CA concentration which were highly correlated (r =0.89, P < 0.0001) with the CA concentration estimated by the LL technique which are considered to be the gold standard for estimating the T1 value. The estimation made by the ANN had an excellent overall performance (AUROC = 0.870).

4.2.3 Using Signal Intensity Instead of ΔR_1

As we mentioned in the previous sections, the standard approach for solving the DCE pharmacokinetic model is creating an observation equation. It is generally assumed fact that the measured signal intensity (SI) time course data (*St*) be converted to an indicator concentration time course. The standard approach utilizes the longitudinal relaxation rate change (ΔR_1) to construct the concentration-time curve of the CA [70, 71]. This process depends on the accurate estimation of pre injection longitudinal relaxation times (*T1*) and signal intensity (S_0) prior to administration of CA. Despite these approaches, there have been recent studies that have proposed to use normalized SI, $(\frac{S_t - S_0}{S_0})$, instead of *ΔR1* in DCE MRI permeability analyses [70, 72]. However, we know of no assessment of the agreement in the estimated permeability parameters using different measures of CA concentration (SI, (ΔR1)). Considering the fact that we use DCE-MR images in our study, it is of critical importance to address this issue before employing these images in any of our studies that involved testing our vascular models. Therefore we did two studies to evaluate the effect of using SI instead of ΔR1; In the first study we approached the problem in an analytical manner and using Equation 4.16, simulated the two signals and investigated the rate of change of ΔR1 value based on changes in normalized SI at different resting T1 values [73]. In the second study, we calculated the tumor permeability parameters using 3D Spoiled-Gradient-Echo (SPGRE) brain images of ten treatment-naive

patients with Glioblastoma Multiforme (GBM) using both SI and ΔR1 [74]. In chapter VI, the results of these studies will be presented.

4.3 Estimation of T1 maps

As explained in sections 4.2.1 and 4.2.2, calculation of ΔR1 requires knowledge of the T1 values of the tissue, prior to injection of the contrast agent [75]. Therefore one of the routine sequences in DCE MRI is the acquiring the Pre-Injection T1 map prior to acquiring the dynamic images. In this section, we will discuss the conventional methods for estimating these T1 maps and next, will introduce a novel method that we have developed for this purpose.

4.3.1 T1 Map Estimation Using Conventional Methods

Two of the most common methods for creating T1 maps are the Look-Locker (LL) [76, 77] and Driven Equilibrium Single Pulse Observation of T1 (DESPOT1) [78, 79] methods. LL is an inversion recovery method and DESPOT1 derives T1 from two or more spoiled gradient recalled echo (SPGRE) images acquired with a constant TR and different flip angles [75].

Assuming that TE << T2* The SPGRE signal intensity can be written as [75]:

(4.26) $$S_i = \frac{M_0\left(1-\exp(-\frac{TR}{T_1})\right)\sin(\alpha_i)}{1-\exp(-\frac{TR}{T_1})\cos(\alpha_i)}$$

where M_0 is the equilibrium longitudinal magnetization and α_i is the flip angle and i is the index of the flip angle. The goal is to estimate M_0 and $T1$ using different fitting methods. Several methods have been proposed for this purpose such as Linear Least Squares (LLS), Gupta's Linear Least Squares (GLLS)) [80], Nonlinear Least Squares (NLS) [81] and Weighted Linear Least Squares (WLLS) [81].

As an example, the LLS approach estimates M_0 and $T1$ by minimizing the following objective function [75]:

(4.27) $$\chi^2_{NLS}(M_0, T_1) = \sum_{i=1}^{n} \frac{1}{\sigma_i^2}\left(S_i - M_0\sin(\alpha_i)\frac{1-exp\left(-\frac{TR}{T_1}\right)}{1-exp\left(-\frac{TR}{T_1}\right)\cos(\alpha_i)}\right)$$

Where σ_i is the expected signal standard deviation due to noise and *n* is the number of flip angles in the experiment. In the Linear methods, the equation is rearranged to form a linear equation and then, linear fitting methods will be applied to them for finding the values of M_0, T_1 for each voxel. Estimation of T_1 from the nonlinear SPGRE equation is susceptible to the signal acquisition noise level and also to the combination of the flip angles selected for the experiment. The problem with these linear methods is that they are not accurate in estimating T1, especially in regions with high T1, such as CSF. Overall GLLS and WLLS overestimate while ILLS underestimates [75]. Due to the inaccuracy of these methods, we decided to design a model trained adaptive system for estimating the T1 map based on the DESPOT1 method. The details are explained in the next section.

4.3.2 T1 Map Estimation Using an Artificial Neural Network

In this part of the study, the goal was to train an adaptive neural network (ANN) for estimation of T1 [76] to get better estimates compared to the conventional methods as explained in the previous section.

In this study, two clinically approved SPGRE protocols with two sets of flip angles - [2 º, 5 º, 10 º, 15 º, 20 º, and 25º] for the first study, and [3 º, 6 º, 9 º, 15 º, 24 º, and 35º] for the second study (*N*=1 to 6 for both sets) were used to model:

(1) The signal acquired in the SPGRE MR experiments and

(2) a synthetic data set provided by QIBA (Quantitative Imaging Biomarkers Alliance) respectively.

For defining the SPGRE signal, we used the following equation:

(4.28) $$S_i = \frac{M_0\left(1-e^{-\frac{TR}{T1}}\right)e^{\frac{TE}{T_2^*}}\sin(\alpha_i)}{1-e^{-\frac{TR}{T1}}\cos(\alpha_i)}$$

For training the ANN, a gain insensitive input set ($\mu_{k-1} = \frac{S(\alpha_k)}{S(\alpha_1)}$: k=2, 3… 6) was described as follows:

(4.29) $$\mu_{k-1} = \frac{(1-e^{-\frac{TR}{T1}}\cos(\alpha_1))\sin a_k}{(1-e^{-\frac{TR}{T1}}\cos(\alpha_k))\sin \alpha_1} \qquad \text{where k= 2, 3… 6}$$

These normalized signals were input to an ANN with a feed-forward multilayer perceptron (MLP) architecture with back propagation training algorithm. Using equation 4.27 and 4.28, for every T_1 value ranging from 10ms to 5000ms (with 10ms intervals), SPGRE signals were simulated by varying the other independent parameters (T_2* and M_0). Different levels of Gaussian noise were also added to the simulated signals to construct a set of signals with different SNR ranging from 2 to 30 (14 different SNR levels) and 10 to 20 (5 different SNR levels: 5, 10, 15, 25 and 30) for test and training sets respectively. The normalized simulated signals (Equation 4.28) were then input to the ANN, with their T_1 value as the gold standard of training. In simulations, for each SNR, the T_2* and M_0 in equation 4.27 were varied (as free and independent parameters) over the range of 5-500ms with 10ms intervals for T_2* and 10^5 - 10^6 with 10^3 intervals for M_0 to generate different SPGRE signals for testing the ANN performance compared to other techniques. While all the simulated signals were used as a testing set, a subset of the simulated signals (*n*=2500) corresponding to only 5 different levels of SNRs (5, 10, 15, 25, and 30) were used for the training set.

To test our method, we used different data sets. One was an in house synthetic T1 map that we created as seen in Figure 4.2-A, which represents three different anatomical areas (WM, GM, and CSF). As shown in this figure, three different Gaussian distributions of T_1 have been generated and assigned to the anatomical areas (WM, GM, and CSF) of the map using the mean and standard deviation of T_1 values reported for these areas in the literature [82] Figure 4.2-B illustrates a set of SPGRE images corresponding to a set of flip angles (2, 5, 10, 15, 20, and 25) constructed from the synthetic T_1 map using equation 4.27.

Also to evaluate the accuracy of the model-trained ANN against different methods, experimental results produced by the model trained ANN for different areas of the brain (WM, GM, and CSF) in six patients (30 central slices) were averaged and compared to the results of the other methods (NLS, WLLS, GLLS) as well as the T_1 values reported in the literature.

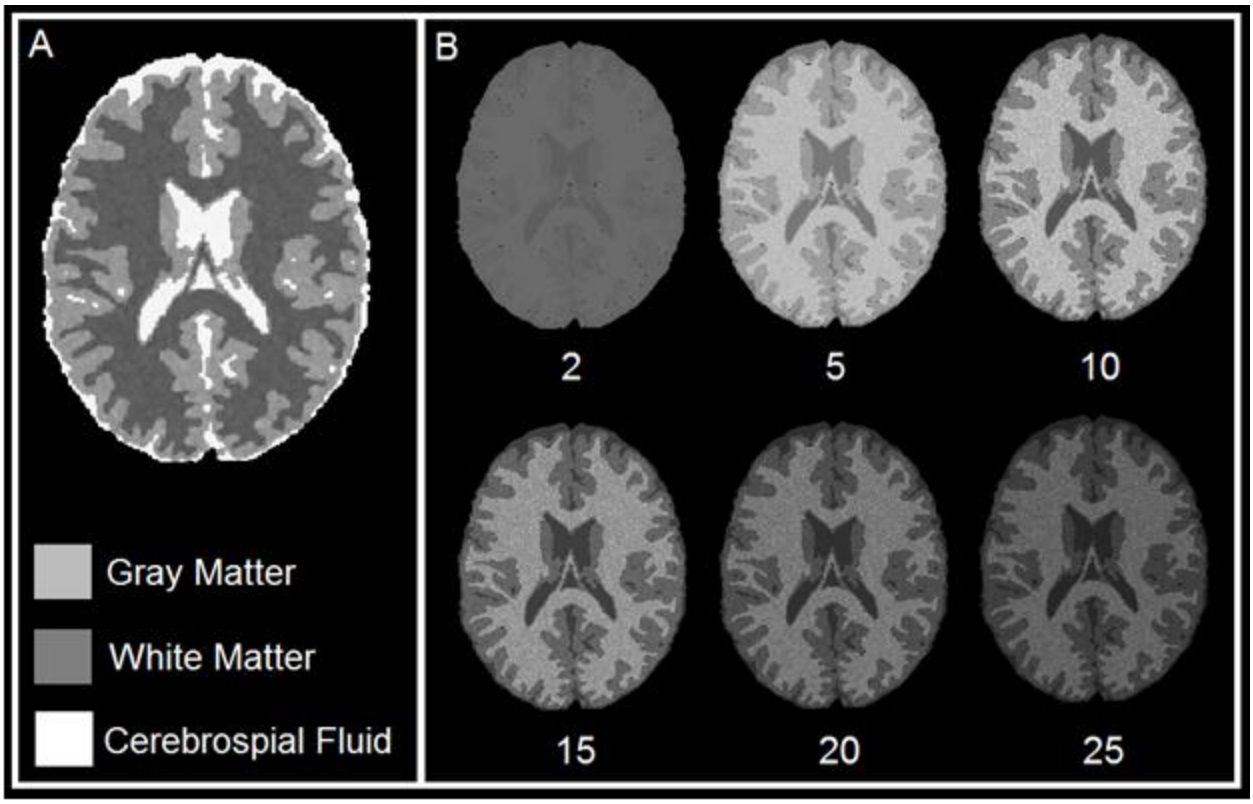

Figure 4.2 Figure A represents the in-house synthetic T_1 map constructed from three different anatomical areas (WM, GM, and CSF) filled with Gaussian distribution of T_1 values using mean and standard deviation of T_1 values reported in the literature. Figure B illustrates a set of SPGRE images corresponding to a set of flip angles (2, 5, 10, 15, 20, and 25) constructed from the synthetic T_1 map using equation 1.

Table 4.1 shows the estimates of T1 values obtained with different methods and on human (in blue) and synthetic data (in red). The second row of this table shows the mean and standard deviation of T_1 values simulated for different anatomical areas (WM, GM, CSF) of the brain using Gaussian distributions constructed according to the mean and standard deviation of T_1 values reported in the literature. According to this table, mean and standard deviation of the T_1 values in different anatomical areas estimated by the model-trained ANN, NLS, GLS, and WLLS are strongly in agreement with the simulated values of T_1 (see the 2^{nd} row of the table). This study also confirms that compared to the other methods (NLS, GLLS, and WNLS), the ANN is able to estimate the T1 value with a lower average error, for a wide range of SNRs in different anatomical areas of the brain [76].

Table 4.1. The mean and standard deviation of the T1 values for voxels falling in the White Matter (WM), Gray Matter (GM) and Cerebrospinal fluid (CSF) of the synthetic in-house and human data estimated using different techniques. The second row represents the gold standard values of T1 simulated in the synthetic data and the red values show the T1 values estimated using different methods. The T1 values estimated by the model-trained ANN match the values of the synthetic data better. Also, the T1 values found in human subjects (blue values) are more in agreement with the literature compared to the T1 values estimated by the other methods.

Method	White Matter	Gray Matter	CSF
In-house Synthetic Data	831 ± 93 ms	1331 ± 129 ms	3380 ± 342.ms
Model-Trained ANN	831 ± 94 ms	1335 ± 129 ms	3378 ± 341ms
NLS	826 ± 95 ms	1324 ± 129 ms	3376 ± 343 ms
GLLS	826 ± 95 ms	1324 ± 129 ms	3369 ± 347 ms
WLLS	826 ± 96 ms	1324 ± 129 ms	3374 ± 342 ms
ANN - Patient	1011 ± 138 ms	1249 ± 291 ms	3162 ± 631 ms
NLS - Patient	1097 ± 148 ms	1277 ± 327 ms	4325 ± 698ms
GLLS - Patient	1118 ± 159 ms	1334 ± 368 ms	3410 ± 870 ms
WNLS - Patient	1107 ± 156 ms	1162 ± 341 ms	3323 ± 710 ms

4.4 Estimation of Permeability Parameters Using the Pharmacokinetic Model

In sections 4.1 through 4.3, we introduced the pharmacokinetic model and our methods for estimating the longitudinal relaxation rate change (ΔR_1) and the (pre-injection) baseline T1 map. These are two of the necessary components for finding the permeability. In this section, we will first discuss the concept of fitting the CA profiles to the Pharmacokinetic model for different conditions of the vessels and next, explain our method of model selection for finding the best fitting model for each voxel.

4.4.1 Models of Vascular Leakiness

In section 4.1.1, we introduced the pharmacokinetic model in the form of the Extended Tofts Model (Equation 4.2) and described the parameters in this model (K^{trans}, k_b, v_p and v_e). When dealing with vascular permeability, three conditions can be considered for the vessels which lead to three nested models [66, 83]:

(1) Impermeable vasculature where the Blood Brain Barrier is intact.

(2) Moderate influx which is observed as leakage without efflux.

(3) Fast leakage which leads to bidirectional exchange.

We have also defined fourth model which we refer to as model 0 [66]. This model represents voxels or areas in the image where there is no evidence of vascular filling with the CA. In Figure 4.3 a schematic diagram of these four models can be seen and the leakage is explained as a two compartmental model: The Vascular Compartment (VC) and the Extracellular-Extravascular compartment. In Model 0 there is no evidence of vascular filling so there is no exchange of the CA between the two compartments ($K^{trans} = 0$, $k_b = 0$, $v_p = 0$). In Model 1 there is evidence of vascular filling but no leakage to the EEC ($K^{trans} = 0$, $k_b = 0$, $v_p \neq 0$). Model 2 indicates leakage from VC into the EEC but without reabsorption ($K^{trans} \neq 0$, $k_b = 0$, $v_p \neq 0$). Finally, Model 3 shows the case where not only leakage occurs from VC to EEC, but the CA that has leaked into the EEC will get reabsorbed into the VC ($K^{trans} \neq 0$, $k_b \neq 0$, $v_p \neq 0$) [84].

Based the conditions for the permeability parameters for each of these models, the Tofts model can be written as follows (since the application is for MR images, we will write the observation equation here):

Model 0:

(4.30) $$\Delta R_{1t}(t) = 0$$

Model 1:

(4.31) $$\Delta R_{1t}(t) = \frac{1}{(1-Hct)} \left\{ v_p \Delta R_{1a}(t) \right\}$$

Model 2:

(4.32) $$\Delta R_{1t}(t) = \frac{1}{(1-Hct)} \left\{ v_p \Delta R_{1a}(t) + K^{trans} \int_0^t \Delta R_{1a}(\tau) d\tau \right\}$$

Model 3:

(4.33) $$\Delta R_{1t}(t) = \frac{1}{(1-Hct)} \left\{ v_p \Delta R_{1a}(t) + K^{trans} \int_0^t e^{-K_b(t-\tau)} \Delta R_{1a}(\tau) d\tau \right\}$$

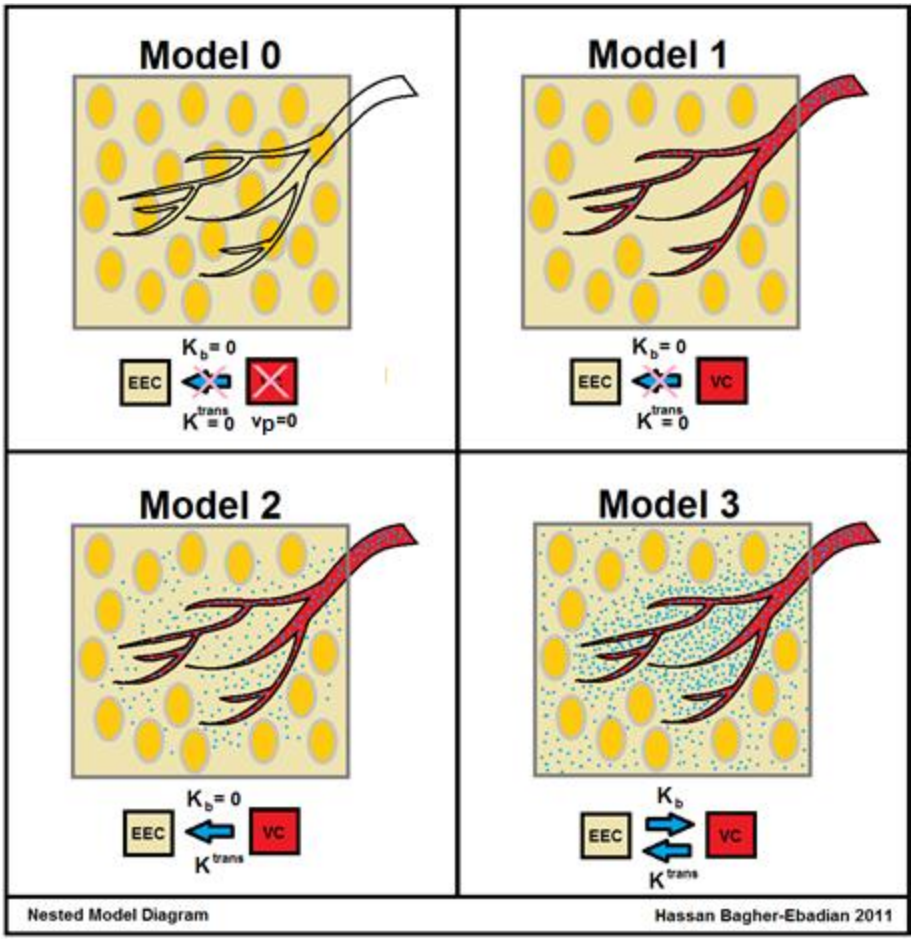

Figure 4.3. The four different models of vascular leakage. In Model 0 there is no evidence of vascular filling so there is no exchange of the CA between the two compartments ($K^{trans} = 0$, $k_b = 0$, $v_p = 0$). In Model 1 there is evidence of vascular filling but no leakage to the EEC ($K^{trans} = 0$, $k_b = 0$, $v_p \neq 0$). Model 2 indicates leakage from VC into the EEC but without reabsorption ($K^{trans} \neq 0$, $k_b = 0$, $v_p \neq 0$). Finally, Model 3 shows the case where not only leakage occurs from VC to EEC, but the CA that has leaked into the EEC will get reabsorbed into the VC ($K^{trans} \neq 0$, $k_b \neq 0$, $v_p \neq 0$).

Figure 4.4 shows the CA profile sampled from three different regions in the ΔR1 maps of a patient with Glioblastoma Multiforme (GBM). As seen here, the CA profile of Model 1 follows the trend of the AIF profile and does not indicate any leakage of the CA. But in Models 2 and 3, the tail of these profiles do not follow the profiles of the AIF and Model 1 tissues which is a sign of accumulation of CA and can be an indication of leakage of CA into the extravascular space.

Considering these profiles for different models, and also the equations that describe each of these (Equations 4.30 - 4.33) the next step in our method is fitting these profiles to these models and selecting the best model that can describe it.

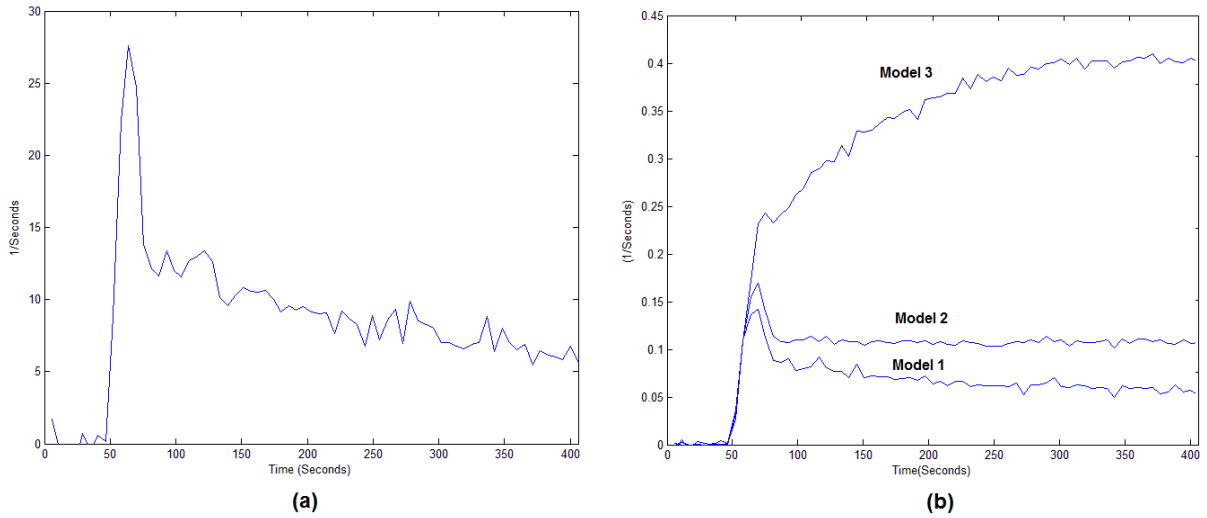

Figure 4.4. (a) The AIF sampled from a major artery in the ΔR1 images of a patient with GBM. This profile represents the CA concentration-time curve. (b) The CA concentration-time curves sampled from the same image as (a) but from three regions representing Models 1, 2 and 3.

4.4.2 Fitting the Models to the Pharmacokinetic Equation

Using the DR1 concentration-time maps, an Arterial Input Function (AIF) for each patient was picked similar to the one in Figure 4.4.a. Because there are a number of artifacts that might be introduced by the movement of blood through the image slice, and by T_2* signal loss, the AIF was adjusted by comparison to white matter in a normal area of the brain. An area of white matter was selected, and it was assumed that the v_p of the white matter was 1% [85]. The AIF was scaled so that the ratio of the integrated white matter concentration-time curve to that of the integrated AIF was 1%. Thus, all v_p's were measured relative to normal tissue white matter v_p.

A nonlinear least squares optimization using the Levenberg- Marquardt (LM) Algorithm[86] was used to fit model 3 to the experimental data, while the linear least squares method was used for the linear models (models 0–2). Using the AIF described in the previous paragraph, the concentration-time data in all voxels were fitted with the linear models 0, 1, and 2.

4.4.3 Selecting the Best Model

Model 1 was tested against model 0. If the F-test showed an advantage for models 1 and 2 was then tested against model 1. If the F-test showed an advantage for models 2 and 3 (the full

model) was then fitted to the data for further model comparison. To expedite the convergence rate of the fitting, the estimated parameters for the partial models in each step served as the initial values for fitting in the next step. Sum Squared Error (SSE) maps for the fitted parameters for all three models were calculated and used for statistical model comparison.

4.5 AVICENNA: Software Tool for Processing DCE Images

Using MATLAB GUI tools, we developed a software tool which we named "Avicenna Tool". This software tool is used for processing DCE-MRI images using the methods explained in the previous sections. Figure 4.5 shows the main interface of this software. As seen in this figure, this software tool has several modules for performing the different processing steps, from creating the T1-pre and the ΔR1 maps to Model fitting and model selection. The image formats that this software can read are HFH (Henry Ford Hospital) and DICOM and the results are saved as HFH. Multi-parametric maps are created for each slice after model selection which show the K^{trans}, v_e and v_p at different regions of these images

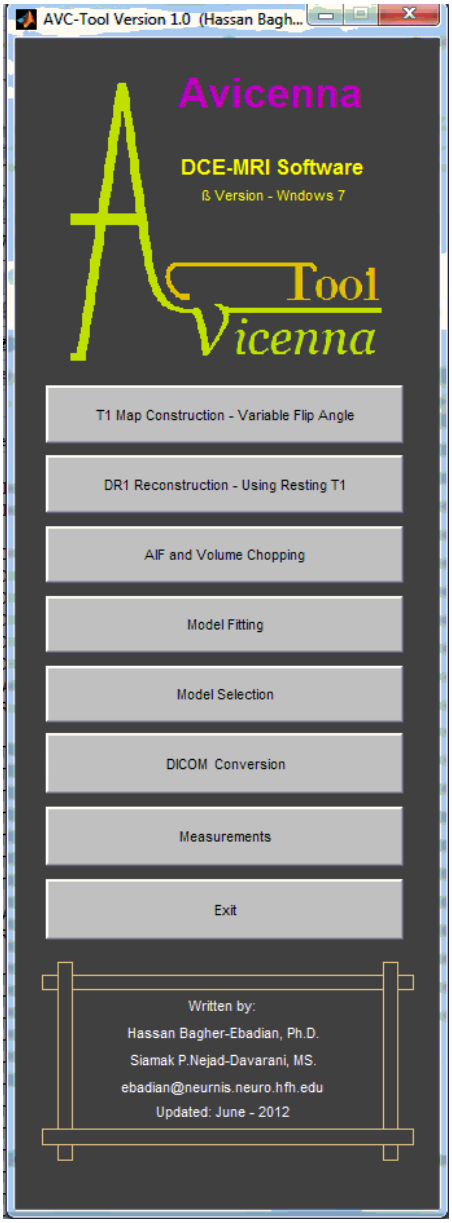

Figure 4.5. The main interface for "Avicenna" software tool. This tool is used for estimation of permeability parameters using DCE MR images.

CHAPTER V

THE EXTENDED VASCULAR MODEL: COMBINING THE EFFECTS OF DISPERSION AND VASCULAR LEAKAGE

In Chapter II we introduced our vascular model which was designed and implemented based on laws of fluid dynamics and vascular physiology. In Chapter III we showed the result of applying our model to DCE-CT images of the brain and there it was demonstrated that the model can explain dispersion in different levels of the vascular system of the brain. In section 3.4.3 the results of applying the model to an image with a tumor was shown and there we explained that since our vascular model was designed for healthy vessels (vessels with no leakage); therefore it is not able to explain the trend of the CA profile in DCE images that are sampled from regions with leaky vessels. After explaining the pharmacokinetic model and the concept of permeability and in chapter IV, we will proceed to introducing an extension of our vascular model that can explain the trend of the measured DCE signal from brain regions with leaky vessels.

5.1 The Extended Vascular Model

In this section, shortcomings of the vascular model and the steps for deriving the extended equation of the vascular model which includes parameters for leakage of the vessels will be discussed.

5.1.1 Adding Permeability Parameters to the Basic Vascular Model

The vascular model, in its current form, is able to describe dispersion of the contrast agent in areas of the brain where the vasculature is intact. In these areas, no leakage of the contrast agent

into the extravascular space is observed; therefore, the signals sampled from voxels in these areas mainly represent the CA profile in the intravascular space which is generally a dispersed form of the AIF profile in major vessels; however, when the CA leaks in the extravascular space, the tissue response observed in the images will follow a different trend.

Figure 5.1(a) shows the AIF sampled from a major vessel in a series of DCE-CT images of the brain. Figure 5.1(b) is the CA profile sampled from normal tissue and 5.1(c) is the CA profile sampled from the tumor in the same image series. As seen here, in contrast to the signal from the normal tissue, in the case of the signal being from the tumor area, as the timepoint increases, the intensity of this voxel increases as well; this rise of the tail of the CA profile indicates increase of the CA concentration in the extravascular space. If we use the transfer function of intact vessels for describing the transform of the AIF to the CA profile in these two cases, we get different results. As seen in Figure 5.1(d) the CA profile of the normal tissue that is estimated by transforming the AIF using our transfer function matches the sampled signal from the tissue very well; however, for the tumor voxels, the best fit would be the signal seen in Figure 5.1(e). Due to the elevated intensity of the ending timepoints, the fitting algorithm tries to fit the two curves by increasing the dispersion and delay time which erroneously finds the best fit in the last layer of the model and with a high delay time.

Based on this observation, to address the changes of the CA profile in areas with leaky vasculature and to find a more accurate estimation of the intravascular (plasma) CA concentration profile in these vessels, we modified our model to include leakage of the CA to the extravascular space. One by-product of this model is decomposing the signal to the intravascular and extravascular components. The result can be used for more accurate estimation of perfusion and permeability parameters in leaky areas which will be described later. Figure 5.2 shows a schematic diagram of different components in the pharmacokinetic model and their relation. $AIF(t)$ is the CA profile sampled at the location of one of the major arteries. The cube in this figure represents an imaginary voxel in the image where the tissue CA profile, $C_t(t)$, is being sampled from. $C_p(t)$ is the plasma CA concentration in the vessel (or vessels) feeding the tissue in the voxel. It should be noted here that the profile of $C_p(t)$ and the average profile of the intravascular CA concentration in the voxel are not necessarily the same and theoretically there will be a slight difference between these two due to dispersion and delay effects based on the

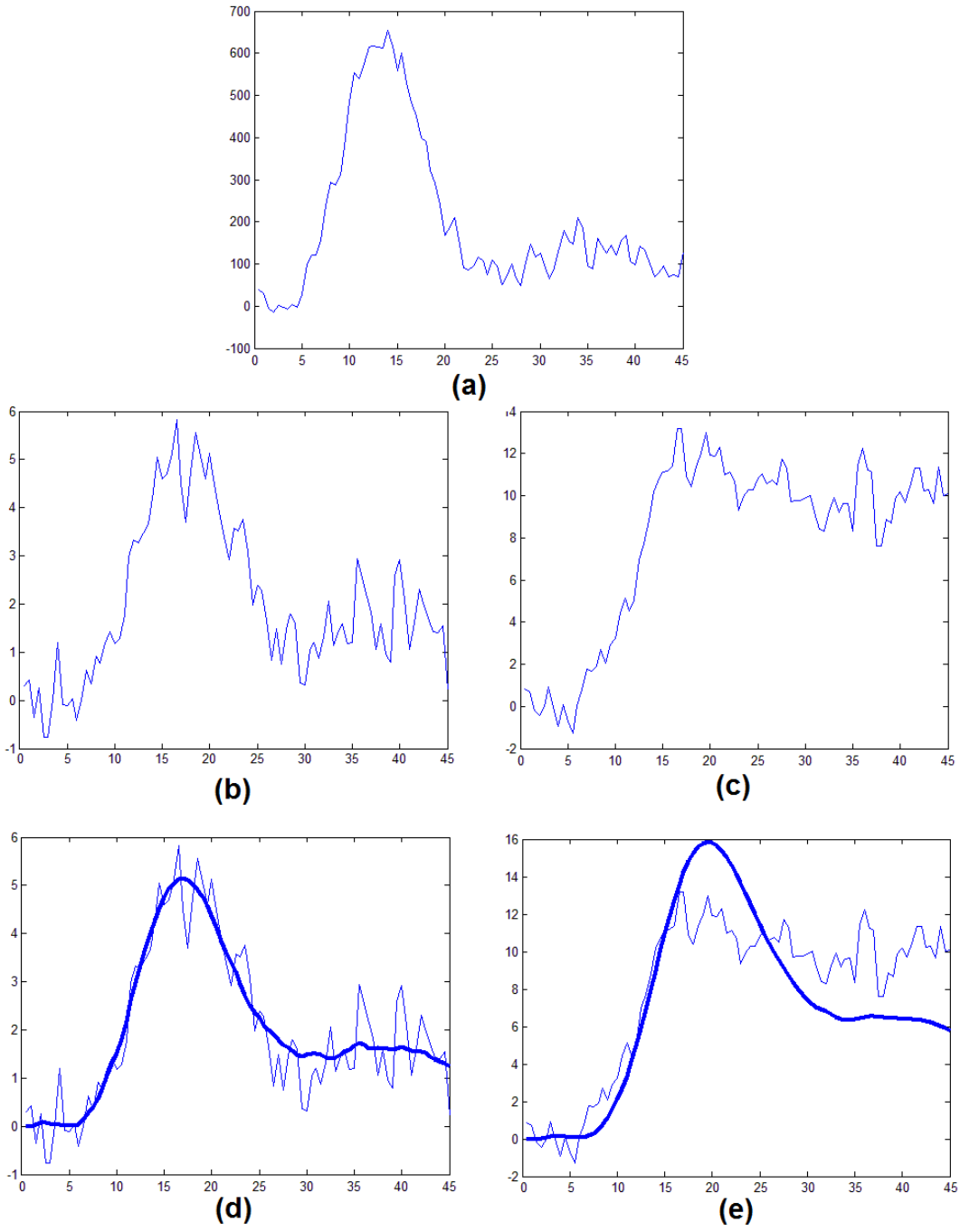

Figure 5.1. (a) The AIF sampled from a major vessel in the DCE-CT image series and the CA profiles sampled from (b) normal tissue (non-leaky vasculature) and (c) the tumor area (leaky vasculature). Using our vascular model, the transfer function that gave the best fit for each of the two CA profiles and the resulting TIF was found. As seen here, for the non-leaky vasculature case, the resulting TIF can give a good estimation of the signal sampled from the tissue (d). But in the case of the signal sampled from the tumor area, the best fit signal cannot follow the trend of the AIF and the best fit model is erroneously selected as the sixth level to minimize the residual error of the fitting procedure.

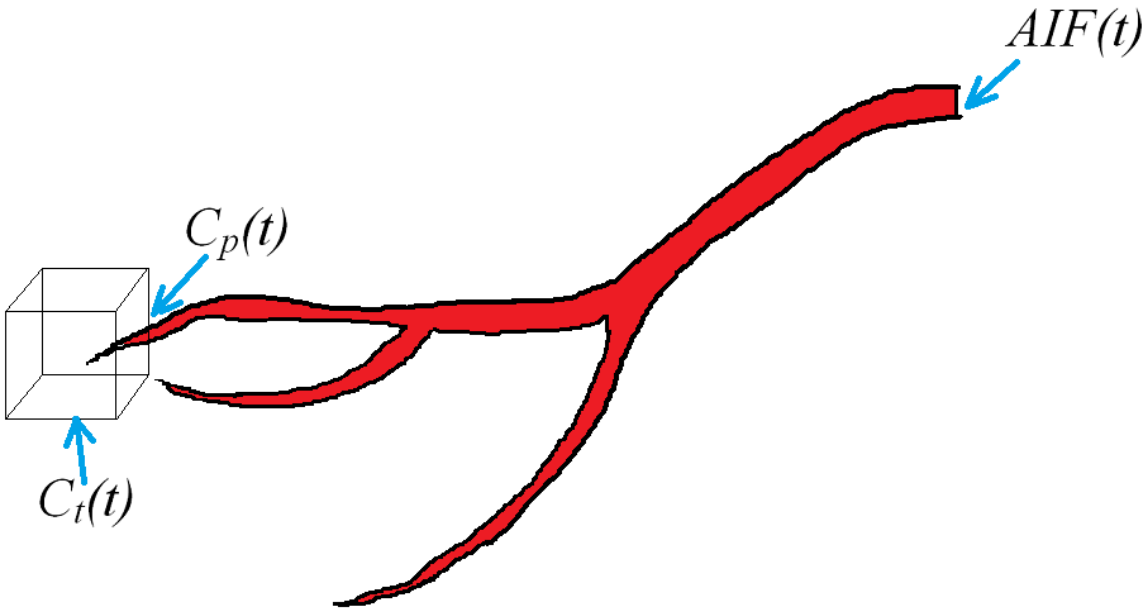

Figure 5.2. Schematic diagram showing the main components in the pharmacokinetic model and their location. AIF(t) is CA profile sampled at the location of one of the major arteries. The cube in this figure represents an imaginary voxel in the image where the tissue CA profile, $C_t(t)$, is being sampled from. $C_p(t)$ is assumed to be the plasma CA concentration in the vessel (or vessels) feeding the tissue in the voxel.

vascular structure in the voxel; however, considering the time resolution of the DCE signals and the noise level in the images, the difference will be negligible and in the following equations and calculations, we will use the same notation for both of them.

According to Equation 4.1, in the pharmacokinetic model, the relationship between $C_t(t)$ and $C_p(t)$ is as follows:

(5.1) $$C_t(t) = K^{trans} \int_0^t e^{-k_b(t-\tau)} C_p(\tau) d\tau + v_p C_p(t)$$

In this equation, the signal $C_t(t)$ is composed of two main components: the second term on the right, $v_pC_p(t)$, basically represents the time trace of the plasma CA concentration in the vessels that feed the tissue that $C_t(t)$ is being sampled from and is dependent on the fractional plasma volume, v_p. The first term on the right, $K^{trans} \int_0^t e^{-k_b(t-\tau)} C_p(\tau) d\tau$ represents the component of

the signal that is due to leakage of the CA to the extravascular space and is dependent on the forward (K^{trans}) and inverse (k_b) transfer rate constants.

As we mentioned in the introduction chapter, in conventional methods of calculating the permeability parameters using the pharmacokinetic model, for $C_p(t)$, the CA profile sampled from one of the major arteries or veins (such as the superior sagittal sinus) is usually used. However, this is not a correct representative of the CA profile in the tissue since it does not address dispersion of the CA profile in the tissue and can lead to biased estimates of the permeability parameters. Here we introduce a method that using our model and the pharmacokinetic model, separates the two components that create $C_t(t)$. This can be used for estimation of both permeability and perfusion parameters.

To address the problem of finding the intravascular CA profile in leaky vessels we added a new feature to the transfer function. According to the definition in Equation 3.2, the intravascular CA concentration profile or Tissue Input Function (*TIF*) can be found using the following equation:

(5.2) $$TIF(t) = AIF(t) * h(t)_{1\ to\ x} \qquad x = 1\ to\ 6$$

Where $h(t)_{1\ to\ x}$ is the transfer function of the vessels from the major artery to a location in the tissue and based on Equation 3.1, $h(t)_{1\ to\ x}$ also includes a factor g, which is the system gain to compensate for the number of branches of vessels that can exist in the voxel being sampled. This equation gives a good estimate of the profile of the CA in the tissue vasculature or TIF. If in Equation 5.1, we replace the CA concentration profile in plasma $C_p(t)$, with the TIF we can write the pharmacokinetic model as follows:

(5.3) $$C_t(t) = \frac{K^{trans}}{v_p}\int_0^t e^{-k_b(t-\tau)}TIF(\tau)d\tau + TIF(t)$$

And by replacing TIF from 5.2 we get the following equation:

(5.4) $$C_t(t) = \frac{K^{trans}}{v_p}\int_0^t e^{-k_b(t-\tau)}(AIF(\tau) * h(\tau)_{1\ to\ x})d\tau + AIF(t) * h(t)_{1\ to\ x}$$

(5.5) $$C_t(t) = \frac{K^{trans}}{v_p}e^{-k_b t} * AIF(t) * h(t)_{1\ to\ x} + AIF(t) * h(t)_{1\ to\ x}$$

(5.6) $$C_t(t) = AIF(t) * h(t)_{1\ to\ x} * \left(\frac{K^{trans}}{v_p} e^{-k_b t} + \delta(t)\right)$$

(5.7) $$C_t(t) = AIF(t) * \left[h(t)_{1\ to\ x} * \left(\frac{K^{trans}}{v_p} e^{-k_b t} + \delta(t)\right)\right] = AIF(t) * h_E(t)$$

Where

(5.8) $$h_E(t) = h(t)_{1\ to\ x} * \left(\frac{K^{trans}}{v_p} e^{-k_b t} + +\delta(t)\right)$$

The transfer function $h_E(t)$, which we will refer to as the Extended Vascular Model, describes transformation of the AIF profile to the measured tissue response at different locations of the vascular structure, with or without leakage of the vessels. In the case where the vessels are intact (non-leaky), K^{trans} will be zero and the measured signal will be basically the intravascular plasma concentration of the CA which can be described by convolving the AIF with $h(t)_{1\ to\ x}$.

Previously several approaches have been suggested for correcting the MR signal in DSC-MRI studies for more accurate estimation of perfusion parameters. These approaches have been focused on methods such as parametric modeling by fitting a gamma-variate curve to the tissue response function [87], estimation of CA extravasation from the tissue residue function after AIF deconvolution [88]. estimation of extravasation using the voxel-wise deviation from the tissue response curve in a non-leaky areas [89]. Bjornerud et al. have combined this with the deconvolution method to directly estimate parameters of CA extravasation and perfusion from the tissue residue function extravasation for correction of T1- and T2*-dominant extravasation [90]. Our method has a similar approach however we have made no assumption about the shape of the residue function and also we are using the direct estimation of the transfer function equation based on fitting methods. Also, our transfer function based on the EVM does not consider the T1 and T2* competing mechanisms and in MR images and adjustments need to be done for applying it to DSC-MR images.

5.1.2 Using the Extended Vascular Model for Decomposing the Tissue Response Signal

The next step is to use the new transfer function for describing transformation of the AIF to the measured tissue response in voxels at different regions of the DCE image. The parameters of the

transfer function that can best describe this transformation can give information about the vascular structure and also permeability of the vessels in these voxels. We employed the fitting method as described in section 3.1.1, but by using the Extended Vascular Model, $h_E(t)$, as the transfer function.

To find the best fit, the transfer function equations for different levels of the vascular branching were implemented and for each equation, the fitting procedure was repeated. The number of parameters used in the fitting procedure varied from 5 to 10 parameters.

Figure 5.3 shows the result of using the new transfer function in the fitting procedure. The two tissue response signals are the same as those in Figure 5.1. In Figures 5.3(a) and 5.3(b) the bold lines show the best curves that are fit to the signals sampled from the normal tissue and tumor areas respectively. A comparison of these curves with those in 5.1(d) and 5.1.(e) show that the new transfer function can explain the tissue response function in both tissues with intact and leaky vessels.

Another useful result of using the Extended Vascular Model in the fitting procedure is separation of the signals resulting from the intravascular and extravascular compartments. After finding the curve that best fits to the sampled signal, using the parameters found in the fitting procedure and also the two main components of the Extended Vascular Model, the transfer functions describing the extravascular and intravascular components of the tissue response signal can be constructed and by convolving them with the AIF profile, each can be found as below:

(5.9) $$C_t^I(t) = AIF(t) * h(t)_{1\ to\ x}$$

(5.10) $$C_t^E(t) = \frac{Ktrans}{v_p} e^{-k_b t} * AIF(t) * h(t)_{1\ to\ x}$$

Where $C_t^I(t)$ and $C_t^E(t)$ are the Intravascular and Extravascular components of the tissue response function respectively. Using these equations, the bold curves in 5.3(a) and 5.3(b) are decomposed into the Intravascular and Extravascular components as seen in 5.3(c) and 5.3(d). Figure 5.3(c) shows the signal from tissue with normal vasculature and therefore we do not expect any extravascular component in the signal. The fitting results confirm this fact and the extravascular component is a flat line which is the result of K^{trans} = 0 in Equation 5.10. In

contrast, in Figure 5.3(d) both Intravascular and Extravascular components of the tissue response signal exist which is the case in tissue with leaky vasculature. The important outcome of this method is getting an estimate of the flow component of the tissue response signal in tissues with leaky vasculature. This can be directly used for estimation of the perfusion parameters. This application will be discussed in Chapter VI.

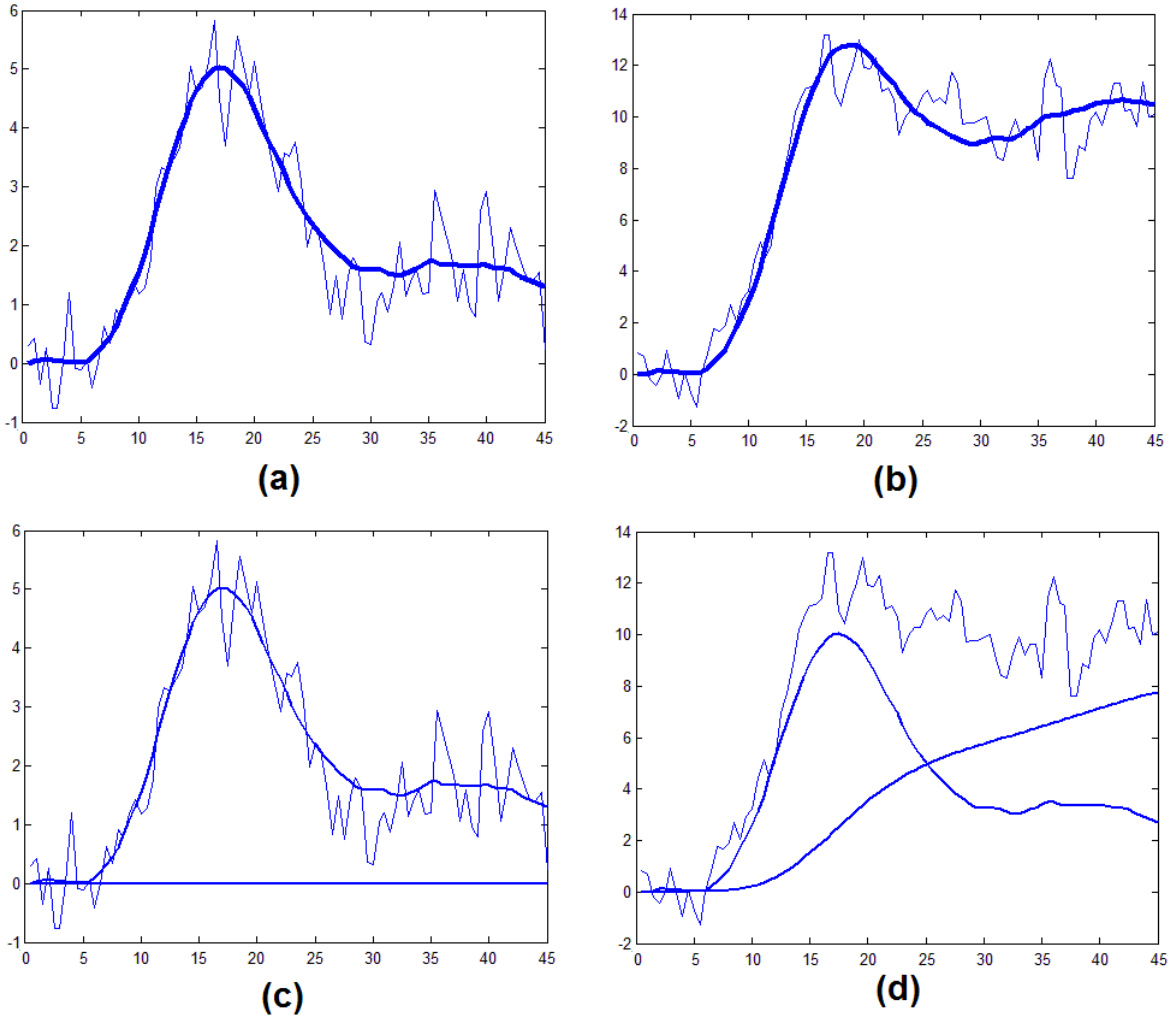

Figure 5.3. The best fit curves to the signals sampled from (a) normal tissue and (b) the tumor area (same as the curves in figure 5.1) using the Extended Vascular Model (EVM) which is consisted of flow and leakage parameters. The bold curve shows the best fit curve in each case. Figures (c) and (d) show the decomposed signals based on the flow and leakage model. The sum of the two curves in (c) and (d) would result in the bold curves in (a) and (b) respectively. As seen in (c) the signal is from the normal tissue and does not represent any leaky vasculature and the fitting method has found the best fit in $K^{trans} = 0$ which has resulted in the component due to vascular leak be flat and only flow paramaters have formed the final result of the fitting. In contrast, the decomposed bold curve in (c) can be seen here as two curves; the curve with a profile similar to the AIF is the flow component of the signal and the other curve is the signal from the CA that has leaked into the extravascular space.

5.2 Testing the Extended Vascular Model on DCE images

In this section, we will test the EVM model on DCE-CT and DCE-MRI images to explore the performance of this model for detecting the level of the vascular branches and the permeability status in different regions of the brain images.

5.2.1 Testing the EVM on DCE-CT images

Using the Extended Vascular Model (EVM) we applied the fitting procedure explained in section 5.1.2 to the voxels in a DCE-CT images series. To compare the results with using the vascular model with no leakage (which we will refer to as the Basic Vascular Model or BVM) we repeated the same procedure using this model as well. For each model, the fitting procedure was repeated for the six different vascular branching levels. Figure 5.4 shows the residue maps of the fitting procedure using the BVM and EVM. One of the major observations in these images is the residue values of the voxels representing the tumor (which is marked with a "T"). In the residue maps in the top row, the tumor can be seen in all levels which indicates that the BVM cannot find a good fit to the data in any level of the vascular model; however, as the level index increases, the residue gets smaller which is due to the increased dispersion and elevated tail of the resulting curve as explained in figure 5.1(d); despite this, even in the residue map of L6 for the BVM, there is still a trace of the tumor. In contrast, in the EVM residue maps, the tumor map starts to appear after the L4 level and prior to that level, the residue is so low that in cannot be visually detected. Although the EVM has more parameters than the BVM (three more parameters in each level), its ability to provide a better fit cannot be necessarily attributed to higher number of parameters. The L1 of EVM has the same number of parameters as the L4 of the BVM and lower number of parameters than L5 and L6 on BVM but the fitting residue is less than these. These maps are shown only for visualizing the performance of these methods; to accurately determine the best fit, we will use model selection using the values in these residue maps. The results of model selection and also the permeability maps that have been created using this approach will be presented in section 6.2.2.

Another observation in these two image series is the similarity of the residue maps at different levels for these two models in areas with intact (non-leaky) vessels. This demonstrates that the performance of the EVM in non-leaky areas is similar to the BVM, meaning that the effects of

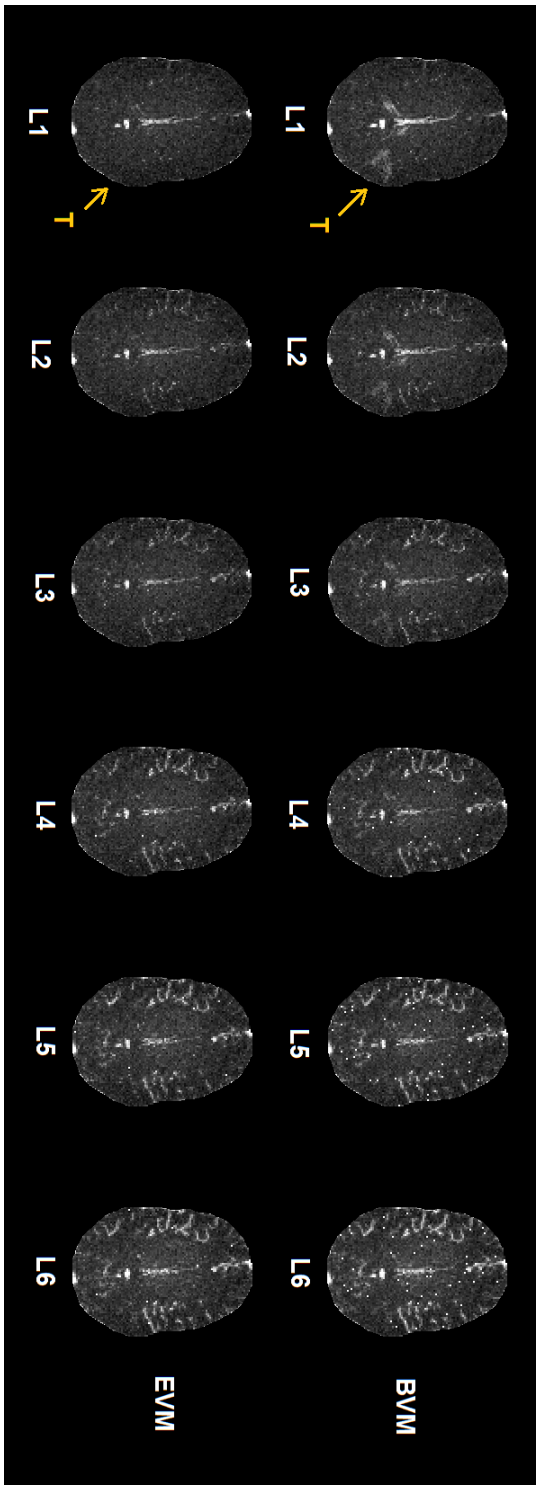

Figure 5.4. The residue maps of the fitting procedure using the BVM and EVM, each done with up to six branching levels. In the residue maps in the top row, the tumor (marked with a "T") can be seen in all levels which indicates that the BVM cannot find a good fit to the data in any level of the vascular model; but this is not the case with the residues of the EVM. Also, the residue pattern in the non-leaky areas in both images are very similar which indicates that the permeability parameters of the EVM have been suppressed in these regions.

leakage of CA to the extravascular space will be suppressed in the fitting procedure. Also, observing the best fit for the tumor in the lower levels of this image set can be directly related to the level of the artery or arteries that are feeding the tumor. To further explore this, more tumor cases should be studied. The reason that the veins have residues in all levels is that our model is designed to explain dispersion of the CA profile only up to the capillary level and the effects of the veins and venules have not been accounted for. However, since the CA concentration profile in the veins and venules is closer to the capillaries, as the level index increases, the residual values decrease in the veins and the best fit for voxels from these structures happens at the sixth level.

5.2.2 Applying the EVM to DCE MR Images

To further investigate the application of the EVM in DCE imaging modalities, we used DCE MRI data to explore the feasibility of using this model for describing dispersion and leakage in these images.

DCE MR Images of patients with cerebral tumors were acquired using the protocol described in section 4.1.2 and using the T1 map created using the DESPOT1 method (As described in section 4.3.2) the temporal $\Delta R1$ images were created by the method explained in section 4.2.1. The intensity of the $\Delta R1$ images represents the CA concentration in these images. Figure 5.5 shows one slice of the post-contrast DCE MR image and three ROIs sampling the CA concentration profiles from (a) A major artery from the circle of Willis (b) Normal White matter tissue and (c) the Tumor which has leaky vessels. One major difference between the temporal signals in our MR images and the DCE CT images is the temporal resolution of these signals. The DCE-CT images have a temporal resolution of 0.5 seconds and the temporal resolution of the DCE MR images in our study is 5.367 seconds. This means that the difference in the rise time of the profiles from the main inlet to the main outlet of the brain will at most be one timepoint. Therefore, when applying our model to this data, the major factor for fitting the curves will be dispersion of the CA profiles rather than delay in the rise time. Using the BVM and the same procedure for finding the transfer function that gives the best fit to the profiles in (b) and (c), the bold curves in (d) and (e) were found as the best fit.

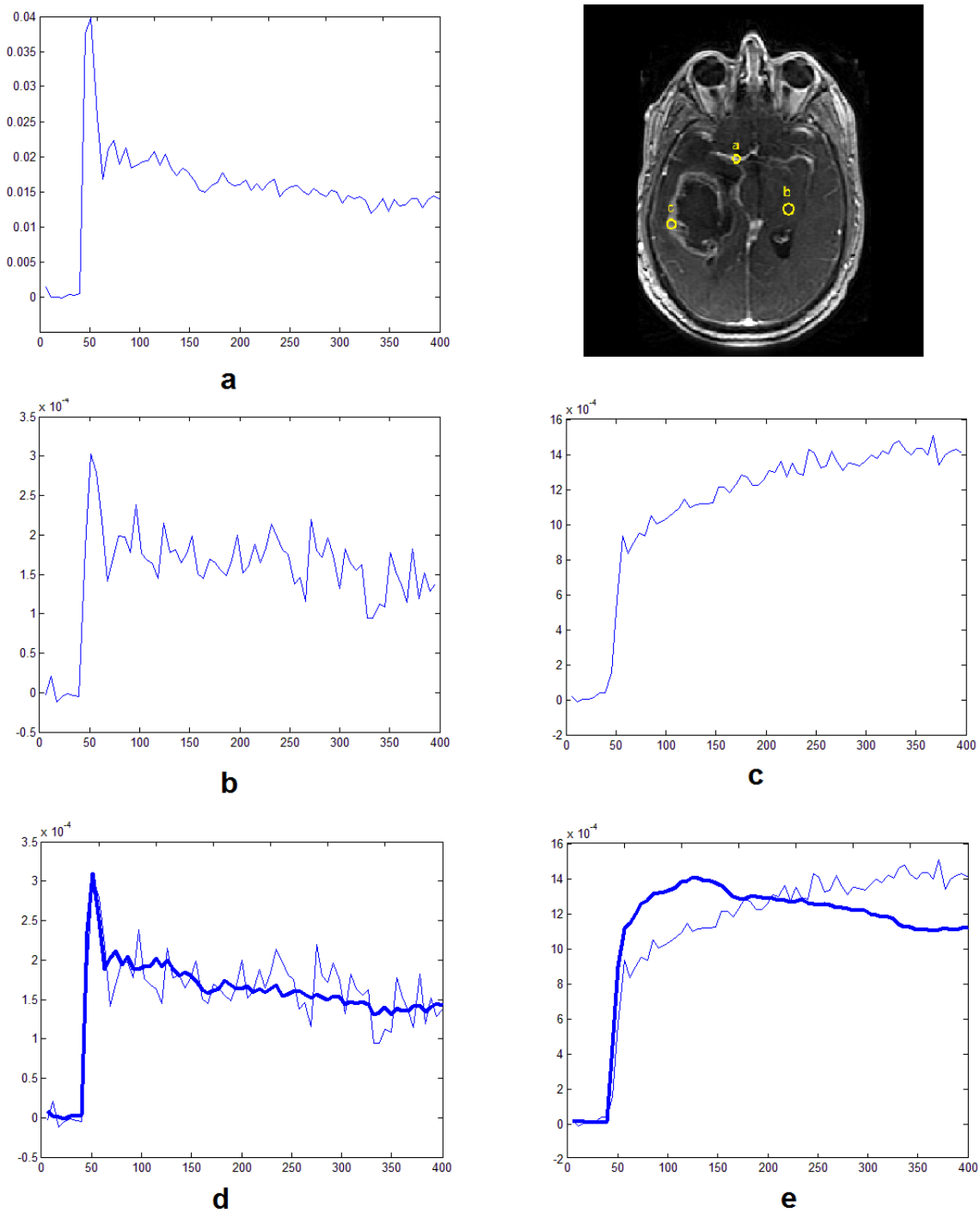

Figure 5.5. One slice of the post-contrast DCE MR image and the three ROIs sampling the CA concentration profiles from (a) A major artery from the circle of Willis (b) Normal White matter tissue and (c) the Tumor which has leaky vessels. Figures (d) and (e) show the best fit curves using the transfer function found using the BVM. As seen here, the curve fit to the normal tissue follows the trend very well but even in the best fit curve, this model is not able to match the sampled data from the tumor.

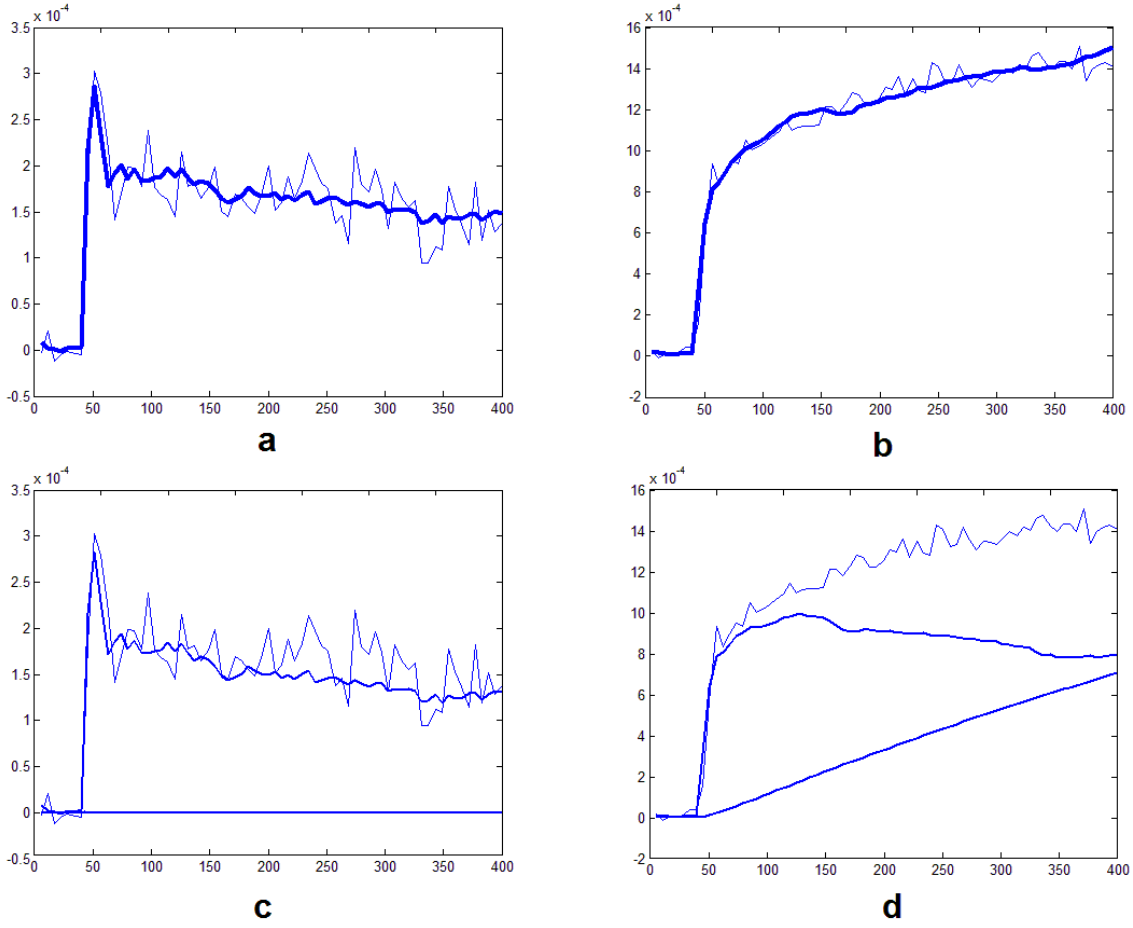

Figure 5.6 (a) The best fit curve to the signal sampled from the normal tissue and (b) The tumor area. (c) Shows the flow and leakage components of the bold curve in a. As seen here , the leakage component is a flat line indicating no leakage (d) The two components of the bold signal in b shows that in addition to the flow component, there also exists a component indicating leakage.

As seen in this figure, in the case where the profile is sampled from the normal tissue (no leaky vessels), the BVM can find a good fit to the tissue response that follows the trend of the profile very well; however, when the data is from the tumor area, even the best fit is far from the sampled curve.

We repeated the fitting procedure as the DCE-CT case, using the EVM. Figure 5.6 shows the best fit curves to the CA profiles in Figure 5.5(b) and 5.5(c). We applied this fitting procedure to all the voxels in a set of DCE-MR Images using both BVM and EVM. The residual value maps of this procedure are seen in Figure 5.7. Similar to the DCE-CT case, the EVM is able to find a good fit for the CA profile in the tumor area which leads to the fitting residual values to be much

lower for the first two branching levels of this model. Considering the location and the size of the tumor in the brain, it is likely that it is being fed by one of the major arteries such as the ACA or an immediate branch of it which leads the CA profile have a good fit in the lower branching levels. The BVM is not able to find a good fit to the CA profile in the tumor area in any of the branching levels which is what is expected.

As in the DCE-CT case, the two models show similar residual patterns in areas with non-leaky vessels which indicates that when the permeability parameters (or more specifically K^{trans}) are suppressed, EVM performs similar to the BVM. This will be discussed in more detail in Chapter VI.

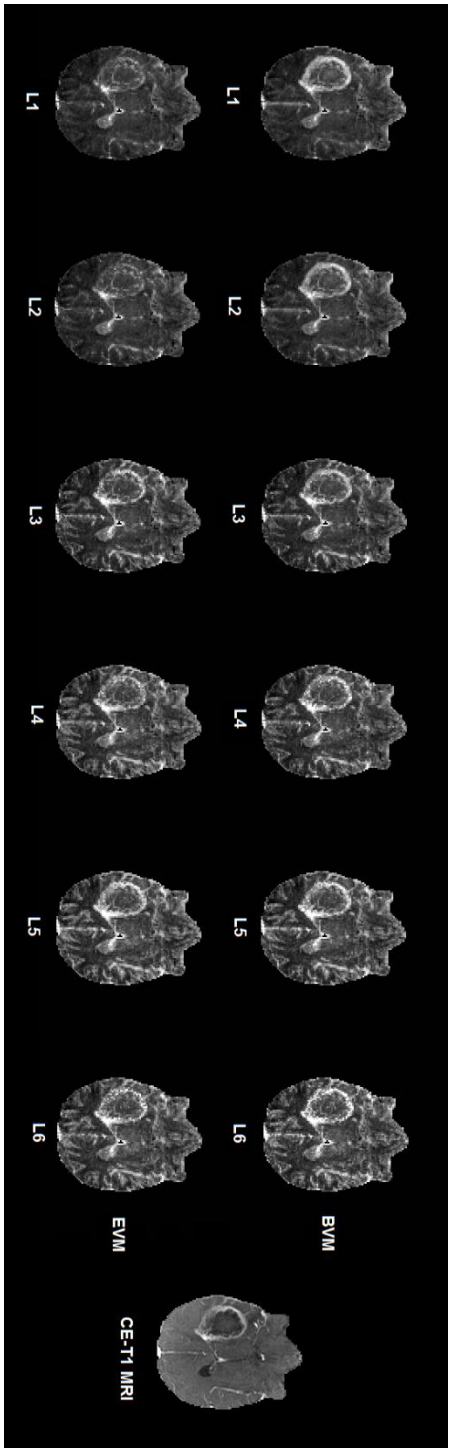

Figure 5.7. Maps of the fitting residual values using the EVM and BVM in a set of DCE MR Images. The residual values in the tumor area are much lower for the EVM which means that this model can explain the trend of the CA profile in the leaky vasculature areas much better than the BVM. Finding the best fit in the lower levels can be due to the tumor being fed through a major artery in the lower branching levels.

CHAPTER VI

RESULTS OF USING DIFFERENT AIF PROFILES AND THE CORRECTED TIF PROFILE

In Chapter IV, we introduced the methods and software that we have developed for estimation of permeability parameters in DCE-T1 and Dynamic Dual-Gradient-Echo images. In this chapter we will discuss the effects of selecting different AIFs in the Pharmacokinetic model and show how it changes the estimated values of the permeability parameters. Initially in section 6.1we will demonstrate the effects of using different AIFs on the estimated permeability parameters and also the difference in the estimated parameters when using the DCE-T1 Signal Intensity instead of the ΔR1 signal. Finally we will compare the permeability and perfusion parameters estimated by using the conventional AIF and the TIF found by the EVM using both DCE-MRI and DCE-CT data in tumor patients as well as in simulated DCE-MR signals.

6.1 Effects of Using Different AIFs on the Estimated Permeability Parameters

In this section, the results of a two comparison studies will be presented that show the effects of using different AIFs for calculation of permeability parameters. The calculations in this section have been done using the conventional method of using one global AIF for all voxels in the brain.

6.1.1 Using Standard Radiological AIF vs. and Manually Selected AIF

The purpose of this portion of the study was to compare the results of using a Standard Radiological Arterial Input Function (SRAIF) vs. the Manually Selected Arterial Input Function (MSAIF) in Dynamic Contrast Enhanced (DCE)-MR image analysis to compare the estimated permeability parameters such as extracellular-extravascular space volume (v_e), plasma volume (v_p) and forward vascular transfer constant (K^{trans}). The SRAIF is the result of a previous study [91, 92] where 13 Wistar rats were injected with radiolabeled Gd-DTPA and CA concentration was sampled at the Carotid Artery of rats at a relatively high temporal resolution by counting β emissions in a well counter at different time points . The measured AIF profiles were then calibrated to the blood relaxivity and averaged to construct the SRAIF. This SRAIF is considered to be a standard curve representing the AIF measured in the carotid artery for use in the Pharmacokinetic model for rats. Figure 6.1 shows the SRAIF and one MSAIF used in this study.

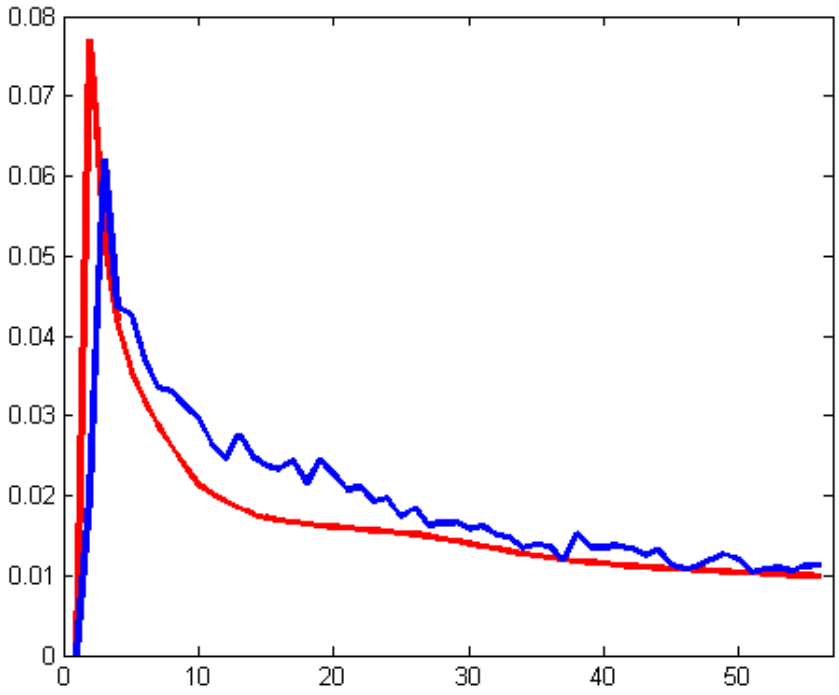

Figure 6.1. The normalized and rise-time corrected SRAIF (red) and MSAIF (blue) from of one of the rats after intravenous bolus injection of GD-DTPA

In the current study, Nine Fisher 344 female rats were inoculated intra-cerebrally with 9L Gliosarcoma cells that were cultured in Dulbecco's modified eagle's medium (DMEM) supplemented with 10% fetal bovine serum (FBS). Cells were harvested and re-suspended and 5 µl of the cell suspension with a concentration of 8×10^7/ml was implanted into the rat brain. Imaging was done using Gd-DTPA on the 14^{th} day after inoculation.

For imaging, the animals were scanned on a GE-3T clinical system (Signa Excite, GE health) using a 50mm(diameter)×108mm RF rung length small animal imaging coil (Litzcage small animal imaging system, Doty Scientific Inc., Columbia, SC). One set of T1-pre followed by a set of DCE-T1 weighted images and a set of T1-post images were acquired in each experiment. For creating the resting (pre-contrast) T1 maps, multiple flip angle (2°, 5°, 10°, 15°, 20° and 25°) fast 3D Spoiled Gradient Echo (3D SPGRE) images were obtained using the following MR specifications: TR/TE=500/12 ms, 256×256 matrix, 13 slices, 1 mm thick, 40×30 mm FOV, NEX=4. A series of 3D SPGRE (flip angle = 30°) image packs were acquired every 11.7 sec for a total scan time of 15 minutes. Gd-DTPA was administered as a bolus through the tail vein of animal over 10 seconds at 0.2 ml/kg (0.1 mmol/kg). We used our Model Selection approach [66] (as described in section 4.4.3) to estimate permeability parameters from these DCE-MR experiments as explained in chapter IV using Tofts extended model and its reduced forms [65]. Using the methods explained in chapter IV [66], resting T1 maps along with the baseline (before CA administration) of the dynamic signal were used to calculate the relaxivity change (ΔR_1). F-Statistic was used to select the best model for each voxel. Model 3 was the focus of this study due to the fact that it allows us to measure three permeability parameters (v_p, v_e, and K^{trans}). All analyses were done using SRAIF and MSAIF. The MSAIFs were selected by an expert radiologist for each animal. For each animal and for each CA, two AIF profiles were used for the analysis: Both AIFs were calibrated to blood relaxivity and normalized to the CA concentration of the white matter. Also, the SRAIF profile was shifted in time so that its rising point matched that of the AIF in the same animal (Figure 6.1).

Table 6.1 shows the mean and standard deviation of v_p, K^{trans} and v_e that have been measured for the whole lesion (only Model 3 areas) in all nine animals. For assessment of the significance of the difference of the mean values of each of the parameters between the two groups, paired T-

test was performed along with calculation of the Intra-class Correlation (ICC) between the results from using the two AIFs.

These results show high correlation between the K^{trans} values calculated using the two AIF profiles (ICC = 0.94) which shows perfect agreement; Also, the mean values of v_e and v_p have a lower correlation when they are calculated for the two different AIFs (for v_e , ICC = 0.42 and for v_p, ICC = 0.56).

The results show less variation in the estimated values of K^{trans}, compared to v_e, v_p. Thus using MSAIF compared to SRAIF would not significantly affect K^{trans} due to the fact that this parameter is relevant to the trend of the time trace of CA concentration in both AIFs. However, v_e and v_p are more susceptible to the AIF profile change. These results show the importance, sensitivity and biasing level of each estimated permeability parameter against different AIF profiles. Further investigation using Quantitative Auto-Radiography (QAR) and histology measurements of the vascular physiology parameters would allow us to investigate the accuracy and biasing effect of each AIF on the estimated parameters.

Table 6.1. Mean and standard deviation of the permeability parameters, estimated using the SRAIF and MSAIF. The P-value of the Paired T-test and the Inter-Class-Correlation were calculated between the estimated values of the permeability parameters calculated using the two AIFs.

	GD-DTPA		
	SRAIF	MSAIF	P-value/ICC
K^{trans} (min^{-1})	0.046±0.011	0.048±0.010	0.3008/0.9382
v_e (%×100)	0.236± .056	0.202± .031	0.1289/0.4203
v_p(%×100)	0.016±0.004	0.016± .006	0.9102/0.5620

6.1.2 Comparison of Results Using DCE T1 Signal Intensity vs. ΔR1

In section 4.2.3, we explained that recently there have been studies that suggest using the normalized DCE T1 signal instead of ΔR1in permeability studies. However, there has been no report of comparing the results obtained using these two methods. Here we present the results of a comparison study that we did to investigate the difference of the estimated parameters.

For this study DCE-T1 imaging was conducted in 10 treatment naive patients with GBM. All studies were performed in a 3T GE Excite HD MR system using a standard eight-channel phased-array RF coil and receiver. Before CA administration, T1 mapping was performed using a 3D SPGRE sequence with Variable Flip Angle (VFA). Sequence parameters were as follows: TE/TR ~ 0.84/5.8 ms, flip angles, θi, of 2, 5, 10, 15, 20, and 25º, matrix of 256 ×128, FOV of 240 mm, 16 slices, 5 mm slices, no gap. The maps of T1 were used to establish baseline pre-contrast values for the dynamic SPGRE procedure that followed. The 3D SPGRE DCE-T1 sequence was then begun (70 image sets ~5.9s per image set, θ=20 and other parameters as above). About 20s after starting, a dose of Magnevist (0.1 mmol/kg) was injected (IV) at a rate of 4 mL/s. ΔR1 was calculated analytically for each voxel using the nominal value of the tip angle, θ , the estimated pre-contrast value of T1, and the ratio of the post-contrast to baseline pre-contrast MRI signal. For calculation of ΔR1, we used the equation in section 4.2.2 a measure of the CA concentration-time curve. Using a manually chosen Arterial Input Function (normalized to white matter), the SI and ΔR1 data in all voxels were fitted with the linear models 0, 1, 2 and non-linear model 3 as explained in section 4.4.1. Sum Squared Error (SSE) maps for the fitted parameters in all three models were calculated and used for statistical model comparison. Three F-test maps were constructed using the SEE maps that served for model comparison. Model 0 vs. 1, Model 1 vs. 2 and Model 2 vs. 3 were tested with the F-test criteria and a final regional map, and three maps of permeability parameters were constructed accordingly.

Table 6.2 shows the results of estimating the permeability parameters using these two signals. As seen here, compared to the ΔR1 technique, the SI technique underestimated the plasma volumes (v_p) for different regions (32% in normal but enhancing core, 26% in white matter, 17% in gray matter, and 32% in Model 2 and 24% Model 3 regions). In contrast to the ΔR1 technique, the SI technique also underestimated K^{trans} around 22% and 28% in regions `associated with Model 2 and 3 respectively.

The SI technique also overestimated k_b around 23% in the model 3 region compared to ΔR1. The mean calculated interstitial space $v_e = K^{trans}/k_b$ (only in Model 3) was underestimated about 38% in the SI technique compared to the ΔR1 technique. In Model 3 regions, excellent curve fits were obtained in both of the techniques to explain the variation of the ΔR1 and SI data (mean R2 = 0.99 and 0.97 for ΔR1 and SI techniques respectively). Results imply that estimation of

pharmacokinetic parameters using the SI technique results in values that are significantly different with those estimated using the ΔR1, considering the fact that the ΔR1is a better indicator of the CA concentration, it is expected that the permeability parameters estimated using this signal would be closer to the actual value; however, validation of these parameters requires other methods such at histology or autoradiography.

Table 6.2. Summary of estimates of vascular parameters in 10 patients. These results show the signifinant difference between the estimated permeability parameters using the Signal Intensity and the ΔR1.

	Model 1 (core)	Model 2		Model 3			
Permeability Parameters	v_p	v_p	K^{trans}	v_p	K^{trans}	v_e	R^2
Mean ± SD (ΔR1)	0.0213 ± 0.0195	0.028 ± 0.025	0.0019 ± 0.0019	0.037 ± 0.019	0.019±0.010	0.076 ± 0.048	0.9912
Mean ± SD (SI)	0.0144 ± 0.0163	0.019 ± 0.021	0.0014 ± 0.0027	0.028 ± 0.024	0.013 ± 0.016	0.045 ± 0.034	0.9724

6.2 Results of Using the Model Corrected AIF

In the previous section, we demonstrated that using different AIFs can lead to biased estimates of the values of permeability parameters, especially v_e and v_p. In the following sections, the results of using the TIF using our vascular model for perfusion and permeability studies will be explored and the results will be compared to the those obtained using conventional methods. In the next session, we will first briefly review the methods for estimating the main perfusion parameters and next, we will show the application of the EVM for less biased estimation of these parameters.

6.2.1 Estimation of Perfusion Parameters in DCE-CT Imaging Using the EVM

In perfusion analysis, Cerebral Blood Volume (CBV), Cerebral Blood Flow (CBF) and Mean Transit Time (MTT) are estimated based on Fick's General Principle [93] :

$$Q(t) = F \int_0^t [C_a(u) - C_v(u)]du \tag{6.1}$$

Where $Q(t)$, $C_a(t)$ and $C_v(u)$ are defined as the tissue, arterial and venous CA concentrations and F is the cerebral blood flow. $Q(t)$ is also referred to as the Tissue Concentration or Tissue Residue Function. The units for $Q(t)$,$C_v(u)$ and $C_a(t)$ are ($mmol.\ mL^{-1}$) and the unit used for F is ($mL.\ min^{-1}.\ 100\ g^{-1}$).

One practical but approximate method for estimating the blood flow using this equation is to do measurements of $Q(t)$ and $C_a(u)$ within the mean transit time of the brain (4.5-6.5 seconds) [93]. This way, the venous outflow will be assumed to be zero and the equation can be written as:

(6.2) $$Q(t) = F \int_0^t C_a(u)du$$

The estimated Flow using this method is very inaccurate and the results do not tend to be consistent. An alternative method for estimating the CBF is deconvolution analysis. This method does not make any assumptions about the venous outflow being non-existent. The base of the deconvolution method is the following equation:

(6.3) $$Q(t) = F\,.\,C_a(t) * R(t)$$

This equation describes a relationship between $C_a(t)$ and $Q(t)$ through $R(t)$ which is called the impulse residue function. If $F\,.\,C_a(t)$ is a delta function, meaning that the unit mass of CA is totally injected at time *t=0*, the tissue response function, $Q(t)$, is assumed to have the form as seen in Figure 6.2 which is the general form of $R(t)$. The initial plateau of $R(t)$ is considered to be the minimum transit time from the arterial inlet to the venous outlet of the brain vascular network.

In perfusion studies, $Q(t)$ and $C_a(t)$ are measured in the tissue voxels and a major artery in the DCE image and the deconvolution between these two will give an estimate of $[F.R(t)]$.

Using $F.R(t)$, by definition, CBV, CBF and MTT are calculated as follows [93]:

(6.4) $$CBV = \ Area\ underneath\ [F.R(t)]$$

(6.5) $$CBF = \ Height\ of\ [F.R(t)]\ plateau$$

(6.6) $$MTT = \frac{CBV}{CBF} = \frac{Area\ underneath\ [F.R(t)]}{Height\ of\ [F.R(t)]\ plateau}$$

Many methods have been proposed for deconvolution and are being currently used in perfusion analysis. New approaches have led to more stable deconvolution methods in presence of noise;

however, this is still an open problem. Also, one critical note about the tissue impulse function is that equation 6.3 is using the assumption that the CA is limited to the intravascular space and there is no leakage into the extravascular space. In the case where the BBB is compromised, area under the $Q(t)$ will be the summation of intravascular and extravascular CA and therefore, CBV will be overestimated. In such cases, calculation of the CBV will not be as straightforward as calculating the area under the curve. This makes perfusion analysis in leaky vasculature a more complicated issue. One solution is extrapolating the training slope of $C_a(t)$ using a mono-exponential function.

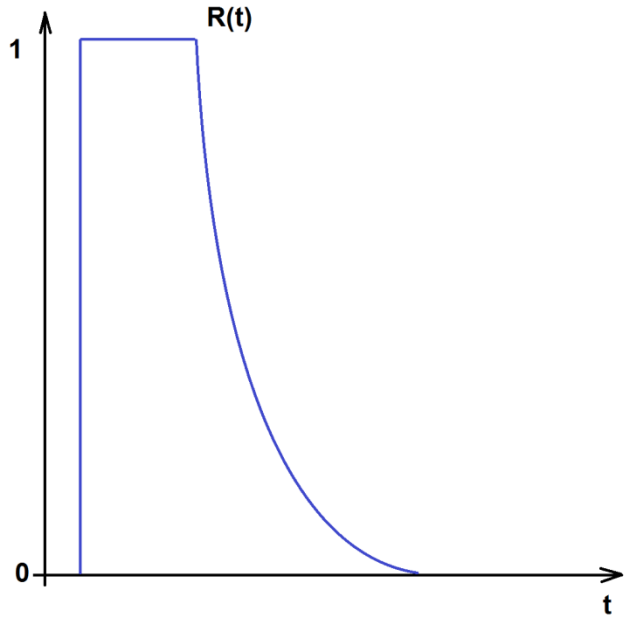

Figure 6.2. Schematic plot of the impulse residue function, R(t)

Here, we introduce another approach for perfusion analysis using our vascular model. The BVM or the intravascular component of the EVM both provide estimates of the flow transfer function from the main artery to each voxel in the image. A close look at the equations 5.2 and 6.3 show that $F.R(t)$ is basically the transfer function that we have defined using our vascular models:

(6.7) $$h(t)_{1\ to\ x} = F.R(t)$$

Therefore by estimating our model based transfer function, R(t) can be directly found, without using deconvolution analysis. The advantage of our method is that by using the EVM, we can find an estimate of the intravascular component of the tissue response (or in other words the impulse residue) function in leaky areas and directly estimate the perfusion parameters using the transfer function of this intravascular component.

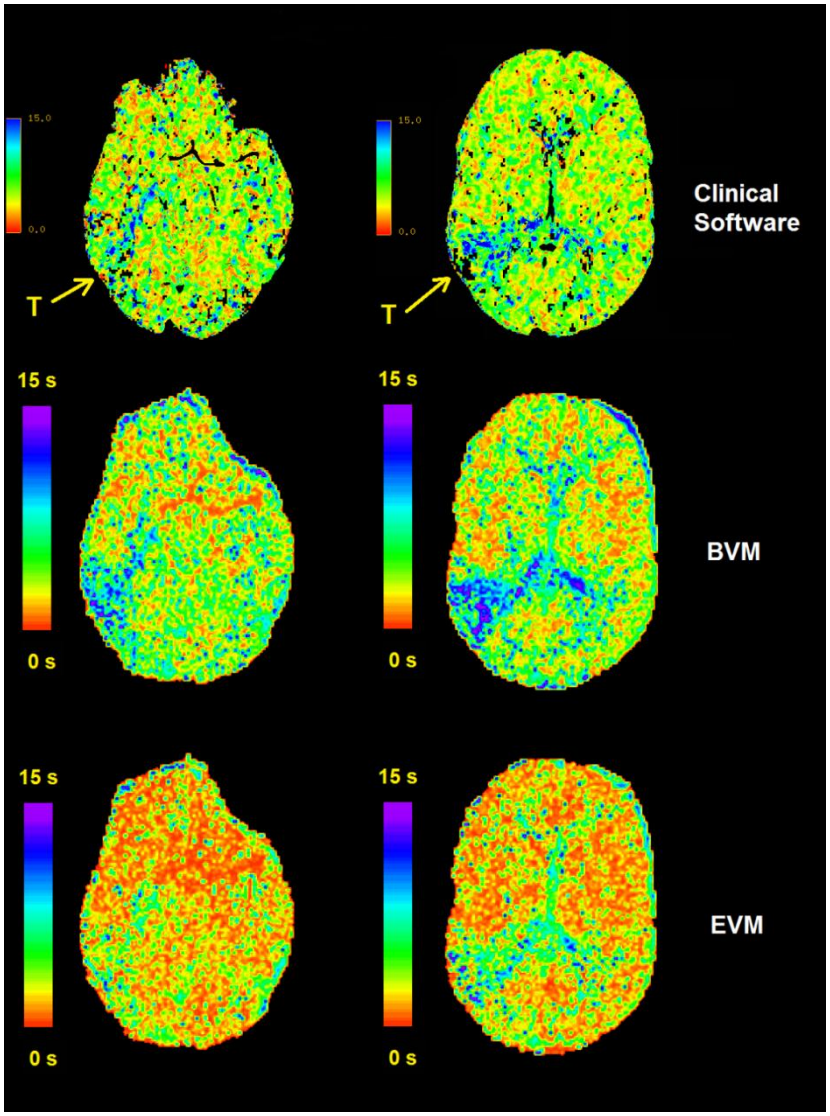

Figure 6.3. The MTT maps for two slices calculated using the clinical software, the Basic Vascular Model (BVM) and the Extended Vascular Model (EVM). As seen in the first row, the MTT for the tumor area (marked with T) is estimated around 15 seconds by the clinical software. When using the BVM, the MTT values are also estimated to be in the same range as the clinical software, however, this overestimation using the BVM is due to the inability of this model to separate the tissue response due to intravascular and extra vascular CA concentrations. The MTT values in the tumor area are around 8 seconds when the EVM is used.

Using this approach, and the method described in the previous chapters, by selecting a reference AIF around the location of the circle of Willis in a DCE-CT image series of the brain of a patient with a cerebral tumor, we found the transfer function at every voxel in the brain and by using the equations above, calculated the MTT in the image. Figure 6.3 shows two slices of this image, along with the results of analyzing the same images using the clinical software. As seen in this figure, in the first row, the MTT for the tumor area is estimated to be around 15 seconds by the clinical software. When using the BVM, the MTT values are also estimated to be in the same range as the clinical software, however, this overestimation using the BVM is due to the inability of this model to separate the tissue response resulting from intravascular and extravascular CA concentrations. When the MTT values are calculated using the TIF estimated by the EVM, in the tumor area these values are around 8 seconds.

6.2.2 Estimation of Permeability Parameters in DCE-MR Imaging Using the EVM

In this section, we demonstrate the results of using the EVM for estimation of the permeability parameters and compare them to the case where a global AIF is used for solving the Tofts Pharmacokinetic equation. The method and software for estimating the permeability parameters using the global AIF has been explained in detail in sections 4.4 and 4.5. In section 5.2.1, we described the method for using the EVM to estimate the transfer function that converts the AIF to the tissue response function in each voxel. Here, we use the results of that section to show the permeability parameter maps in these images.

After estimation of the EVM based transfer function for every voxel in the image, in addition to the parameters describing the vascular structure connecting the major artery and the vessels passing through that voxel, the permeability parameters are also directly estimated as a byproduct of the method. Depending on the model of the leakiness that is being considered, at each branching level, the transfer function can have one (v_p), two (v_p, K^{trans}) or three (v_p, K^{trans}, K_b) parameters to represent models 1, 2 or 3. Therefore the fitting procedure was repeated 18 times to take into account all combinations of six levels of vascular branching and vascular leakiness. After estimating all 18 transfer functions based on the fitting procedure, the AIC was calculated using the resulting RSS and the combined model with the lowest AIC was selected as the best fitted model. Figures 6.4-a, c and e show the three permeability maps (v_p, K^{trans}, K_b) that

were estimated by solving the pharmacokinetic model using the global AIF for the DCE-MR series of the slice shown in 6.4-g. Figures 6.4-b, d and f show the same maps that were estimated using the TIF found by the EVM. As seen here, in the v_p map, in the non-leaky areas, the values found by the two methods are very close; however, the v_p values in figure 6.4-a show lower values in the tumor area compared to figure 6.4-b. This can be interpreted as underestimation of the plasma volume fraction in leaky areas when the global AIF is used. The simulation study in the next section confirms this. Comparison of the K^{trans} and K_b maps show that compared to the case when the EVM is used, the values of K^{trans} and K_b are under and overestimated respectively. Assessment of the accuracy of either method should be investigated using methods such as histology or autoradiography, however the results of the simulation study reported in the nest section, lean towards accuracy of the values found by the EVM.

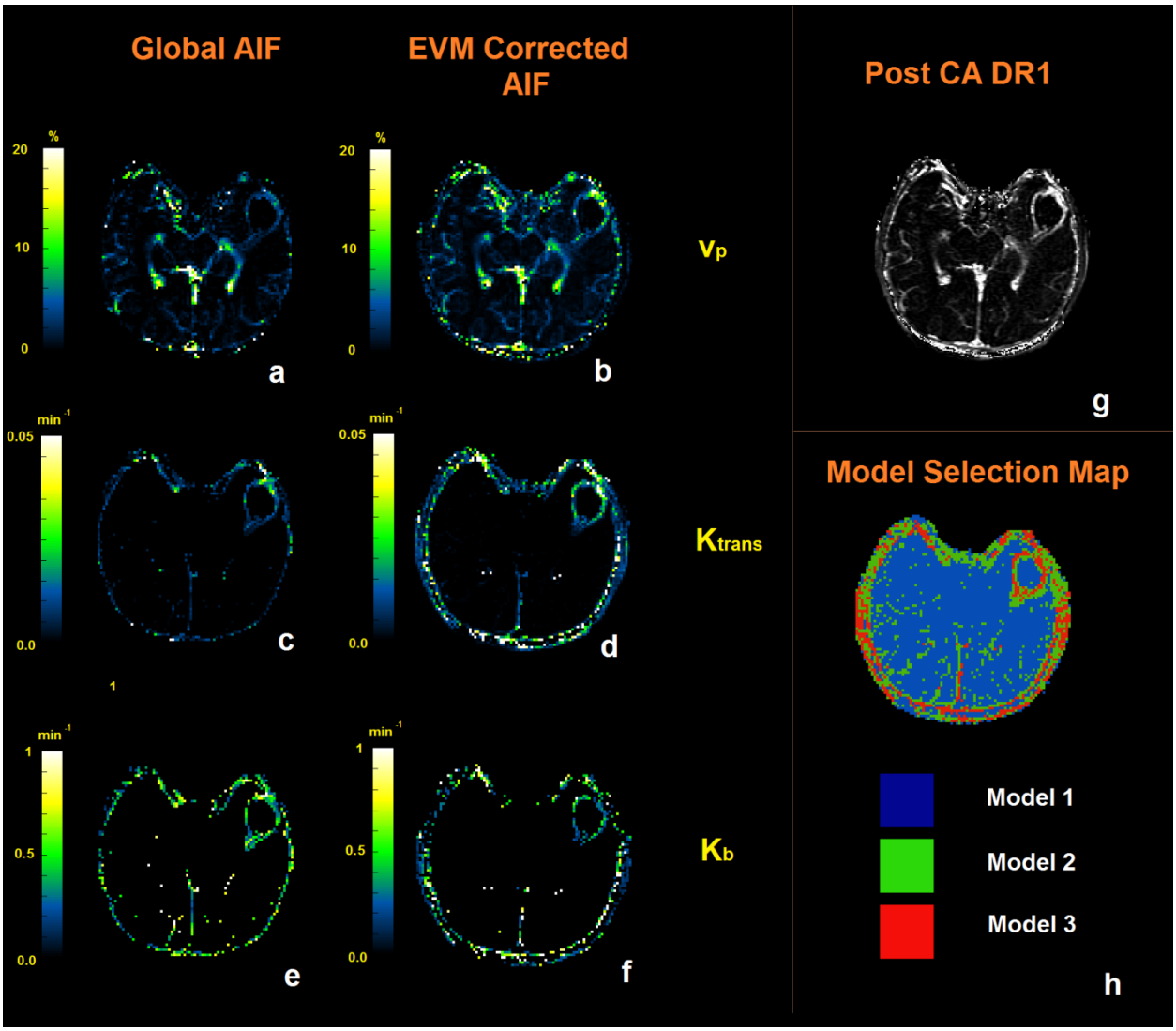

Figure 6.4. (a, c and e) the three permeability maps (v_p, K^{trans}, K_b) estimated by solving the pharmacokinetic model using the global AIF for the DCE-MR series of the slice shown in (g). (b, d and f) permeability maps estimated using the TIF found by the EVM. (h) Model selection map estimated using the RSS of the fitting procedure and finding the minimum AIC.

6.3 Comparison of Performance of the EVM vs. Using the Global AIF: A Simulation Study

In section 4.4, we described the conventional method that is used for solving the Tofts pharmacokinetic model to estimate the permeability parameters. One of our main goals for developing the vascular model (especially as the extended form) was more accurate estimation of the permeability parameters. We had hypothesized that by estimating the local AIF or in other

words the TIF and using that for solving the pharmacokinetic model (instead of using the global AIF), we will be able to find more accurate estimates of these parameters. However, even after applying this method to *in vivo* data, still validation of the method and estimated parameters will still be an issue. In animal models, methods such as histology or autoradiography can be used for measurement of v_p, K^{trans} or v_e, however, for human data, validation in this form would be impossible. Therefore, to compare the performance of these two methods for estimation of the permeability parameters, we conducted a simulation study using our model to compare the value of the estimated parameters using these two methods.

In the first step, using a sampled AIF from the circle of Willis in the $\Delta R1$ image series estimated from the DCE MRI series of a human subject, we estimated curves of the dispersed AIF at different levels of the vascular system using our vascular model. Figure 6.5 shows these curves. The time resolution of these curves is 5.8 seconds therefore considering the fact that the transit time of blood in the brain is about 5 seconds the temporal shift in the rise time of these signals will be at most one timepoint cannot be visualized with the time resolution of these signals. The peaks of these curves have been scaled to the same value for better comparison of the curves.

For our simulation, we separately tested the two methods for each of the three categories of the Pharmacokinetic model as described in section 4.4.2.

For model I, which is considered to be the model with no vascular leakage, the only parameter that is included is the fractional plasma volume, v_p. Using different values of v_p, several tissue response signals were simulated for different levels of the vascular branching structure. Then using the PKM with global AIF and also the EVM, the value of v_p was estimated in these curves. Figure 6.6 and Figure 6.7 show the best fit curves in the case of $v_p = 0.01$, that is estimated using the two methods. As seen in Figure 6.6, in the case of using the global AIF, since the TIF is not corrected for dispersion, as the level of the vascular branching increases the mismatch between the profiles increases as well. In contrast, as Figure 6.7 shows, for all levels of the vascular model, the fit curve matches the profile very closely which can leads to more accurate estimation of v_p.

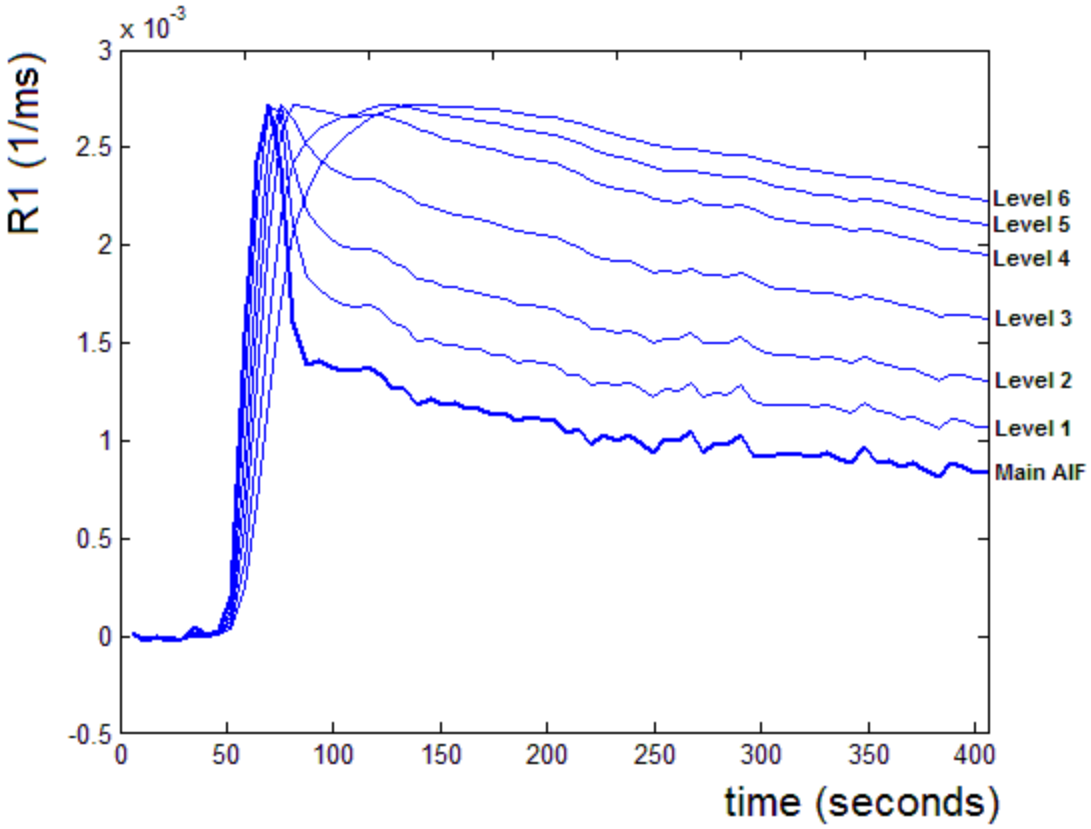

Figure 6.5. The AIF sampled from the circle of Willis in the ΔR1 image series estimated from the DCE MRI series (bold curve) and the curves of the dispersed AIF at different levels of the vascular system found using our vascular model. The time resolution of these curves is 5.8 seconds therefore the temporal shift in the rise time of these signals cannot be visualized using these signals. For visualization, the peaks of these curves have been scaled to the same value.

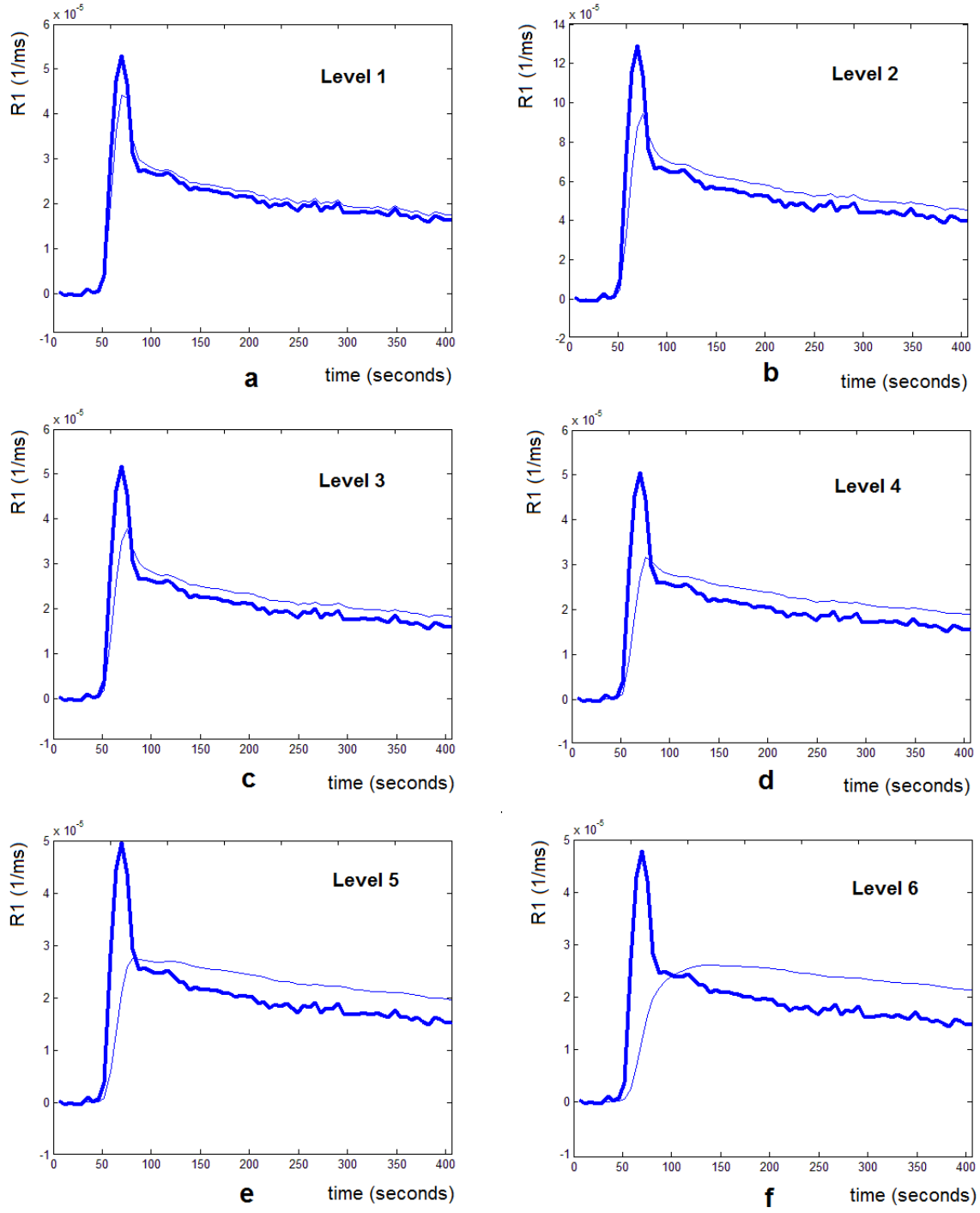

Figure 6.6. The best fit of AIF (bold) to the simulated tissue response curves as seen in Figure 6.5 (thin) for solving the first configuration of the pharmacokinetic model. The solution to this equation is v_p, the fractional plasma volume. As seen in these curves, since the AIF is not corrected for dispersion, as the level of the vascular banching increases, the mismatch between these profiles increases as well. This results in underestimation of the calculated value for v_p.

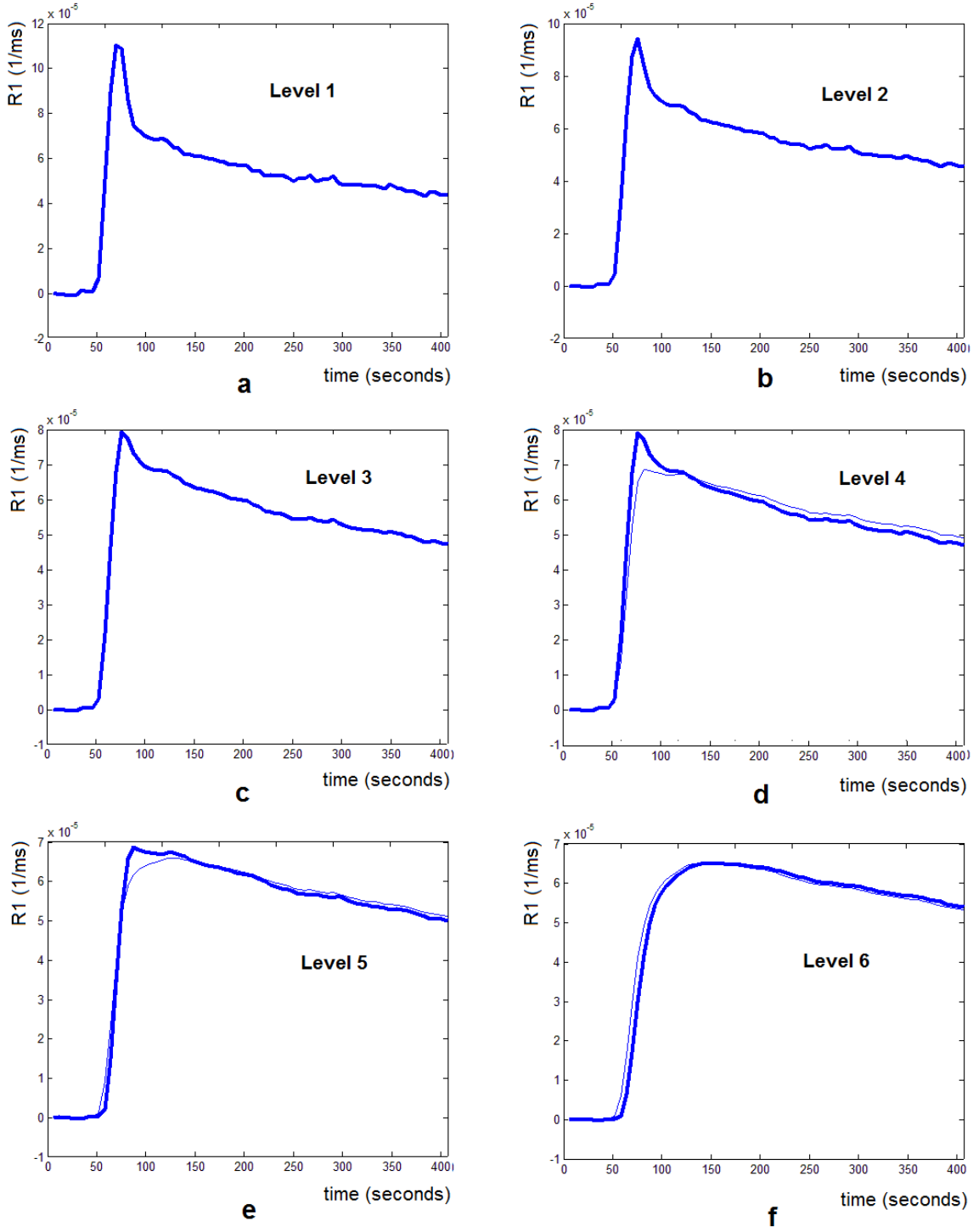

Figure 6.7. The best curves (bold) fit to the same simulated TIF signals (thin) as in Figure 6.6, using the EVM and the first configuration of the pharmacokinetic model . In all levels of the vascular model, the fit curve matches the profile very closely which leads to more accurate estimation of v_p

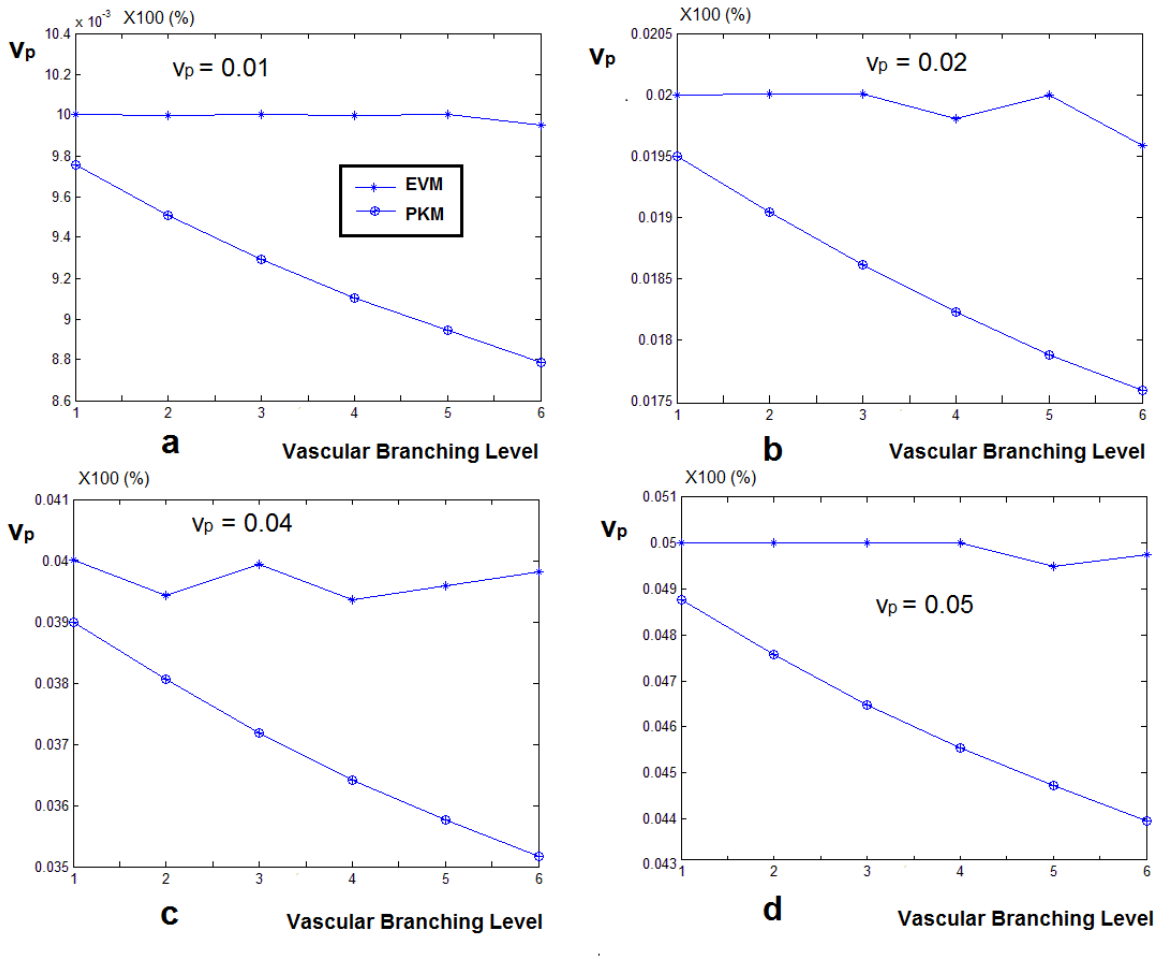

Figure 6.8. (a) The v_p values estimated by solving the PKM equation using the global AIF and the EVM as shown in Figure 6.6 and Figure 6.7. As explained there, when the EVM is used, the estimated vaue of v_p much closer to the nominal value compared to using the AIF which leads to underestimation of v_p. (b)-(d) show the estimated values of v_p for simulating a fractional plasma volume of 0.02, 0.04 and 0.05

In Figure 6.8 the results of estimating v_p using the two methods is presented. The signals were simulated for four values of v_p (0.01, 0.02, 0.04 and 0.05). The observation in all these graphs is that when the global AIF is used, starting from the first level of vascular branching, the value of v_p gets underestimated and the gap between the estimated value and the nominal value increases as the tissue response signal gets more dispersed. But the values estimated by the EVM remain very close to the nominal value at all levels of the vascular branching.

In the next step, the same procedure was repeated but this time, when simulating the tissue response signals, Model II was considered. When creating these signals, the forward transfer rate constant (K^{trans}) was added to the equation to model leakage of the vessels. Next, using the global

AIF and the EVM corrected AIF, the pharmacokinetic model was employed to estimate the values of K^{trans} and v_p in these simulated tissue response signals.

In Figure 6.9 and Figure 6.10 the curves that are fit to the tissue response signals simulated with $v_p = 0.01$ and $K^{trans} = 0.001$ (1/min) are presented. As seen in Figure 5.9, when the global AIF is used, the best fit curve does not follow the trend of the simulated TIF in the higher vascular levels. But in Figure 6.10 when the EVM corrected AIF is used, the resulting curves match the simulated signal in all levels. This figure shows the decomposed intravascular and extravascular components of the signal which are both used for estimating the v_p and the K^{trans} values.

In Figure 6.11, curves are plotted which show the estimated values of K^{trans} and v_p, calculated using the global AIF and the TIF estimated by the EVM, assuming that they are sampled from six different levels of the vascular tree. Figure 6.11 (a) and (b) show the case where $v_p = 0.01$ and $K^{trans} = 0.001$ (1/min) and Figure 6.11 (c) and (d) represent $v_p=0.01$ and $K^{trans} = 0.005$ (1/min). As seen here, in both configurations, the K^{trans} values found using the global AIF are overestimated at all branching levels and as the vascular levels increase, this value increases as well. In the case of $K^{trans} = 0.001$, the over estimation can be as much as 9 times the nominal value and in the case of $K^{trans} = 0.005$, this is about 3 times the nominal value. But for the case of using the EVM, the value of K^{trans} is at most 1.6 times higher than the nominal value. In the case of the estimated v_p, similar to the case of the first configuration of the Pharmacokinetic model, when using the global AIF, the fractional plasma volume is underestimated starting from the first level and is underestimated by about half the nominal value when it gets to the last level. In the case of using the EVM, the estimated value of v_p is almost always accurate.

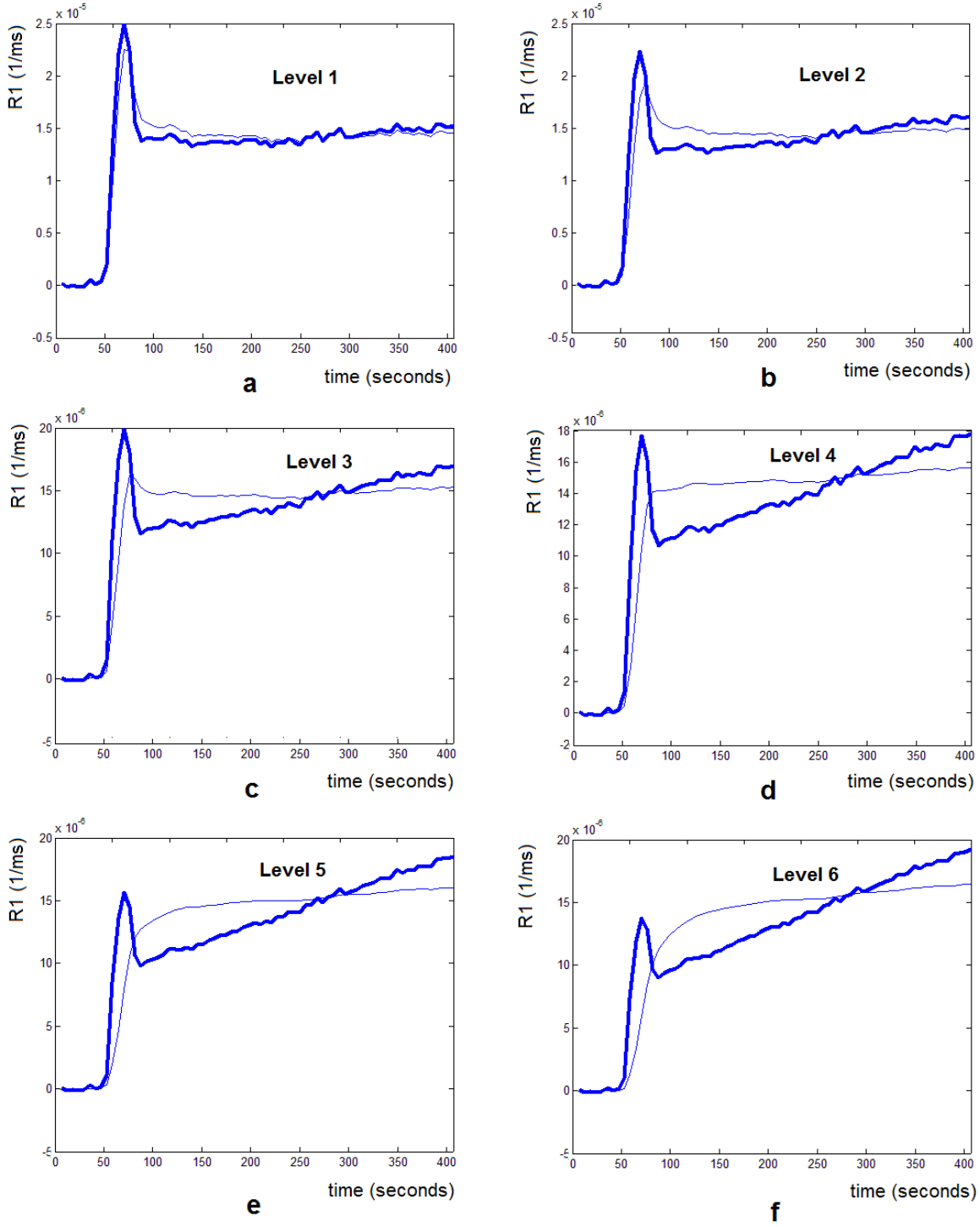

Figure 6.9. The best curves (bold) fit to the simulated tissue response signals (thin) having vascular leakage with the second configuration of the PKM. The two paramaters in this configuration are v_p and K^{trans}. The TIF used here is the AIF and as seen here, the best fit curve does not follow the trend of the simulated TIF in the higher vascular levels. The values af v_p and K^{trans} are 0.01 and 0.001 (1/min) respectively.

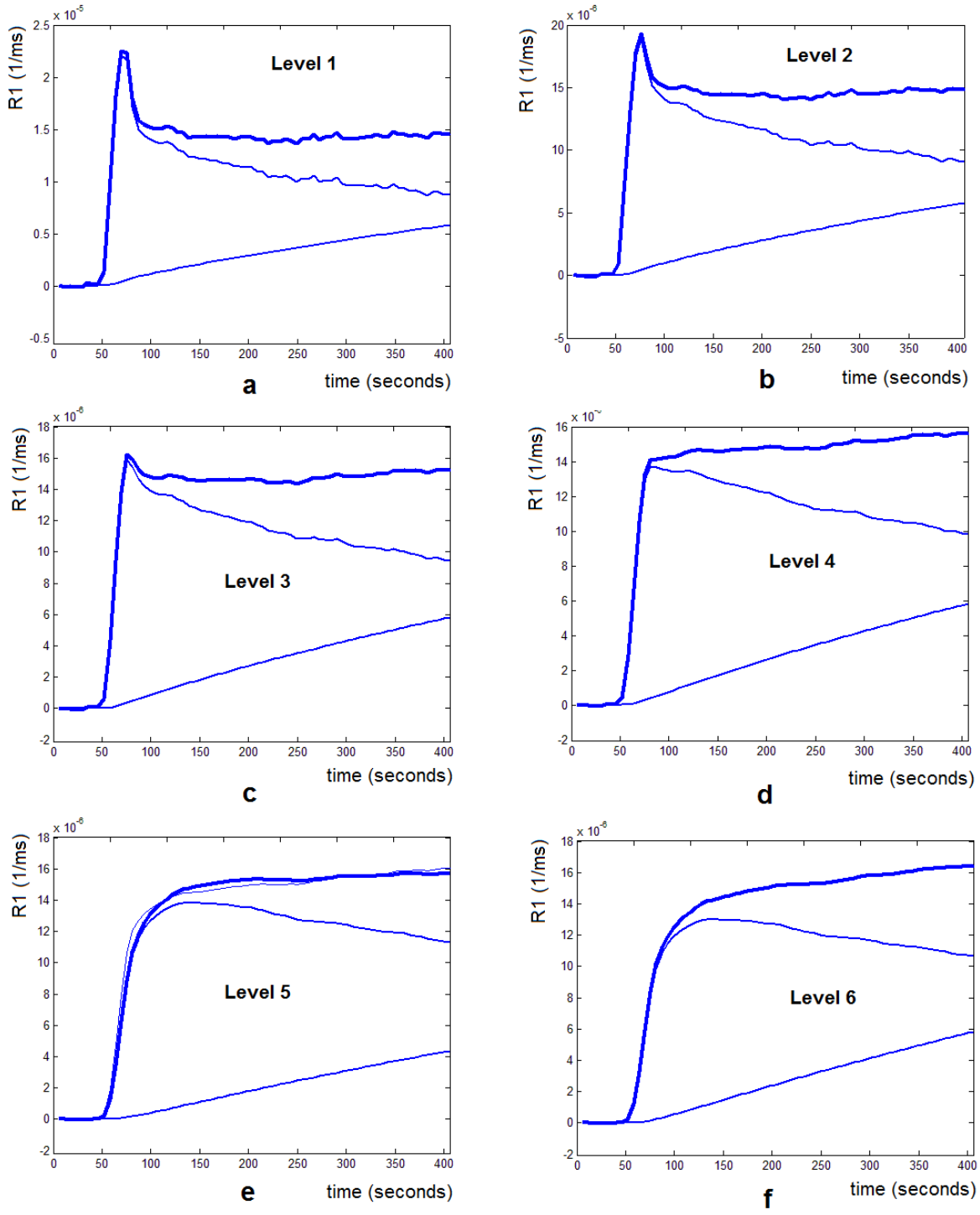

Figure 6.10. The curves fit to the simluated tissue response signals using the EVM. The bold curves show the fit curve and the thin lines represent the extravascular (lower thin line) and intra vascular (upper thin line) components. The inrtravascular and extravascular components are used for estimating the v_p and the K^{trans} values.

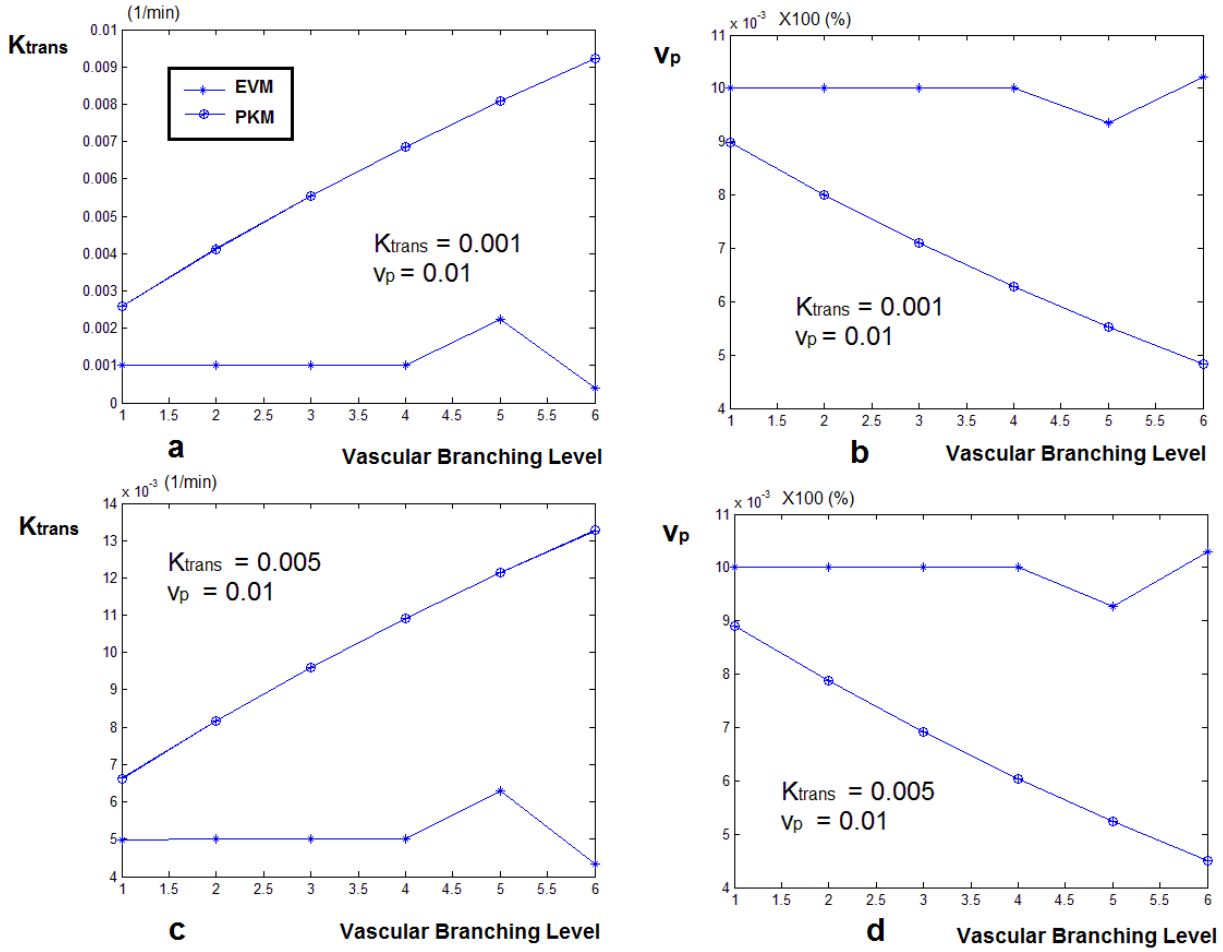

Figure 6.11. Estimated values of K^{trans} and v_p calculated by solving the Pharmacokinetic model using the global AIF and the TIF estimated by the Extended Vascular Model for simulated signals. These signals were created assuming that they are sampled from six different levels of the vascular tree. Also, leakage was added to the vessels based on the second configuration of the pharmacokinetic model where only K^{trans} and v_p exist in the equation. Figures (a) and (b) show the case where v_p = 0.01 and K^{trans} = 0.001 (1/min) and (c) and (d) represent v_p=0.01 and K^{trans} = 0.005 (1/min). As seen here, in both configurations, the K^{trans} values found using the global AIF are overestimated at all branching levels and as the vascular levels increase, this value increases as well. In the case of K^{trans} = 0.001, the over estimation is about 9 X the nominal value and in the case of K^{trans} = 0.005, this is about 3X. In contrast, for the case of using the EVM, the value of K^{trans} is at most 1.6X higher than the nominal value. In the case of v_p, similar to the case of the first configuration of the Pharmacokinetic model, in the case of using the global AIF, the fractional plasma volume is underestimated from the first level and is underestimated by about half the nominal value. In the case of using the EVM, the estimated value of v_p is almost always accurate.

In the last step, the tissue response signal was simulated using model III of the Pharmacokinetic model in which a third parameter, K_b was added. Similar to the other two models, we estimated these three parameters using our two methods and compared the results. Figure 6.12 and Figure 6.13 show the fitting results at different branching levels using the two methods. The values of v_p, K^{trans} and K_b used in the simulation for creating the tissue response curve are 0.01, 0.005 (1/min) and 0.5 (1/min) respectively.

One observation in Figure 6.12 is that even though the global AIF is used, the best fit curve follows the trend of the simulated TIF better than the case of the second configuration of the PKM (as seen in Figure 5). One reason for the better fit is the extra parameter (K_b) added to the equation. The presence of K_b will compensate for dispersion of the AIF; however, the fitting process will lead to overestimation of K_b. Similar to the previous cases, in the case of the EVM corrected AIF (Figure 9) the estimated curve fits the simulated signal very well.

Figure 6.14 shows the graphs comparing the estimated values of K^{trans}, K_b and v_p using the two AIFs for two sets of simulated signals. These signals are created using K^{trans} = 0.005 and v_p = 0.01 and two values for K_b (0.2 and 0.5). As seen in both signal sets, the value of v_p estimated by EVM is almost the same as the nominal value. Also the values of K^{trans} and K_b are estimated close to the nominal value and even though at some of the branching levels they deviate from this value, but it is much less than the estimates when using the global AIF. In this case, the value of K^{trans} can be overestimated as much as 7 times and K_b and high as 4 times the nominal value.

Although the full range of the parameters was not considered here, the results show that when using the EVM estimated TIF, the estimated parameters are less biased compared to using the global AIF. Although in this simulation study, when using the EVM, the same transfer function is used for creating the tissue response signals and for transforming the AIF; however, the accuracy of the results show the reliability of this model for estimating the permeability parameters by decomposing the tissue response signal to the intravascular and extravascular components which is the main advantage compared to using the global AIF. Comparing these simulation results with the results obtained from processing the DCE-MRI data discussed in section 6.2.2 confirms the results found when using real data. Compared to the case when the TIF is corrected, the permeability parameters estimated in the tumor area by using the global AIF, are overestimated or underestimated with the same trend as the simulation study.

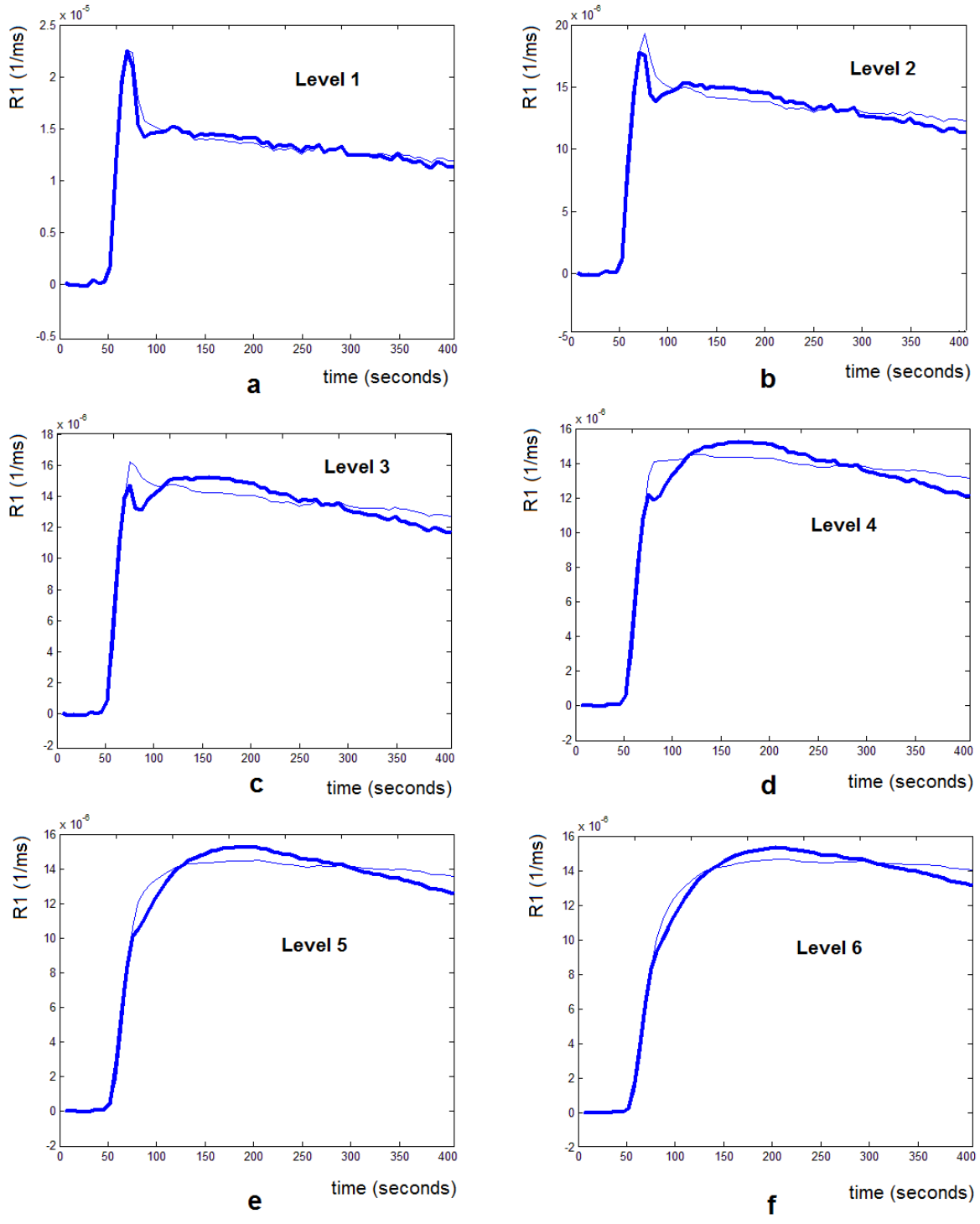

Figure 6.12. The best curves (bold) fit to the simulated tissue response signals (thin) having vascular leakage with the third configuration of the PKM. The three paramaters in this configuration are v_p, K^{trans} and K_b. The TIF used here is the AIF and as seen here, the best fit curve does follows the trend of the simulated TIF better than the case of the second configuration of the PKM (as seen in Figure 5). The reason that the better fitting occurs is the extra parameter (K_b) added to the equation. This will compensate for the dispersion of the AIF; however, it will lead to overestimation of K_b. In these TIFs, the values af v_p, K^{trans} and K_b are 0.01 and 0.005 (1/min) and 0.5 (1/min) respectively

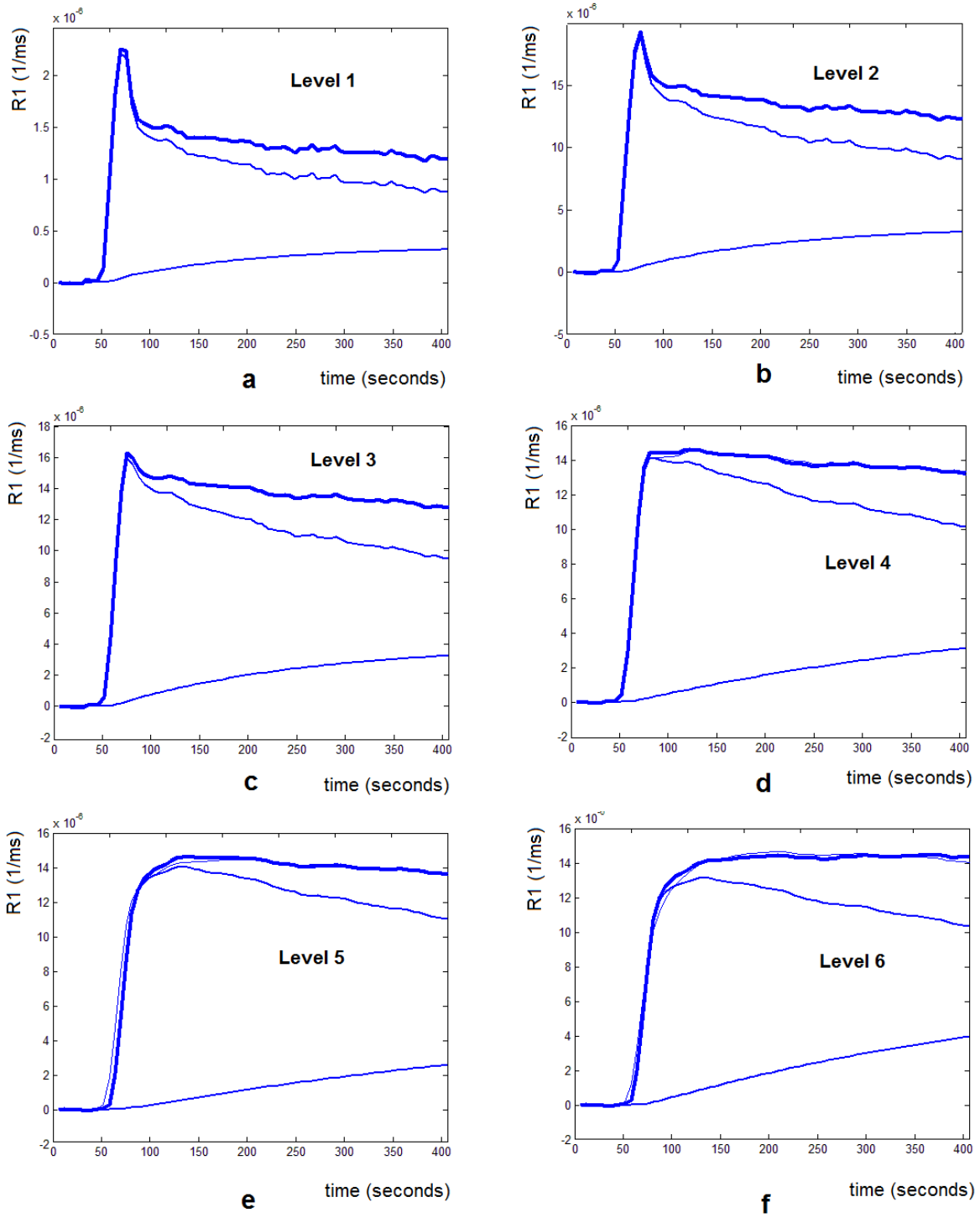

Figure 6.13. The curves fit to the simluated tissue response signals using the EVM with three permeability parameters. The bold curves show the fit curve and the thin lines represent the extravascular (upper thin line) and intra vascular (lower thin line) components. The inrtravascular and extravascular components are used for estimating the v_p, K^{trans} and K_b values.

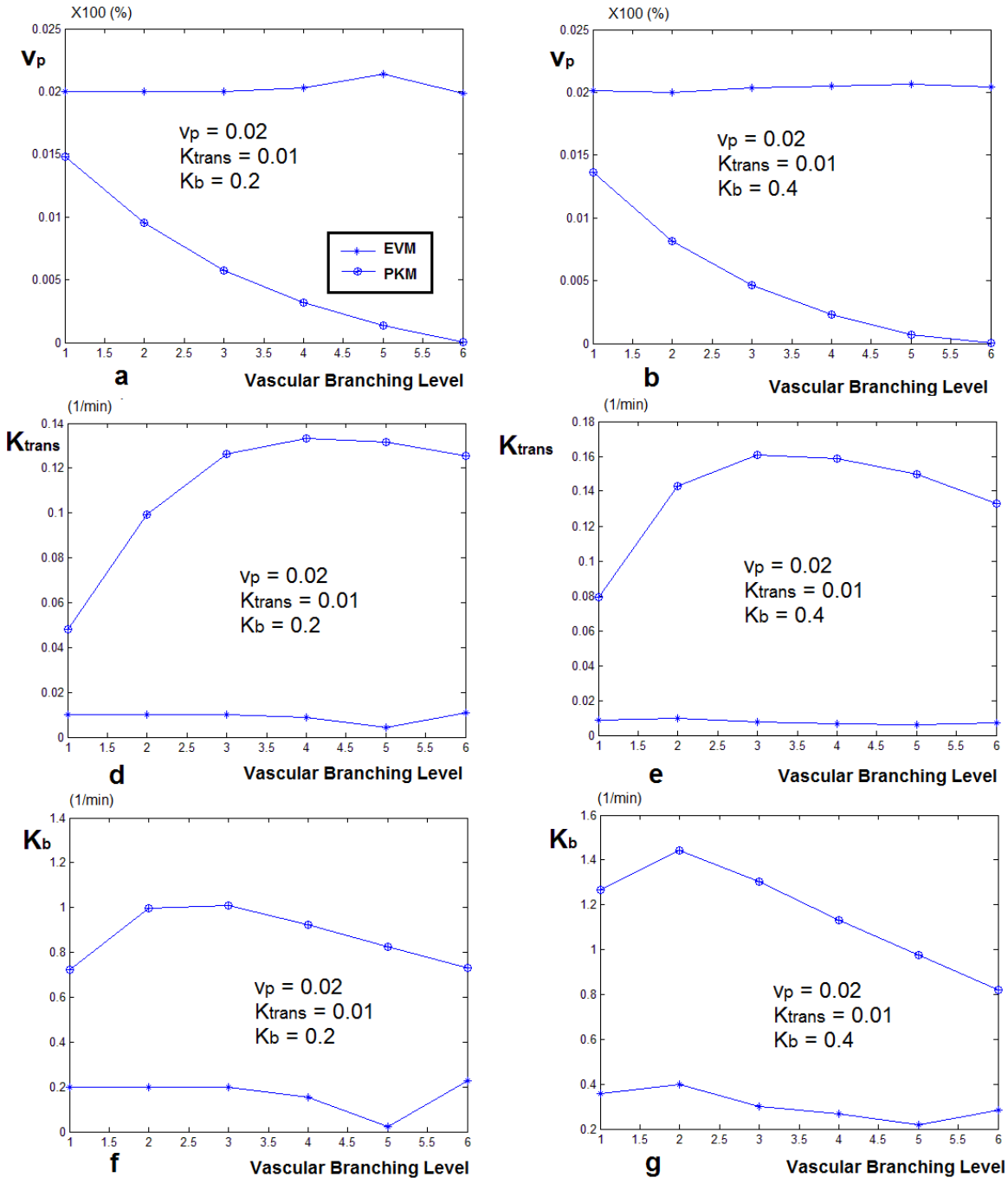

Figure 6.14. Estimated values of v_p, K^{trans} and K_b, using the PKM and global AIF vs. the EVM. The curves on the left (a, d, f) a represent the case where K_b = 0.2 and the curves on the right represent K_b = 0.5. In both cases K^{trans} = 0.005 and v_p = 0.01. As seen in both cases, the value of v_p estimated by EVM is almost the same as the nominal value. The values of K^{trans} and K_b are estimated close to the nominal value and even though at some of the branching levels they deviate from that value but it is much less than the case of the estimates done using the AIF. In this case, the value of K^{trans} can be overestimated as much as 7X and K_b and high as 4X the nominal value.

CHAPTER VII

CONCLUSIONS

In this dissertation, a novel vascular model is introduced that we have developed based on the laws of fluid dynamics and vascular morphology for formulating dispersion and delay of the AIF at different branching levels of the brain vascular system and for finding the AIF at the tissue level (TIF). To test our model and methods, we carried out a simulation study and also studied the application of our method in DCE-CT and DCE-MR images of the human brain. Our model can analytically explain dispersion of the contrast agent profile at different levels of the vascular tree in the brain without any assumptions about the profile of the contrast agent. Simulation results showed high accuracy in finding the level of the CA profile in the vascular tree and the contribution of CA profiles at different levels of the vascular tree. Also, we extended our vascular model to address effects of leakage of the CA to the extravascular space. The Extended Vascular Model describes the measured tissue response function in DCE images based on dispersion of the AIF in the vascular structure as well as leakage of the CA to the extravascular space, using systems analysis methods. We used the extended vascular model to decompose the tissue response function measured by the DCE imaging into its intravascular and extravascular components. This exciting aspect of our model has opened the door to many possibilities for less biased estimation of perfusion and permeability parameters using DCE imaging. In another part of our research, we also studied the results of using different AIFs for calculating the permeability parameters of vasculature and measured the bias that is added to the estimated parameters in each case.

The scientific contributions of this research can be summarized as follows:

- Deriving an equation for the transfer function of a single vessel with laminar flow

- Design and implementation of a three dimensional model of the brain vascular structure for simulating blood flow and dispersion based on the single vessel transfer function

- Developing a model (transfer function) for decomposing the tissue response signal to the intravascular and extravascular components of the signal in areas with leakage of the vessels based on a model of the brain vascular structure.

- More accurate estimation of permeability and perfusion parameters using the decomposed tissue response signal

- Assessment of performance of different methods for estimating T1 maps using Variable Flip Angle SPGRE images and introducing a novel adaptive system for T1 map estimation

- Using model selection for estimation of permeability parameters using the different forms of Tofts extended pharmacokinetic model

- Assessment of the variations in estimating the permeability parameters based on using different AIFs

- Assessment of the variations in estimating the permeability parameters based on using $\Delta R1$ or the Intensity of DCE-MR signals

- Design and Development of a software tool for processing DCE-MR images for estimation of permeability parameters for human and animal data. This software in currently being used and evaluated in four centers.

- Design and Development of a new software tool for processing DCE-MR and DCE-CT images for estimation of permeability and perfusion parameters for human data. This software is based on the new model and currently being internally evaluated.

- Providing a tool to potentially reduce the total scan time in permeability studies using the extended model for analyzing the data.

Our novel semi-empirical model of the brain vascular system was designed and implemented based on laws of fluid dynamics and morphology of the vascular structure in the brain. Other methods have been suggested for modeling dispersion in the vascular structures but they have modeled dispersion based on only delay of parallel branches [16] or in the case of extensive modeling of flow in the vascular structure in the whole body, only flow in major vessels has been addressed [21, 22]. In the work by Calamante et al. [17] the effects of delay and dispersion have both been addressed but the transfer function used is an estimate. In another study Gallichan and Jezzard [31] introduced an approach similar to ours which used the dynamics of laminar and pulsatile flow for finding the dispersion of the bolus and obtained an equation for describing it; however, this equation only described the dispersion of a box-car shaped bolus and also it did not address the effects of branching of the vessels on the dispersion of the bolus profile. The advantage of our model is that we did not make any assumptions about the profile of the contrast agent (such as it being a gamma variate, Gaussian function or square etc.) and we used a transfer function that we estimated based on laws of fluid dynamics in the vessels and have also used facts of vascular morphology in developing it which makes it unique. This novel model can analytically explain dispersion of the contrast agent profile at different levels of the vascular tree in the brain and most importantly in the capillary bed. The vascular model in its current form, does not include all aspects of the laws of fluid dynamics and vascular physiology such as turbulence at the bifurcation points in the vessels; but even though it is not accurate in that sense, considering the data modalities and also the time resolution of our dynamic experiments, it can explain dispersion in the brain vasculature very well. Also, it should be noted that the model that we have used in this study mainly describes arteries, arterioles and capillaries and in order to describe the veins and venules, more parameters should be added to the model to address the dispersion of the CA profile in the veins more accurately. However, considering the fact that the total volume fraction of capillaries, veins and venules consist at most 3% of the total brain volume [94], the likelihood of selecting a voxel representing a vein is very low. For this reason and also to avoid the unnecessary increase of the complexity of our model at this point, we did not include that in our analysis. In the first stage of developing our model, we assumed that the vessels follow the morphology and characteristics of healthy vessels

To test the performance of this model, CA profiles were simulated at different levels of the vascular tree. A combination of simplex (for fitting) and AIC (for model selection) methods

were used to find the level of the simulated CA profiles; the results showed high accuracy in finding the level of the CA profile in the vascular tree, in presence of noise; even with up to 18% noise, the correct level was detected with almost 100% accuracy. Also these simulations showed the ability of our method to separate original signals in a composite signal even when it was contaminated with almost 50% noise. The good performance of this method in presence of noise shows its robustness for finding the vascular branching level of signals in non-simulated data.

To test our model with in vivo data, the same method was applied to DCE-CT images of the human brain. For every voxel in these images, the transfer function of the vascular structure was found and using the parameters of the transfer function a delay map was created. The delay map represents the arrival time of the contrast agent at each voxel; they delay values were estimated by fitting the transfer function to the data and it matched the expected arrival times of the contrast agent. The first tests were done on DCE images of tissues with healthy vessels but since the main application of this model and DCE imaging is for estimating vascular physiology parameters for different pathologies such as brain tumors, it was necessary that in our model address changes in the vascular physiology due to these pathologies as well. Even though in the case of most leaky vessels such as vasculature in tumors, the leakage does not disrupt the blood flow, however, since leaking of the contrast agent into the extravascular space changes the measured response of the voxels to the contrast agent, permeability parameters were incorporated into the model so that the function of the model matches the temporal signals from the images.

Even though at this point only the morphology of healthy arteries, arterioles and capillaries have been included in our model, it can give a good estimate of the transfer functions of most vessels in the brain in its current form. Further steps in this research can involve adding abnormal morphologies of vessels such the vascular structure of tumors to the model and explore their effect on dispersion and changes in the pattern of blood flow. This can lead to more accurate estimation of perfusion and permeability characteristics of vessels in DCE images. Another application of this model and methods introduced in this dissertation is tissue characterization; based on the vascularity of the tissue, the CA profile can change and this can be used to classify it. As was noted, modeling abnormal vasculature can also be used for characterizing different types of tissue the DCE images based on the parameters in the model.

One of the most important products of our vascular model is providing a more realistic estimate of the contrast agent profile (TIF) the image voxels. For regions with intact vessels where there is no leakage of the CA agent to the extracellular space, this profile matches the tissue response measured by the DCE imaging very well. However, a long standing problem in DCE image analysis has been estimating the TIF in areas with leaky vessels. Using the EVM, we are able to decompose the tissue response signal into intravascular and extravascular components. This not only can provide an accurate estimate of the TIF, but it can also simultaneously estimate the permeability parameters of the leaky vessels. The estimated TIF can be used for estimating perfusion parameters.

Another advantage of our method is using model averaging and model selection for choosing the best model to fit the data and using parameters of that model as the estimated parameters. Using different models to fit to the data and using model selection for finding the best fit model can help find the closet match to the physiologic process that had produced the data. One practical issue that we encountered with the Akaike model averaging method was its performance when dealing with noisy data. When the data is noisy, even for the best fit, the residual values cannot get very small and therefore when applying the logarithmic equation, the difference between the AIC values for various models will not differ much. Unless the difference between the residues is large, in these cases, when the penalty value is added (which is the number of model parameters), the bias will always be in favor of models with lower number of parameters. The penalty value is necessary for compensating for overfitting of the models with more parameters, and the penalty of the Akaike method for models with more parameters is less than other methods such as the Bayesian method. However, by directly applying the Akaike method to our data, in noisy areas of the normal tissue, the lower number models are almost always favored. We found a solution to this problem by averaging the low intensity neighboring voxels; however, it would be worth to model noise and investigate the performance of the Akaike method in presence of it to make necessary adjustments to the method.

In the absence of a physical phantom simulating the vascular structure and blood flow of the brain, we tested our model using DCE-CT and DCE-MR images of the human brain. Estimation of the spatial location of the vessels at different branching levels using probability maps and also the ability of our model to describe the profile of the CA at different levels of the vascular

system, with or without leakage, indicates that our model can reasonably describe blood flow, dispersion of the AIF and also leakage of the contrast agent to the extravascular space. Of course, these results are tested within the spatial and temporal resolution of our imaging. Although a few research groups had made perfusion phantoms (either physically fabricated or using simulated data), none of them fit our specifications for our model. In most of these phantoms, the simulated transfer function used is an estimate of the transfer function of vessels which do not simulate the laminar flow and morphology of vessels of the brain as we have simulated and using those to validate of our model would be a fruitless effort. In the best case, the simulations will be using transfer functions based on laminar flow which in this case will provide us with a tool similar to what we have created in our simulations. An indirect method for validating our model is applying it to DCE images of animals for measuring permeability parameters. The advantage of animal models compared to human data is that the accuracy of the measured parameters can be evaluated using histology and autoradiography.

The newly proposed method can have vast applications in DCE imaging and can be used for many classes of analysis of brain tumors, stroke or other neuro-vascular pathologies. For example one of the observations in the images being analyzed with this method so far has been that using the EVM, the tumors get classified mainly as being in the first or second levels of branching. This can mean that they are being directly fed by one of the main cerebral arteries (MCA, PCA or ACA) or their daughter vessels. A more intensive study of the CA profile in different grades of tumors using the model might give information on the angiogenesis involved with them and it can be used for tumor grading.

As part of the future work, to expedite the fitting process for making processing time more practical, we will explore training an adaptive system can based on the EVM vascular model to be used for finding the transfer function parameters for every voxel in the image and use those for estimating the permeability and perfusion characteristics of the vessel. Assuming that this adaptive system works, it will be able process all the voxels in the brain in a matter of seconds.

In summary, we have developed a model of the vascular system of the brain that explains dispersion of the CA profile in different locations of the brain vascular system and also models leakage of the CA to the extravascular space. We tested our model using different modalities of

Dynamic Contrast-Enhanced Imaging and simulated data. The results show that using this model, extravascular and intravascular components of the CA profile can be found in the DCE signal and this can be used for less biased estimates of permeability and perfusion parameters in pathologies with leaky vessels such as tumors.

APPENDIX

Methods

In the appendix section, we will describe the methods that have used for implementing and testing the models. In the first section, the general methods that that are in common among all chapters will be described and next, the specific methodologies for each chapter will be explained.

A.1 General Methods

Modeling, visualization, simulation and programming for the GUIs and algorithms were done using MATLAB, version 2010b on a platform with 64-bit Windows 7 operating system. MATLAB toolboxes used were the Image Processing, Optimization, Parallel Computing, and Signal Processing Toolboxes. The Graphical User Interfaces (GUI's) were developed using GUIDE or the MATLAB (GUI development environment).

A.1.1 The Fitting Procedure

The main MATLAB function used for the Fitting Procedure (fminsearchbnd) was a derivation of the MATLAB function fminsearch. fminsearch uses the simplex search method of Lagarias et al. [44] which is a direct search method not based on numerical or analytical gradients and is categorized as a unconstrained nonlinear optimization method. This MATLAB function can find the minimum of a scalar function of several variables. The problem with fminsearch is that it does not accept any constraints on the bounds. To improve the search fitting procedure and to apply constraints on the variable, we used the fminsearchbnd function. This function has been

is a third party modified version of fminsearch and is used exactly like fminsearch, except that upper and lower bounds are applied to the variables. The user defines the bounds and they are applied to the function internally, using a transformation of the variables. (Quadratic for single bound, sin(x) for dual bounds.) Since the parameters that we deal with in our method are time and gain, they cannot accept negative values and therefore using the constrained version of the search algorithm fits our applications perfectly. For the t_0 values, the maximum value was set to be 2 and for the gain this value was set as 2^6.

The cost function used for the optimization procedure was the sum of squared errors (SSE) between the target curve and the curve created using the parameters found by the fminsearchbnd function. The SSE is defined as:

(A.1) $$SSE = \sum_{i=1}^{N} [S_T(i) - S_F(i)]^2$$

A.2 Specific Methods Used in Chapter 3

A.2.1 Simulating the flow and vascular structure

The starting values for simulating flow in different branches of the model were found in the literature as explained in section 3.2.1. These values were the length, diameter and flow in the major arteries of the brain and using the laws explained in chapter 3 the flow in all the sub-branches were calculated using the simulated model.

A.2.2 Noise added to the system in the single and two signal cases

For simulating the TIF signals for testing the performance of our method in the two situations as explained in chapter 3, we have added noise to the signals and in each noise level, evaluated the performance of our method for first finding the level of the vascular branching for a single signal and secondly the ability to decompose the composite signal to its base signals.

In the first step, to be able to compare the dispersed signals at different levels of the vascular tree, the simulated signals were scaled to the same power level. The scaling factor for the TIF at each branching level *i* was found as below:

(A.2) $$\propto_i = \frac{\sum_{j=1}^{N}[S_0^j]^2}{\sum_{j=1}^{N}[S_i^j]^2}$$

here N is the number of timepoints of the signals, S_0 is the AIF input to the vascular structure and S_i is the simulated TIF at the i^{th} level of the vascular tree. Next, we scaled each simulated signal according to the scaling factor and used these signals as the base signals for the subsequent levels.

To add noise to the signals, the randn command in MATLAB was used. randn(x,y) returns an x-by-y matrix containing pseudorandom values drawn from a normal distribution with a mean of zero and standard deviation of 1. We used the randn command as $\sigma \times$ randn(1,n) to produce a vector with n elements to be added to the signal as Gaussian noise with a standard deviation of σ.

In our study, we added different levels of noise to the signals. The general definition for the Signal to Noise Ratio is (SNR) is as follows:

(A.3) $$SNR = \frac{P_{signal}}{P_{noise}}$$

Where P_{signal} denotes the average power of the signal and P_{noise} the average power of the noise and were calculated as:

(A.4) $$P_{signal} = \frac{\sum_{j=1}^{N}[S_0^j]^2}{n}$$

(A.5) $$P_{noise} = \sigma^2$$

Based on these equations, we applied different values to σ to simulate different values of SNR. The noise levels that were added to the signals were 1, 4, 10, 18, 28, 37, 52, 75, 94 and 100% of the signal power according to the definitions above. In the second case where two signals were added, the noise level was calculated as a percentage of the power level of the composite signal based on the values above.

In the second study where weighted sums of two signals created the composite signals, the contribution level of each signal was varied from 0% to 100% in increments of 10%. This contribution level was calculated based on the power of the signal according to the equation

above. After creating the composite signal, Gaussian noise was added to the composite signal using the same procedure as above with the same 11 levels.

One point that should be noted is that in both of the single signal and the composite signal cases described above, for each level of noise, the procedure was repeated 300 times and the final curves that were created were the average of these signals.

A.2.3 The Fitting Method

Fitting was performed using the method as described in section A.1.1. In this section the function used and the main concepts were described. Using the MATLAB optimset command, the optimization options were set for the fminsearchbnd command. Using this command, the maximum number of iterations was set to 1,000,000 and the termination tolerance on the cost function value was set to 10^{-4}.The starting point for the t_0 parameters in all the fitting procedures were set to 1 which is close to the expected value of the delay in each of the delay lines. The starting value for the gain factor in the fitting algorithm was selected to be 2^n where n is the branching level of the function that to be fitted. The cost function for the fitting procedure was set to the sum of squared errors (SSE) between the target TIF and the TIF created using the parameters found in the fitting procedure.

A.3 Specific Methods used in Chapter 4

The specific methods in Chapter 4 have been explained in detail in the published literature [66].

A.4 Specific Methods Used in Chapter 5

In chapter 5, the extended vascular model was applied to the MR and CT signals and the Akaike maps were created for the two sets of images. In this chapter there is no mention of the model selection and only the residual maps are shown.

The method for estimating the transfer function is the same as that described in section A.1 with the difference that considering the effects of extravasation, another dimension is added to the fitting procedure. The transfer function used in this chapter is described as Equation 5.8. For each of the six branching levels there are three possibilities of extravasation (no leakage, leakage

with no back-flux and leakage with back-flux) which leads to performing the fitting procedure 18 times. The starting values in the fitting procedure for the vascular branching parameters were set as in A.2.3. At each vascular level, first Model 1 was considered with the initial value of 0.01 for v_p and fitting was performed. Next, Model 2 was considered with the v_p found from fitting Model 1 used as the initial value and the starting point for K^{trans} set to 0.001. Finally Model 3 was fit with the final values of v_p and K^{trans} found for Model 2 to be set as the initial values for these parameters and the starting value of K_b was set to 0.1.

A.5 Specific Methods Used in Chapter 6

In this chapter, the main focus is finding the best transfer function based on the extended vascular model to describe the dispersion and delay of the AIF upon arrival at different levels of the tissue. The difference between the function described in this chapter and that in Chapter 3 is that effects of extravasation of the CA to the Extravascular Extracellular space has been added to the function. This point adds one, two or three additional parameters to the function depending on the extravasation model.

Fitting was performed as described in section A.4, Using the final SSE value resulting from fitting each of the 18 configurations of the of models, the AIC was calculated and the model with the lowest AIC was selected as the best model for representing the transfer function that transforms the AIF to the tissue response function in each voxel. The model selection map was created based on the best selected model in the procedure described above.

BIBLIOGRAPHY

[1] J. A. Guzman-de-Villoria, P. Fernandez-Garcia, J. M. Mateos-Perez, and M. Desco, "[Studying cerebral perfusion using magnetic susceptibility techniques: technique and applications]," *Radiologia,* vol. 54, pp. 208-20, May-Jun 2012.

[2] S. Sourbron, M. Ingrisch, A. Siefert, M. Reiser, and K. Herrmann, "Quantification of cerebral blood flow, cerebral blood volume, and blood-brain-barrier leakage with DCE-MRI," *Magn Reson Med,* vol. 62, pp. 205-17, Jul 2009.

[3] A. A. Chan and S. J. Nelson, "Simplified gamma-variate fitting of perfusion curves," presented at the IEEE International Symposium on Biomedical Imaging: Nano to Macro, 2004, 2004.

[4] I. Nestorov, "Whole-body physiologically based pharmacokinetic models," *Expert Opin Drug Metab Toxicol,* vol. 3, pp. 235-49, Apr 2007.

[5] F. Calamante, "Arterial input function in perfusion MRI: A comprehensive review," *Prog Nucl Magn Reson Spectrosc,* vol. 74, pp. 1-32, Oct 2013.

[6] C. D. Murray, "The Physiological Principle of Minimum Work: I. The Vascular System and the Cost of Blood Volume," *Proc Natl Acad Sci U S A,* vol. 12, pp. 207-14, Mar 1926.

[7] C. D. Murray, "The Physiological Principle of Minimum Work Applied to the Angle of Branching of Arteries," *J Gen Physiol,* vol. 9, pp. 835-41, Jul 20 1926.

[8] T. F. Sherman, "On connecting large vessels to small. The meaning of Murray's law," *J Gen Physiol,* vol. 78, pp. 431-53, Oct 1981.

[9] J. Blake, "On the actions of medicine," *Buffalo Medical Journal and Monthly Review of Medical and Surgical Science,* vol. 3, pp. 468-478, 1847.

[10] R. Andres, K. L. Zierler, H. M. Anderson, W. N. Stainsby, G. Cader, A. S. Ghrayyib, and J. L. Lilienthal, Jr., "Measurement of blood flow and volume in the forearm of man; with notes on the theory of indicator-dilution and on production of turbulence, hemolysis, and vasodilatation by intra-vascular injection," *Journal of Clinical Investigation,* vol. 33, pp. 482-504, Apr 1954.

[11] J. T. Fales, S. R. Heisey, and K. L. Zierler, "Blood flow from and oxygen uptake by muscle, during and after partial venous occlusion," *Am J Physiol,* vol. 203, pp. 470-4, Sep 1962.

[12] P. Meier and K. L. Zierler, "On the theory of the indicator-dilution method for measurement of blood flow and volume," *J Appl Physiol,* vol. 6, pp. 731-44, Jun 1954.

[13] K. L. Zierler, "Equations for Measuring Blood Flow by External Monitoring of Radioisotopes," *Circulation Research,* vol. 16, pp. 309-21, Apr 1965.

[14] K. L. Zierler, "Intra-arterial tracer injection methods for evaluating blood flow, volumes of distribution, and trans-capillary exchange in the extremities," *Scand J Clin Lab Invest Suppl,* vol. 99, pp. 65-9, 1967.

[15] F. Calamante, M. Morup, and L. K. Hansen, "Defining a local arterial input function for perfusion MRI using independent component analysis," *Magn Reson Med,* vol. 52, pp. 789-97, Oct 2004.

[16] K. Mouridsen, K. Friston, N. Hjort, L. Gyldensted, L. Ostergaard, and S. Kiebel, "Bayesian estimation of cerebral perfusion using a physiological model of microvasculature," *Neuroimage,* vol. 33, pp. 570-9, Nov 1 2006.

[17] F. Calamante, D. G. Gadian, and A. Connelly, "Delay and dispersion effects in dynamic susceptibility contrast MRI: simulations using singular value decomposition," *Magn Reson Med,* vol. 44, pp. 466-73, Sep 2000.

[18] F. Calamante, D. G. Gadian, and A. Connelly, "Quantification of bolus-tracking MRI: Improved characterization of the tissue residue function using Tikhonov regularization," *Magn Reson Med,* vol. 50, pp. 1237-47, Dec 2003.

[19] J. R. Cebral, P. J. Yim, R. Lohner, O. Soto, and P. L. Choyke, "Blood flow modeling in carotid arteries with computational fluid dynamics and MR imaging," *Academic Radiology,* vol. 9, pp. 1286-99, Nov 2002.

[20] X. Li, E. B. Welch, L. R. Arlinghaus, A. B. Chakravarthy, L. Xu, J. Farley, M. E. Loveless, I. A. Mayer, M. C. Kelley, I. M. Meszoely, J. A. Means-Powell, V. G. Abramson, A. M. Grau, J. C. Gore, and T. E. Yankeelov, "A novel AIF tracking method and comparison of DCE-MRI parameters using individual and population-based AIFs in human breast cancer," *Phys Med Biol,* vol. 56, pp. 5753-69, Sep 7 2011.

[21] S. J. Sherwin, V. Franke, J. Peiró, and K. H. Parker, "One-dimensional modelling of a vascular network in space-time variables," *J Eng Math,* vol. 47, pp. 217-250, 2003.

[22] P. J. Blanco, M. R. Pivello, S. A. Urquiza, and R. A. Feijoo, "On the potentialities of 3D-1D coupled models in hemodynamics simulations," *J Biomech,* vol. 42, pp. 919-30, May 11 2009.

[23] H. Bagher-Ebadian, K. Jafari-Khouzani, H. Soltanian-Zadeh, and J. R. Ewing, "A Blood Circulatory Model to Estimate the Arterial Input Function in MR Brain Perfusion Studies," presented at the in International Society of Magnetic Resonance in Medicine 16, Toronto, Canada, 2008.

[24] A. Noorizadeh, H. Bagher-Ebadian, R. Faghihi, J. Narang, R. Jain, and J. R. Ewing, "Input Function Detection in MR Brain Perfusion Using a Blood Circulatory Model Based Algorithm," presented at the International Society of Magnetic Resonance in Medicine Annual Meeting, Stockholm, Sweden, 2010.

[25] H. Bagher-Ebadian, S. P. Nejad-Davarani, R. Paudyal, T. N. Nagaraga, S. Brown, R. Knight, J. D. Fenstermacher, and J. R. Ewing, "Construction of a Model-Based High Resolution Arterial Input Function (AIF) Using a Standard Radiological AIF and the Levenberg-Marquardt Algorithm," presented at the International Soceity of Megnetic Resonance in Medicine 19, Montreal, Canada, 2011.

[26] M. A. Chappell, M. W. Woolrich, S. Kazan, P. Jezzard, S. J. Payne, and B. J. MacIntosh, "Modeling dispersion in arterial spin labeling: validation using dynamic angiographic measurements," *Magn Reson Med,* vol. 69, pp. 563-70, Feb 2013.

[27] J. Hrabe and D. P. Lewis, "Two analytical solutions for a model of pulsed arterial spin labeling with randomized blood arrival times," *J Magn Reson,* vol. 167, pp. 49-55, Mar 2004.

[28] O. Ozyurt, A. Dincer, and C. Ozturk, "A modified version of Hrabe-Lewis model to acocunt dispersion of labeled bolus in arterial spin labeling.," presented at the 18th Annual Meeting of ISMRM, Stockholm, Sweden, 2010.

[29] L. Hernandez-Garcia, G. R. Lee, A. L. Vazquez, C. Y. Yip, and D. C. Noll, "Quantification of perfusion fMRI using a numerical model of arterial spin labeling that accounts for dynamic transit time effects," *Magn Reson Med,* vol. 54, pp. 955-64, Oct 2005.

[30] S. M. Kazan, M. A. Chappell, and S. J. Payne, "Modeling the effects of flow dispersion in arterial spin labeling," *IEEE Trans Biomed Eng,* vol. 56, pp. 1635-43, Jun 2009.

[31] D. Gallichan and P. Jezzard, "Modeling the effects of dispersion and pulsatility of blood flow in pulsed arterial spin labeling," *Magn Reson Med,* vol. 60, pp. 53-63, Jul 2008.

[32] M. Peladeau-Pigeon and C. Coolens, "Computational fluid dynamics modelling of perfusion measurements in dynamic contrast-enhanced computed tomography: development, validation and clinical applications," *Phys Med Biol,* vol. 58, pp. 6111-31, Sep 7 2013.

[33] S. P. Sourbron and D. L. Buckley, "On the scope and interpretation of the Tofts models for DCE-MRI," *Magn Reson Med,* vol. 66, pp. 735-45, Sep 2011.

[34] G. A. Truskey, F. Yuan, and D. F. Katz, *Transport phenomena in biological systems,* 2nd ed. Upper Saddle River, N.J.: Pearson Prentice Hall, 2009.

[35] R. Uflacker, *Atlas of vascular anatomy : an angiographic approach,* 2nd ed. Philadelphia: Lippincott Williams & Wilkins, 2007.

[36] S. N. Wright, P. Kochunov, F. Mut, M. Bergamino, K. M. Brown, J. C. Mazziotta, A. W. Toga, J. R. Cebral, and G. A. Ascoli, "Digital reconstruction and morphometric analysis of human brain arterial vasculature from magnetic resonance angiography," *Neuroimage,* vol. 82C, pp. 170-181, May 28 2013.

[37] A. J. Vander, J. H. Sherman, and D. S. Luciano, *Human physiology : the mechanisms of body function,* 8th ed. Boston: McGraw-Hill, 2001.

[38] W. K. Purves, *Life, the science of biology,* 7th ed. Sunderland, Mass., Gordonsville, VA: Sinauer Associates ; W.H. Freeman and Co., 2004.

[39] R. Fahraeus and T. Lindqvist, "The viscosity of the blood in narrow capillary tubes," *The American Journal of Physiology,* vol. 96, pp. 562–568, 1931.

[40] S. P. Sourbron and D. L. Buckley, "Classic models for dynamic contrast-enhanced MRI," *NMR Biomed,* vol. 26, pp. 1004-27, Aug 2013.

[41] S. E. Lee, S. W. Lee, P. F. Fischer, H. S. Bassiouny, and F. Loth, "Direct numerical simulation of transitional flow in a stenosed carotid bifurcation," *J Biomech,* vol. 41, pp. 2551-61, Aug 7 2008.

[42] A. A. van Steenhoven, F. N. van de Vosse, C. C. Rindt, J. D. Janssen, and R. S. Reneman, "Experimental and numerical analysis of carotid artery blood flow," *Monogr Atheroscler,* vol. 15, pp. 250-60, 1990.

[43] A. Esposito, "A Simplified Method for Analyzing Circuits by Analogy," *Machine Design,* vol. October, pp. 173-177, 1969.

[44] J. C. Lagarias, J. A. Reeds, M. H. Wright, and P. E. Wright, "Convergence Properties of the Nelder-Mead Simplex Method in Low Dimensions," *SIAM Journal of Optimization,* vol. 9, p. 36, 1998.

[45] D. Posada and T. R. Buckley, "Model selection and model averaging in phylogenetics: advantages of akaike information criterion and bayesian approaches over likelihood ratio tests," *Syst Biol,* vol. 53, pp. 793-808, Oct 2004.

[46] K. P. Burnham and D. R. Anderson, *Model selection and multimodel inference : a practical information-theoretic approach,* 2nd ed. New York: Springer, 2002.

[47] K. P. Burnham and D. R. Anderson, *Model selection and inference : a practical information-theoretic approach.* New York: Springer, 1998.

[48] L. A. Ferrara, M. Mancini, R. Iannuzzi, T. Marotta, I. Gaeta, F. Pasanisi, A. Postiglione, and L. Guida, "Carotid diameter and blood flow velocities in cerebral circulation in hypertensive patients," *Stroke,* vol. 26, pp. 418-21, Mar 1995.

[49] J. Krejza, M. Arkuszewski, S. E. Kasner, J. Weigele, A. Ustymowicz, R. W. Hurst, B. L. Cucchiara, and S. R. Messe, "Carotid artery diameter in men and women and the relation to body and neck size," *Stroke,* vol. 37, pp. 1103-5, Apr 2006.

[50] P. S. Tofts, "T1-weighted DCE Imaging Concepts: Modelling, Acquisition and Analysis," in *MAGNETOM flash*, ed, 2010, pp. 30-39.

[51] G. Strich, P. L. Hagan, K. H. Gerber, and R. A. Slutsky, "Tissue distribution and magnetic resonance spin lattice relaxation effects of gadolinium-DTPA," *Radiology,* vol. 154, pp. 723-6, Mar 1985.

[52] R. C. Brasch, H. J. Weinmann, and G. E. Wesbey, "Contrast-enhanced NMR imaging: animal studies using gadolinium-DTPA complex," *AJR Am J Roentgenol,* vol. 142, pp. 625-30, Mar 1984.

[53] H. Bagher-Ebadian, R. Paudyal, T. N. Nagaraja, R. L. Croxen, J. D. Fenstermacher, and J. R. Ewing, "MRI estimation of gadolinium and albumin effects on water proton," *Neuroimage,* vol. 54 Suppl 1, pp. S176-9, Jan 2011.

[54] E. L. Barbier, J. A. den Boer, A. R. Peters, A. R. Rozeboom, J. Sau, and A. Bonmartin, "A model of the dual effect of gadopentetate dimeglumine on dynamic brain MR images," *J Magn Reson Imaging,* vol. 10, pp. 242-53, Sep 1999.

[55] N. Gelman, J. R. Ewing, J. M. Gorell, E. M. Spickler, and E. G. Solomon, "Interregional variation of longitudinal relaxation rates in human brain at 3.0 T: relation to estimated iron and water contents," *Magn Reson Med,* vol. 45, pp. 71-9, Jan 2001.

[56] H. Bagher-Ebadian, S. P. Nejad-Davarani, M. M. Ali, S. Brown, M. Makki, Q. Jiang, D. C. Noll, and J. R. Ewing, "Magnetic resonance imaging estimation of longitudinal relaxation rate change (ΔR1) in dual gradient echo sequences using an adaptive model," in *IJCNN 2011*, San Jose, CA, 2011, pp. 2501-2506.

[57] R. P. Crick and P. T. Khaw, *A textbook of clinical ophthalmology : a practical guide to disorders of the eyes and their management*, 3rd ed. River Edge, NJ: World Scientific, 2003.

[58] F. G. Holz, R. Spaide, and SpringerLink (Online service). (2010). *Medical Retina Focus on Retinal Imaging*. Available: http://dx.doi.org/10.1007/978-3-540-85540-8

[59] A. Ogura, A. Miyai, F. Maeda, T. Hongoh, and R. Kikumoto, "[Comparison of contrast resolution between dynamic MRI and dynamic CT in liver scanning]," *Nihon Hoshasen Gijutsu Gakkai Zasshi,* vol. 58, pp. 286-91, Feb 2002.

[60] K. Kudo, S. Terae, C. Katoh, M. Oka, T. Shiga, N. Tamaki, and K. Miyasaka, "Quantitative cerebral blood flow measurement with dynamic perfusion CT using the vascular-pixel elimination method: comparison with H2(15)O positron emission tomography," *AJNR Am J Neuroradiol,* vol. 24, pp. 419-26, Mar 2003.

[61] J. P. O'Connor, P. S. Tofts, K. A. Miles, L. M. Parkes, G. Thompson, and A. Jackson, "Dynamic contrast-enhanced imaging techniques: CT and MRI," *Br J Radiol,* vol. 84 Spec No 2, pp. S112-20, Dec 2011.

[62] M. Ibaraki, H. Ito, E. Shimosegawa, H. Toyoshima, K. Ishigame, K. Takahashi, I. Kanno, and S. Miura, "Cerebral vascular mean transit time in healthy humans: a comparative study with PET and dynamic susceptibility contrast-enhanced MRI," *J Cereb Blood Flow Metab,* vol. 27, pp. 404-13, Feb 2007.

[63] C. S. Patlak and R. G. Blasberg, "Graphical evaluation of blood-to-brain transfer constants from multiple-time uptake data. Generalizations," *J Cereb Blood Flow Metab,* vol. 5, pp. 584-90, Dec 1985.

[64] C. S. Patlak, R. G. Blasberg, and J. D. Fenstermacher, "Graphical evaluation of blood-to-brain transfer constants from multiple-time uptake data," *J Cereb Blood Flow Metab,* vol. 3, pp. 1-7, Mar 1983.

[65] P. S. Tofts, G. Brix, D. L. Buckley, J. L. Evelhoch, E. Henderson, M. V. Knopp, H. B. Larsson, T. Y. Lee, N. A. Mayr, G. J. Parker, R. E. Port, J. Taylor, and R. M. Weisskoff, "Estimating kinetic parameters from dynamic contrast-enhanced T(1)-weighted MRI of a diffusable tracer: standardized quantities and symbols," *J Magn Reson Imaging,* vol. 10, pp. 223-32, Sep 1999.

[66] H. Bagher-Ebadian, R. Jain, S. P. Nejad-Davarani, T. Mikkelsen, M. Lu, Q. Jiang, L. Scarpace, A. S. Arbab, J. Narang, H. Soltanian-Zadeh, R. Paudyal, and J. R. Ewing, "Model selection for DCE-T1 studies in glioblastoma," *Magn Reson Med,* vol. 68, pp. 241-51, Jul 2012.

[67] E. M. Haacke, *Magnetic resonance imaging : physical principles and sequence design*. New York: Wiley, 1999.

[68] K. L. Li, X. P. Zhu, J. Waterton, and A. Jackson, "Improved 3D quantitative mapping of blood volume and endothelial permeability in brain tumors," *J Magn Reson Imaging,* vol. 12, pp. 347-57, Aug 2000.

[69] X. Li, W. D. Rooney, C. G. Varallyay, S. Gahramanov, L. L. Muldoon, J. A. Goodman, I. J. Tagge, A. H. Selzer, M. M. Pike, E. A. Neuwelt, and C. S. Springer, Jr., "Dynamic-contrast-enhanced-MRI with extravasating contrast reagent: rat cerebral glioma blood volume determination," *J Magn Reson,* vol. 206, pp. 190-9, Oct 2010.

[70] M. Heilmann, F. Kiessling, M. Enderlin, and L. R. Schad, "Determination of pharmacokinetic parameters in DCE MRI: Consequence of nonlinearity between contrast agent concentration and signal intensity," *Invest Radiol,* vol. 41, pp. 536-43, Jun 2006.

[71] P. S. Tofts, "Modeling tracer kinetics in dynamic Gd-DTPA MR imaging," *J Magn Reson Imaging,* vol. 7, pp. 91-101, Jan-Feb 1997.

[72] P. L. Choyke, A. J. Dwyer, and M. V. Knopp, "Functional tumor imaging with dynamic contrast-enhanced magnetic resonance imaging," *J Magn Reson Imaging,* vol. 17, pp. 509-20, May 2003.

[73] H. Bagher-Ebadian, S. P. Nejad-Davarani, R. Jain, D. Noll, Q. Jiang, A. S. Arbab, T. Mikkelsen, and J. R. Ewing, "An Analytical Approach for Quantification and Comparison between Signal Intensity and Longitudinal Relaxation Rate Change (ΔR1) in MR DCE-T1 Studies," presented at the ISMRM 20th Annual Meeting and Exhibition, Melbourne, Australia, 2012.

[74] H. Bagher-Ebadian, S. P. Nejad-Davarani, R. Jain, D. Noll, Q. Jiang, A. S. Arbab, T. Mikkelsen, and J. R. Ewing, "Comparison of Signal Intensity and Standard Techniques for Estimation of Pharmacokinetic Parameters in DCE-T1 Studies of Glioblastoma: Using Model Selection," presented at the ISMRM 20th Annual Meeting and Exhibition, Melbourne, Australia, 2012.

[75] L. C. Chang, C. G. Koay, P. J. Basser, and C. Pierpaoli, "Linear least-squares method for unbiased estimation of T1 from SPGR signals," *Magn Reson Med,* vol. 60, pp. 496-501, Aug 2008.

[76] H. Bagher-Ebadian, S. P. Nejad-Davarani, J. R. Ewing, Q. Jiang, D. Hearshen, R. Jain, T. Mikkelsen, and H. Soltanian-Zadeh, "MR Estimation of Longitudinal Relaxation Time (T1) in SPGRE Pulse Sequence Using an Adaptive Model: Evaluation and Comparison with Conventional Methods," *Submitted to MRM-Under Review,* 2013.

[77] H. Bagher-Ebadian, M. M. Ali, A. S. Arbab, M. Makki, S. P. Nejad-Davarani, S. Panda, Q. Jiang, and J. R. Ewing, "Adaptive Neural Network for Direct Quantification of Longitudinal Relaxation Rate Change (ΔR1) in T One by Multiple Read Out (TOMROP) Sequence," presented at the ISMRM, 19th Annual Meeting and Exhibition, Montreal, Canada, 2011.

[78] S. C. Deoni, B. K. Rutt, and T. M. Peters, "Rapid combined T1 and T2 mapping using gradient recalled acquisition in the steady state," *Magn Reson Med*, vol. 49, pp. 515-26, Mar 2003.

[79] S. C. Deoni, T. M. Peters, and B. K. Rutt, "High-resolution T1 and T2 mapping of the brain in a clinically acceptable time with DESPOT1 and DESPOT2," *Magn Reson Med*, vol. 53, pp. 237-41, Jan 2005.

[80] R. Gupta, "A new look at the method of variable nutation angle for the measurement of spin-lattice relaxation time using fourier transform, NMR.," *J Magn Imaging*, vol. 25, 1977.

[81] L. C. Chang, C. G. Koay, P. J. Basser, and C. Pierpaoli, "Linear least-squares method for unbiased estimation of T1 from SPGR signals," *Magn Reson Med*, vol. 60, 2008.

[82] G. F. Mason, W. J. Chu, and H. P. Hetherington, "A general approach to error estimation and optimized experiment design, applied to multislice imaging of T1 in human brain at 4.1 T," *J Magn Reson*, vol. 126, pp. 18-29, May 1997.

[83] J. R. Ewing, S. L. Brown, M. Lu, S. Panda, G. Ding, R. A. Knight, Y. Cao, Q. Jiang, T. N. Nagaraja, J. L. Churchman, and J. D. Fenstermacher, "Model selection in magnetic resonance imaging measurements of vascular permeability: Gadomer in a 9L model of rat cerebral tumor," *J Cereb Blood Flow Metab*, vol. 26, pp. 310-20, Mar 2006.

[84] J. R. Ewing and H. Bagher-Ebadian, "Model selection in measures of vascular parameters using dynamic contrast-enhanced MRI: experimental and clinical applications," *NMR Biomed*, vol. 26, pp. 1028-41, Aug 2013.

[85] G. Johnson, S. G. Wetzel, S. Cha, J. Babb, and P. S. Tofts, "Measuring blood volume and vascular transfer constant from dynamic, T(2)*-weighted contrast-enhanced MRI," *Magn Reson Med*, vol. 51, pp. 961-8, May 2004.

[86] D. Marquardt, " An algorithm for least-squares estimation on nonlinear parameters," *J Soc Ind Appl Math*, vol. 11, pp. 431–441, 1963.

[87] B. R. Rosen, J. W. Belliveau, J. M. Vevea, and T. J. Brady, "Perfusion imaging with NMR contrast agents," *Magn Reson Med*, vol. 14, pp. 249-65, May 1990.

[88] L. Ostergaard, R. M. Weisskoff, D. A. Chesler, C. Gyldensted, and B. R. Rosen, "High resolution measurement of cerebral blood flow using intravascular tracer bolus passages. Part I: Mathematical approach and statistical analysis," *Magn Reson Med*, vol. 36, pp. 715-25, Nov 1996.

[89] R. Weisskoff, J. Boxerman, A. Sorensen, S. Kulke, and B. Rosen, "Simultaneous blood volume and permeability mapping using a single Gd-based contrast injection," presented at the Second Annual Meeting of Society of Magnetic Resonance, San Francisco, CA, USA, 1994.

[90] A. Bjornerud, A. G. Sorensen, K. Mouridsen, and K. E. Emblem, "T1- and T2*-dominant extravasation correction in DSC-MRI: part I--theoretical considerations and implications for assessment of tumor hemodynamic properties," *J Cereb Blood Flow Metab*, vol. 31, pp. 2041-53, Oct 2011.

[91] T. N. Nagaraja, K. Karki, J. R. Ewing, G. W. Divine, J. D. Fenstermacher, C. S. Patlak, and R. A. Knight, "The MRI-measured arterial input function resulting from a bolus injection of Gd-DTPA in a rat model of stroke slightly underestimates that of Gd-[14C]DTPA and marginally

overestimates the blood-to-brain influx rate constant determined by Patlak plots," *Magn Reson Med,* vol. 63, pp. 1502-9, Jun 2010.

[92] H. Bagher-Ebadian, A. Noorizadeh, S. P. Nejad-Davarani, R. Paudyal, T. N. Nagaraja, R. Knight, S. Brown, J. D. Fenstermacher, and J. R. Ewing, "Construction of a Model-Based High Resolution Arterial Input Function (AIF) Using a Standard Radiological AIF and the Levenberg-Marquardt Algorithm," presented at the ISMRM 19th Annual Meeting and Exhibition Montreal, Canada, 2011.

[93] J. D. Eastwood, M. H. Lev, T. Azhari, T. Y. Lee, D. P. Barboriak, D. M. Delong, C. Fitzek, M. Herzau, M. Wintermark, R. Meuli, D. Brazier, and J. M. Provenzale, "CT perfusion scanning with deconvolution analysis: pilot study in patients with acute middle cerebral artery stroke," *Radiology,* vol. 222, pp. 227-36, Jan 2002.

[94] H. Ito, I. Kanno, H. Iida, J. Hatazawa, E. Shimosegawa, H. Tamura, and T. Okudera, "Arterial fraction of cerebral blood volume in humans measured by positron emission tomography," *Ann Nucl Med,* vol. 15, pp. 111-6, Apr 2001.